Alma Mater Studiorum · University of Bologna

School of Science
Department of Physics and Astronomy
Master Degree in Physics

Quality Control in Digital Breast Tomosynthesis: compliance of two phantoms with the EUREF protocol.

Supervisor:
Prof. Nico Lanconelli

Co-supervisors:
Dr. Matilde Costa
Dr. Barbara Mongero
Dr. Silvia Pesente

Submitted by:
Azzurra Sisi

Academic Year 2021/2022

Abstract

Ever since the integration of Digital Breast Tomosynthesis (DBT) into breast cancer screening programmes, it has been a European endeavour to draw up standard guidelines for the assessment of the imaging performance of DBT systems. The quantitative evaluation of the quality of reconstructed tomosynthesis images is still an active area of research. In fact, the current version of the EUREF DBT QC protocol represents a preliminary set of guidelines to be used at acceptance, and to establish baseline values for constancy testing. New phantoms for QC in DBT have also been developed. Together, Sun Nuclear's Mammo 3D Performance Kits and CIRS DBT QC Phantom, model 021, have been shown to provide adequate test objects and background material for the assessment of the Automatic Exposure Control system performance, image receptor response function and noise analysis, system sharpness measured in projection images, and in-plane and out-of-plane spatial resolution in the reconstructed tomosynthesis image. From the comparison with the available literature, the use of the two phantoms with the Hologic Selenia Dimensions and Fujifilm AMULET Innovality systems has been validated.

Contents

Introduction

Breast cancer is the most commonly diagnosed cancer in women worldwide, accounting for 11.7% of total cancer cases, and one of the leading causes of cancer-related deaths. In 2020, there were 2.3 million new cases of breast cancer and an estimated 685,000 deaths in females globally, corresponding to 16% of cancer deaths [51], [20].

As well as effective treatment, breast cancer prognosis strongly depends on early detection. To this end, the World Health Organization advocates early diagnosis of symptomatic cancer, and population-wide screening, which is the identification of the disease in asymptomatic individuals [24]. The Guidelines Development Group (GDG) of the European Commission Initiative on Breast Cancer (ECIBC) recommends that asymptomatic women aged 45-74 with an average risk of breast cancer, undergo screening every 2 to 3 years [3]. Indeed, screening programmes in conjunction with advances in therapy have shown to reduce cancer-related mortality up to 30% [22], [30].

Full-Field Digital Mammography (FFDM) is the best method to detect breast cancer at an early stage. In routine screening FFDM, two-dimensional x-ray projections of each breast are acquired in the medial-lateral-oblique (MLO) and cranio-caudal (CC) directions. However, because of its two dimensional nature, a major limitation of FFDM is the superposition of breast tissue in a mammogram, which can lead to a decrease in specificity and sensitivity [2]. First demonstrated by Niklason et al. in 1997, Digital Breast Tomosynthesis (DBT) aims to partly overcome the detrimental effects of tissue overlapping and tissue masking by producing pseudo three-dimensional images of the breast [53]. This is done by acquiring several low-dose projections of the breast as the x-ray source travels over a small arc spanning a limited angular range. The projections are then combined with dedicated algorithms into a stack of tomographic planes, each reproducing the content of the breast at different depths [57].

The approval of the Hologic Selenia Dimensions as the first commercially available DBT system in 2011 by the U.S. Food and Drug Administration (FDA) marked the entrance of DBT in screening and diagnostic settings [22], [57]. Since then, the number of installations of DBT systems has rapidly been increasing and European breast cancer screening trials have been carried out, with the objective to define its clinical role [27], [29], [59].

Parallel to the evaluation of DBT detection efficacy in clinical settings, progress has

also been made in the development of methods for the assessment of technical performance and quality control of DBT imaging systems [46]. The objective of the European Reference Organisation for Quality Assured Breast Screening and Diagnostic Services (EUREF) is to promote high-quality mammo-care in Europe. To this end, its Physico-Technical Steering Group has coordinated European guidelines for quality assurance and quality control of physical and technical aspects in mammography screening [23]. These guidelines have been used as a starting point for the development of a preliminary protocol for quality control in DBT. In addition to this, DBT dedicated phantoms that simulate radiation-tissue interactions have been designed to be used for software analysis and visual Quality Control (QC) tests.

This thesis is the outcome of the work carried out during my internship with Tecnologie Avanzate TA S.r.l., Turin, Italy. As part of their Research & Development (R&D) activities, Tecnologie Avanzate is looking into developing a software for the automation of EUREF's DBT QC tests to be performed with two phantoms: CIRS DBT QC Phantom (model 021) and Mammo 3D Performance Kits. The phantoms are produced by Computerized Imaging Reference Systems Inc. (CIRS) and Sun Nuclear respectively, both part of Mirion Technologies, and are distributed by Tecnologie Avanzate.

The objective of the internship project was to assess the compliance of CIRS DBT QC Phantom and Mammo 3D Performance Kits with EUREF's DBT protocol. To this end, the activities were organised in two parts. First of all, QC tests requiring imaging targets included in both phantoms were identified and implemented. These include the evaluation of the Automatic Exposure Control system in projection images, and the analysis of the z-resolution in reconstructed stacks. Acquisitions were performed with the Hologic Selenia Dimensions system at Molinette Hospital, part of the Azienda Ospedaliero-Universitaria Città della Salute e della Scienza, Turin, and the Fujifilm AMULET Innovality system at the European Institute of Oncology (IEO) in Milan.

The second part of this study consisted in performing additional EUREF measurements using other test objects available with the phantoms, with the objective to validate their use in the physical characterisation of the two DBT systems. This involved the assessment of the image receptor response function and noise analysis, as well as the quantification of the system sharpness through the Modulation Transfer Function.

The QC measurements were implemented using the image processing software ImageJ, which enabled semi-automation through the creation of macros. The latter will serve as a starting point for the development of a fully automated software by Tecnologie Avanzate. In addition to this, given the differences in practicality and cost between the two phantoms, the results of this study will also allow Tecnologie Avanzate to resolve whether to base the software on both phantoms.

This thesis is organised in four chapters. In Chapter 1, an overview of the physical processes underlying x-ray imaging of the breast will be provided, and key technological aspects concerning mammography will be described. The focus will then shift to the DBT imaging chain, including the different acquisition geometries and the image recon-

struction process. Chapter 2 will be dedicated to quality control procedures in DBT, and the development of the EUREF protocol. The image quality parameters measured in QC settings will thus be presented, highlighting system design factors that influence them. A detailed description of the phantoms and DBT systems under evaluation will be instead provided in Chapter 3. The EUREF tests considered for the analysis will also be outlined, together with the approaches employed in the calculations. The results obtained will finally be presented and discussed in Chapter 4, where future developments of the QC software will also be mentioned.

Chapter 1

X-ray imaging of the breast

The discovery of x-rays by physicist Wilhem Röngten in 1895 marked the beginning of diagnostic radiography, which, to date, is the mainstay of medical imaging.

Mammography is radiography of the breast and, as such, is an attenuation-transmission imaging technique. A source external to the patient produces a uniform x-ray beam incident on the breast. The x-rays are then differentially attenuated by the breast according to its tissue composition (e.g., glandular or adipose), with only a fraction of the x-rays being transmitted to a detector placed below the breast. Given the variability in attenuation along the beam path, the detected signal is descriptive of the tissue characteristics that affect the transmission of x-rays, and therefore carries information on the internal anatomy [17].

Because of the two-dimensional (2D) nature of standard mammography, tissue superposition occurs, posing two major issues [53], [30]:

- Dense glandular tissue located above and/or below a lesion of interest can create a masking effect, also known as anatomical noise, and reduce the visibility of a pathology, thus decreasing sensitivity (83.5%);
- Since the signal detected at a location on the digital detector depends on the total attenuation of all the tissue between the detector and the x-ray beam, two or more normal features that are only vertically separated can be misinterpreted as the projection of a lesion. This affects specificity (90.9%).

As a consequence, tissue superposition may lead to false positives as well as false negatives and a higher recall rate. In figure 1.1 the effect of tissue superposition is shown. Because of the overlapping tissues, a lesion of interest is hidden in a 2D image, resulting in missed cancers. On the other hand, by providing thin cross-sectional slices through the imaged object, loss of information in the third dimension can be overcome [53], [57]. This is achieved with Digital Breast Tomosynthesis (DBT), a limited-angle tomographic breast imaging technique in which several projection images are acquired at different

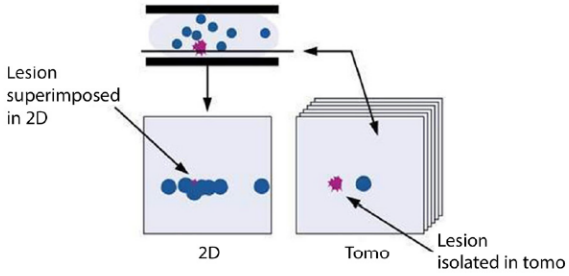

Figure 1.1: A lesion of interest is hidden by the overlapping tissues in two-dimensional mammography but is spatially resolved in tomographic planes. Source: [57].

angular positions of the x-ray source. The set of projections is then processed with a dedicated reconstruction algorithm and a series of stacked images representing the three-dimensional (3D) distribution of the tissues is obtained [53].

In the following, the anatomy of the breast together with the different types of breast abnormalities will be first described, in order to identify the imaging objectives in mammography and the challenges they entail. Then, key physical aspects of x-ray imaging will be introduced, such as radiation-matter interaction mechanisms, x-ray production and contrast information. This will lay the grounds for the understanding of the physics of Digital Breast Tomosynthesis and how image quality parameters are derived.

1.1 Anatomy of the breast and breast cancer

A healthy breast is organised into 15-25 sections called lobes, which can vary in shape and size and are separated through connective and adipose tissue (supporting stroma). Each lobe is made up of smaller epithelial structures called lobules which in turn contain secretion units called alveoli, where milk is produced and stored during lactation. The lobes are then drained through a network of radially arranged milk ducts which exit at the nipple.

A mature female breast contains a balanced amount of ducts, fibroglandular stromal tissue, and fat. Later in life, from about 40 years of age, the percentage of lobular and ductal breast tissues in the breast starts decreasing, with the connective tissue and fat making up the larger proportion [37]. The basic functional and histo-pathological unit of the breast is the terminal duct lobular unit (TDLU) which consists of a small segment of the terminal duct and the lobules. Evidence suggests that breast cancer is a collection of different diseases with different clinical appearance and pathological features, mostly originating from the TDLU [1]. Most breast cancers are carcinomas, which are tumours that form in epithelial tissue. Carcinomas that start in the breast ducts or lobules are usually called adenocarcinoma. Breast cancers can be classified

Figure 1.2: Vertical cross section of a healthy mature female breast, showing the lobules and ducts embedded in breast stroma (fibrous, connective and adipose tissues). Source: Adapted from [37].

into subgroups according to their histopathological grade and type. The former is an indication of the degree of differentiation and proliferative activity of a tumour, and therefore describes its aggressiveness. The histopathological type, on the other hand, refers to the growth pattern of the tumours. With a prevalence of 70-80% [58], invasive ductal carcinoma (IDC) is the most common adenocarcinoma in which cancer cells have spread through the lining of the ducts into the surrounding breast tissue [49]. It may appear as masses, often of irregular or "spiculated" margins . Contrary to IDC, ductal carcinoma in situ (DCIS) is a cancer precursor, that, as the name suggests, is also found in the milk ducts, but is non-invasive. This type of cancer may show on a mammogram as clusters of microcalcifications, which are small calcium deposits, of approximately 100 µm, resembling white specks [1].

1.2 X-ray interactions with matter

Diagnostic radiology is based on the use of the electromagnetic energy spectrum as a form of radiation, with the spectral energy band differing between imaging modalities.

As it can be seen in figure 1.3, x-rays are electromagnetic (EM) waves which propagate in space or through a medium at frequencies varying from about 10^{17} Hz (soft x-rays) to nearly 10^{20} Hz (hard x-rays), and wavelengths ranging from several nanometres down to 10^{-12} m. X-rays used for diagnostic purposes can reach energy values of up to 10^5 eV, where 1 eV is equal to the kinetic energy gained by an electron in a vacuum accelerated by a potential difference of 1 V [55]. At such high energies radiation-matter interactions

are collisional in nature and ionisation of the medium can take place [55]. For this reason, electromagnetic radiation beyond the far ultra violet (UV) region of the electromagnetic spectrum is classified as ionising. The ionisation energy is the minimum energy required

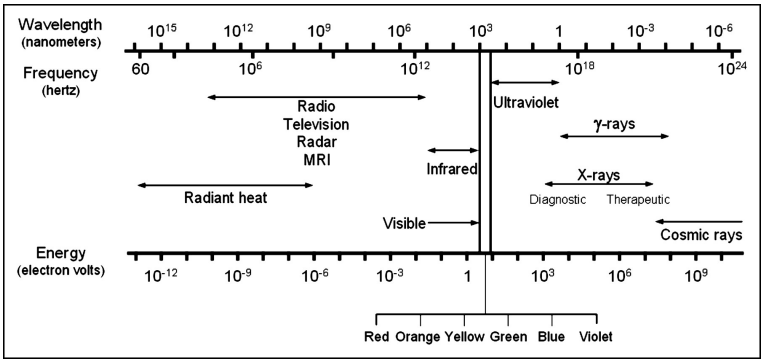

Figure 1.3: The electromagnetic spectrum. Source: [55].

to ionise an atom or molecule and depends on the type and state of matter. For instance, the ionisation energy for liquid water is 11.2 eV. Since water is the most abundant molecule in the human body, radiation with energies below 11 eV is considered non-ionising [17].

X-ray photons crossing a medium may either be transmitted without interacting, scattered or completely absorbed. Attenuation is the removal of photons from an x-ray beam caused by absorption and scattering events and it is mathematically described by the Beer-Lambert law [17]:

$$N = N_0 \cdot e^{-\mu x}, \tag{1.1}$$

where N is the signal produced by an incident x-ray beam of initial intensity N_0. The quantity μ is the linear attenuation coefficient which describes the fraction of x-rays removed from a mono-energetic beam per unit thickness of material x. The linear attenuation coefficient therefore describes the probability of interaction between radiation and matter.

Given a material of a certain thickness, the probability of interaction is proportional to the number of atoms per volume. To overcome this dependency, the mass attenuation coefficient $(\mu/\rho)[\mathrm{cm}^2/\mathrm{g}]$ is used, which is a normalisation of μ per unit density ρ of the material. As it can be seen in figure 1.4, the total mass attenuation coefficient is given by the contributions from different interaction mechanisms. In general, photons crossing a medium can undergo the following interactions:

- Photoelectric effect;
- Rayleigh scattering;
- Compton scattering;

- Pair production.

The total mass attenuation coefficient is therefore:

$$\frac{\mu}{\rho} = \frac{\sigma}{\rho} + \frac{\tau}{\rho} + \frac{\kappa}{\rho} \tag{1.2}$$

where σ, τ and κ are the probabilities, or cross sections, of the photoelectric effect, scattering and pair production interactions respectively. Within the x-ray energy range,

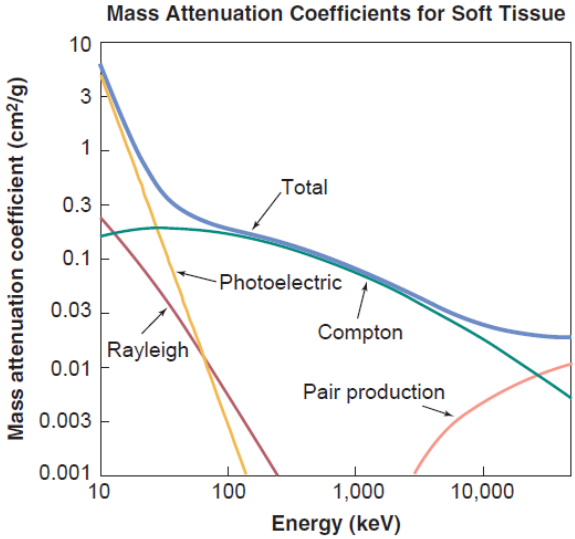

Figure 1.4: Total mass attenuation coefficients for soft tissue as a function of beam energy, together with the contributions from different x-ray interactions with matter. Source: [17].

the interaction mechanisms responsible for the attenuation of the x-ray beam are the photoelectric effect and the scattering interactions. Pair production is instead a nuclear interaction between a photon and the nucleus of an atom, occurring at energies in the order of MeV. For this reason, it will not be included in the discussion that follows.

1.2.1 Photoelectric effect

In the photoelectric effect, a photon transfers all its energy to an atomic electron, usually located on the innermost shell of the atom, designated K, and therefore tightly bound to the atom. As a result, the electron is ejected from the atom and deposits its energy in its surroundings. The energy of the ejected electron, also referred to as photoelectron, is:

$$E_{\mathrm{pe}} = E_0 - E_{\mathrm{b}}, \tag{1.3}$$

where E_0 is the incident photon energy and E_b is the binding energy of the orbital electron [17]. The photoelectric effect can only take place if the photon energy is sufficiently high to overcome E_b and is most likely to occur with electrons whose binding energy is close to but less than the incoming photon energy.

After a photoelectric interaction the atom is ionised and in an excited state. The vacancy left by the ejected electron is then occupied by an electron from an outer shell of lower binding energy, creating another vacancy. The latter will therefore be filled by an electron from an even outer shell, and so on. The result of this de-excitation process is the cascaded emission of characteristic x-rays whose energy is equal to the difference between the shell binding energies. Figure 1.5 shows the emission of a K_α x-ray due to the transition of an electron from the L shell to the vacancy created in the K shell by the photoelectron. Given the principal quantum number n characterising an atomic shell, the subscript α in K_α denotes a transition from a shell $n+1$ to shell n. Alternatively

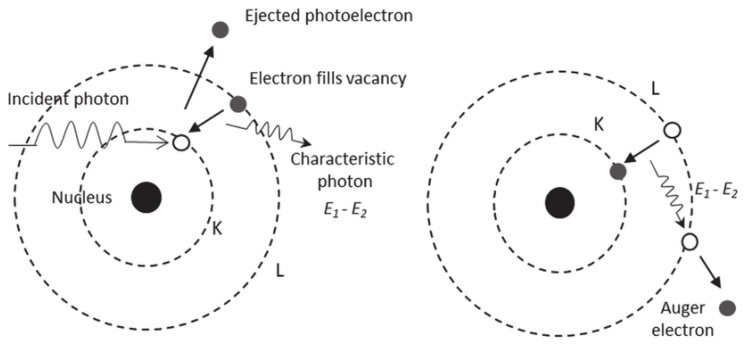

Figure 1.5: Schematic representation of the photoelectric effect followed by de-excitation processes: emission of a characteristic x-ray (left) and of an Auger electron (right). Source: [44].

to the emission of characteristic x-rays, the difference in binding energies can also be released as Auger electrons. An electron of the outer L shell in figure 1.5 absorbs the excess energy $E_1 - E_2$ and is emitted from the atom.

As it is shown in figure 1.4, the cross section for the photoelectric effect decreases as a function of the photon energy E and increases with the atomic number Z of the material the photons interact with. More specifically, $\sigma \propto E^{-3.5}$ and $\sigma \propto Z^4$. For this reason, the photoelectric effect is dominant when low energy photons interact with high Z materials. This means that, in the energy range used in mammography (20-40 keV), the photoelectric effect is an important contribution to beam attenuation, despite the low Z ($Z \approx 20$) of soft tissues [17].

1.2.2 Scattering: Rayleigh and Compton

Rayleigh scattering, also known as coherent scattering, is an excitation process in which the electric field of the incoming x-rays causes the atomic electrons to oscillate in phase. The oscillating electrons thus emit radiation of the same λ, giving rise to an interference phenomena. Interference is constructive at small incidence angles of the x-ray beam, and destructive at greater angles. For this reason, the emitted radiation is slightly deflected in direction. Rayleigh scattering cross section $\tau_{\text{coh}} \propto E^{-2}$, and this behaviour is reflected by the corresponding curve in figure 1.4. This indicates that Rayleigh scattering is appreciable at low x-ray energies such as the ones used in mammography and this could degrade image quality. However, since $\tau_{\text{coh}} \propto Z^{2.5}$, in soft tissues only about 10% of interactions at 30 keV are Rayleigh scattering, making it negligible in diagnostic applications [17].

Unlike Rayleigh scattering, Compton scattering is an inelastic collision in which a photon undergoes a change in energy and direction. In figure 1.6, an incident photon of energy E_0 scatters off a quasi-free outer shell electron ($E_0 \gg E_{\text{b}}$) at an angle θ. The electron, on the other hand, recoils with kinetic energy E_{e^-} at an angle ϕ. As a result,

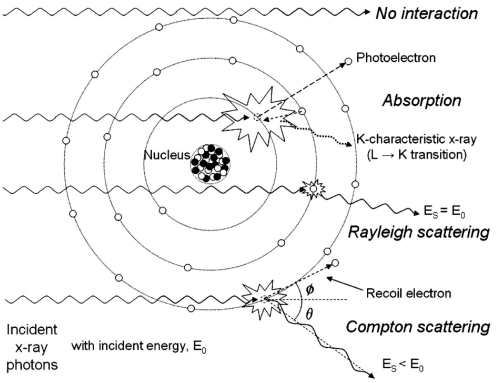

Figure 1.6: X-ray interactions with matter in the diagnostic energy range. Source: Adapted from [55].

the atom is ionised and E_0 is distributed between the scattered photon and the ejected Compton electron:

$$E_0 = E_{\text{S}} + E_{e^-}, \tag{1.4}$$

where E_{S} is the energy of the scattered photon and, for a photon scattering angle θ, is given by:

$$E_{\text{S}} = \frac{E_0}{1 + \frac{E_0}{511\text{keV}}(1 - \cos\theta)} \tag{1.5}$$

where 511 keV is the rest mass energy of the electron. Equation 1.5 indicates that, for a given θ, E_{S} decreases for higher E_0 and most of the incident energy is transferred to the

scattered electron. Moreover, when a scattering angle of 180° is considered (backscattering), E_S reaches its minimum value and the electron receives the maximum attainable energy. for a given E_0.

The probability a photon is scattered in the solid angle element $d\Omega$ is given by the Klein-Nishina formula, through which it is possible to calculate the angular distribution of the scattered photon. Figure 1.7 shows the scatter distribution probability as a function of the scattering angle, for incident photon energies of 20 keV, 80 keV and 140 keV. At low energies ($\approx$ 20 keV), the angular distribution is symmetric and the photon

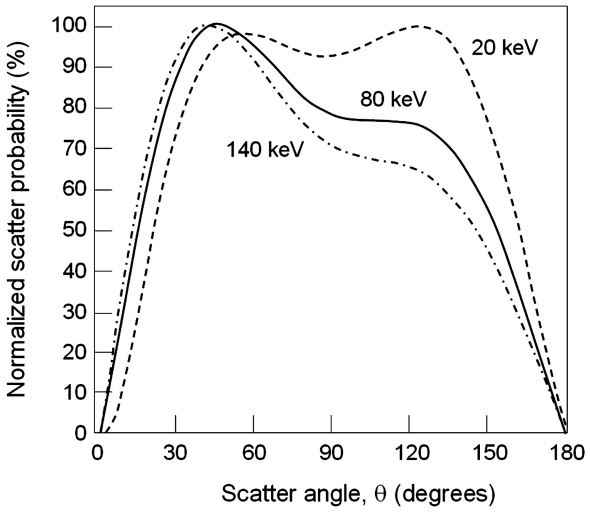

Figure 1.7: Compton scattering probability as a function of scattering angle for different incident photon energies. Source: [55].

is either front ($\theta \approx 0°$) or backscattered ($\theta \approx 180°$). On the other hand, as the energy increases to values close to 140 keV, scattering in the forward direction is predominant. Photons scattered in the forward direction are more likely to reach the image receptor and are therefore detrimental to the image quality.

In order for Compton scattering to occur, the photon energy must surpass the electron binding energy E_b. For this reason, unlike the photoelectric effect and Rayleigh scattering, the probability of a Compton interaction increases as a function of the x-ray beam energy. As it can be seen in figure 1.4, within the diagnostic x-ray energy range ($\approx$ 20-80 keV) the probability of Compton scattering remains roughly constant but, at higher energies, it decreases as approximately $1/E_0$. In addition to this, the probability of interaction also depends on the electron density of the material. Since the number of electrons per unit mass is more or less constant, given the equal number of protons and neutrons in the nucleus, the Compton probability per unit mass is independent of Z. Given the absence of neutrons in the hydrogen nucleus, the electron density in hydrogenous material is greater and Compton scattering is more likely to occur [17], [55].

1.2.3 X-ray generation

X-ray production is the result of collisional and radiative interactions of high energy electrons with a target in vacuum. Figure 1.8 illustrates the main components of an x-ray tube, which consists of two electrodes, the cathode and anode, separated by a small distance (about 1–2 cm) in a vacuum enclosure, made of either glass or metal. The cathode consists of a heated filament and a focusing cup from which electrons are emitted via thermionic emission. The electrons are then accelerated in a potential difference to the anode, in which a target of high Z material, usually tungsten, W ($Z = 74$), is embedded [55].

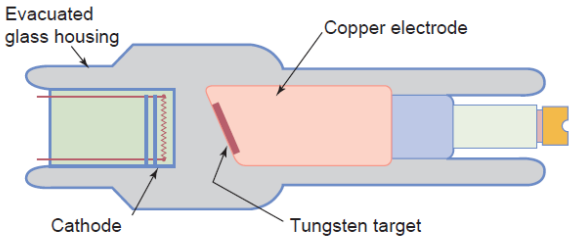

Figure 1.8: Schematic representation of an x-ray tube containing a tungsten (W) target. Source: [17].

Electrons are light charged particles and as such, can lose their energy via inelastic collisions or radiative losses, with the emission of Bremsstrahlung or braking radiation. While inelastic collisions take place at low electron energies, energy loss via Bremsstrahlung radiation is predominant at higher energies and increases as a function of Z^2. Radiative losses occur if an accelerated electron comes in close proximity with the nucleus of a target atom, and is decelerated by the coulombic attractive forces due to the protons in the nucleus. The energy lost by the electrons is then emitted as x-rays which constitute the braking radiation. As well as the electron energy, the energy of the emitted x-rays also depends on the impact parameter b, that is the perpendicular distance between the path of a projectile and the position of the target nucleus. In figure 1.9 a typical x-ray spectrum obtained from an x-ray tube operating at a potential difference of 90 kV is reproduced. As it can be seen, the spectrum is constituted by a continuous range of energies of Bremsstrahlung radiation, representing a polychromatic x-ray beam. The maximum achievable photon energy is given by the peak potential difference applied between the tube electrodes, which is referred to as *kilovoltage peak* (kVp).

The effective energy of a polychromatic beam can be measured from the Half Value Layer, *HVL*, which is the thickness of material required to reduce the intensity of a beam to half of its initial value. Narrow beam geometry is an experimental configuration in which the x-ray beam is collimated so that scattered photons are prevented from reaching

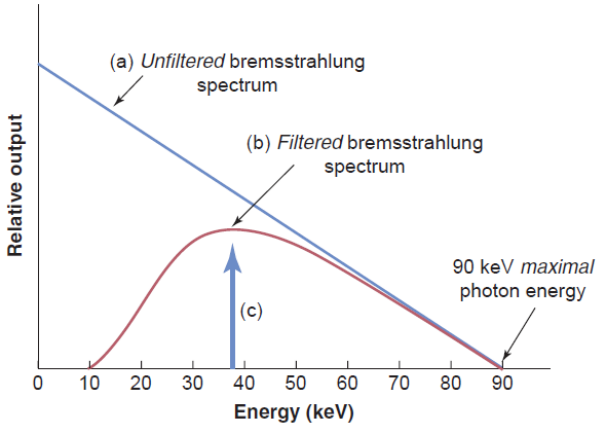

Figure 1.9: Typical x-ray spectrum obtained by applying a potential difference of 90 kV. Source: [17].

the detector. Under these conditions, the HVL measured in millimetres of aluminium can be used as an estimate of the penetrability of a diagnostic x-ray beam. For a mono-energetic beam:

$$HVL = \frac{0.693}{\mu} \tag{1.6}$$

which is obtained by setting $N = N_0/2$ in equation 1.1. Once the HVL is experimentally determined, the linear attenuation coefficient μ can be computed according to the expression in equation 1.6. Hence, given μ, the effective energy can be obtained, which is an estimate of the penetration power of a polychromatic beam, expressed as the energy of a mono-energetic beam that would exhibit the same effective penetrability. The effective energy is usually between 1/3 and 2/3 the maximum value and is indicated by the blue arrow in figure 1.9.

Along with the quality of the photons generated, the tube voltage also determines their quantity, which is denoted by the area under the curves in figure 1.9. An increase in kVp therefore determines a shift of the spectrum towards higher energy values, as well as an increase in the photon intensity. A measure of the radiation produced is provided by the quantity *milliampere-seconds*, which is commonly known as mAs. As the name suggests, the mAs is given by the product of the tube current, determined by the production of electrons inside the tube and expressed in milliamperes (mA), and the exposure time measured in seconds. Consequently, the mAs can be changed by either adjusting the tube current or the duration of electron emission. In clinical settings, changes to the mAs are mostly achieved by tuning the tube current, since longer exposure times entail higher likelihood of patient motion, hence image quality degradation.

The red curve in figure 1.9 represents the x-ray spectrum once it has exited the x-ray tube. The non-zero value of the minimum photon energy is due to the filtering of

the lower energy photons, caused by the tube material located at the tube exit. This is an example of beam filtration which consists in shaping the energy distribution of the x-ray beam through the use of filters of specific materials. Moreover, as the x-ray beam traverses matter, whether it be filters or the patient, the x-ray spectrum is shifted to higher effective energies, following the removal of lower energy photons. This phenomenon is known as beam hardening and it only concerns polychromatic beams. Filtration, kVp and mAs are the primary settings that can be adjusted on x-ray machines to control the image quality and dose to the patient.

As it was mentioned above, electrons can also undergo collisional interactions and these are actually the dominant contribution to their energy loss. If the electron energy exceeds the binding energy of a shell electron in a target atom, the latter is ionised and a vacancy in the corresponding shell is created. This leads to the transition of a shell electron of greater binding energy to the newly created vacancy, and the emission of the excess energy as a characteristic x-ray. As a result, discrete characteristic energy

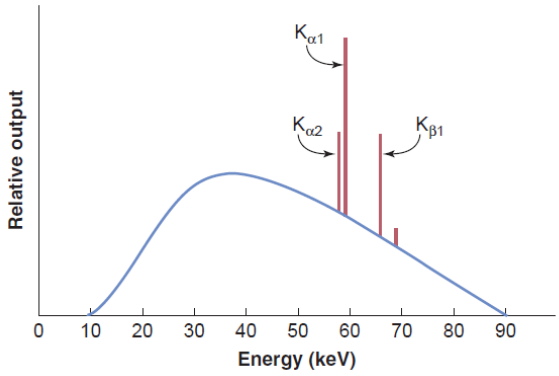

Figure 1.10: Filtered Bremsstrahlung spectrum, on which the characteristic x-rays $K_{\alpha1}$, $K_{\alpha2}$ and $K_{\beta1}$ are superimposed. Source: [17].

peaks are superimposed on the continuous Bremsstrahlung spectrum, with their values depending on the anode material. For example, figure 1.10 shows the characteristic x-rays produced from a tungsten target. The peaks $K_{\alpha1}$, $K_{\alpha2}$ are due to the transition to the K shell ($n = 1$) of electrons from an L shell, whereas $K_{\beta1}$ is emitted when the vacancy is filled by an electron from an M shell. As it will be described in the next sections, the production of characteristic x-rays is the basis for beam filtration for the optimisation of beam quality.

Since inelastic collisions represent the vast majority of electron-target interactions, x-ray production by an x-ray tube is an inefficient process resulting in heat generation. This is taken into account when choosing the target material, which should be characterised by good thermal conductivity [39]. Moreover, the effect of inelastic collisions is mitigated by a rotating anode design, in which the heat is spread over a larger area, thus providing

greater heat loading [17].

An x-ray tube is also characterised by a focal spot size, that is the area of the anode on which the electrons are incident, determined by the length of the cathode's filament. The effective focal spot size is the projected size shown in figure 1.11 and, for a given

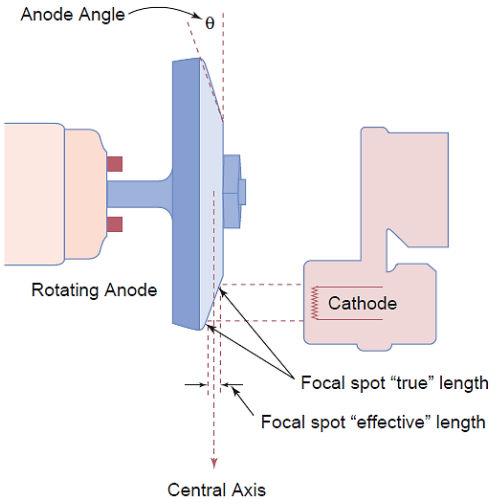

Figure 1.11: X-ray tube design factors affecting the focal spot size, namely the filament length and anode angle θ. Source: [17].

filament length, it is affected by the angle between the anode surface and the central ray in the x-ray field, that is the central axis in figure 1.11. More specifically, a small filament length and a large anode angle result in a small effective focal spot. Likewise, a large filament length, but with a small anode angle also produce a small effective focal spot. Typical anode angle values are 7°-20°, resulting in a Field of View (FOV) of the produced x-ray beam of variable size.

All things considered, since the focal spot size affects the spatial resolution attainable by an imaging system, and the anode angle determines the FOV, the design of an x-ray tube depends on its clinical application. With regards to mammography, a small focal spot size of 0.3 mm is required for the detection of microcalcifications [39]. Moreover, in order to reach a field coverage of 24 x 30 cm^2, the x-ray tube is tilted so that an effective anode angle of at least 22° is obtained, also taking into account the actual anode angle θ, which can vary between 0° and 16° [17].

1.3 Imaging requirements in mammography

As it was previously mentioned, transmission projection radiography is based on the differential attenuation of an x-ray beam as it encounters different tissues along its path.

This dependence on the tissue composition appears in the Beer-Lambert law as the linear attenuation coefficient μ. Since μ determines the degree of attenuation, features in the breast will be more or less visible in a mammogram according to the attenuation coefficient that characterises the type of tissue, in other words, they will have a different subject contrast. Figure 1.12 shows an object containing a detail, represented by the

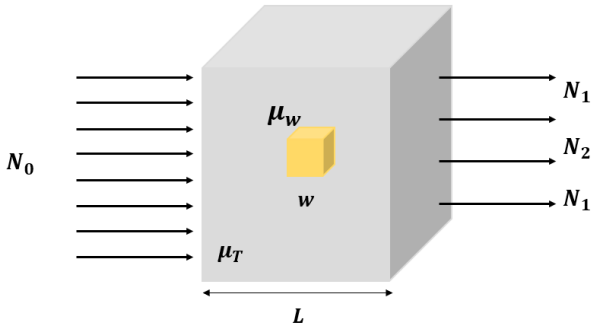

Figure 1.12: Schematic representation of the differential attenuation of an x-ray beam, due to the different attenuation coefficients μ_T and μ_w. Source: Adapted from [39].

yellow cube of width w in a uniform background. The signal produced by an incident x-ray beam of intensity N_0 can be calculated by applying the Beer Lambert Law. However, the background and the detail have different linear attenuation coefficients, μ_T and μ_w respectively. As a consequence, the signal N_1 corresponding to a region containing background only will differ from N_2, the number of photons emerging from the region containing the detail. More specifically:

$$N_1 = N_0 e^{-\mu_T L} \tag{1.7}$$

$$N_2 = N_0 e^{-[\mu_T \cdot w + \mu_T (L-w)]}. \tag{1.8}$$

Multiplying out the exponent in the expression for N_2, one gets

$$\begin{aligned} N_2 &= N_0 e^{-\mu_T L} \cdot e^{-w[-\mu_T + \mu_w]} \\ &= N_1 e^{-w[\mu_w - \mu_T]}. \end{aligned} \tag{1.9}$$

Using the expressions in equations 1.7 and 1.8, the subject contrast between the two regions is therefore

$$\begin{aligned} C = \frac{N_1 - N_2}{N_1} &= 1 - \frac{N_2}{N_1} \\ &= 1 - e^{-w[\mu_w - \mu_T]} \\ &\approx (\mu_w - \mu_T) w. \end{aligned} \tag{1.10}$$

The result obtained in equation 1.10 indicates that contrast between two regions depends on the difference between the linear attenuation coefficients characterising those regions, and on the thickness of the detail. That is, contrast depends on the absorption properties of the tissues constituting the object being imaged. Moreover, contrast is independent of the number of photons, hence changes to the amount of the radiation imparted leave contrast unaffected. Since adenocarcinomas are made of epithelial tissues,

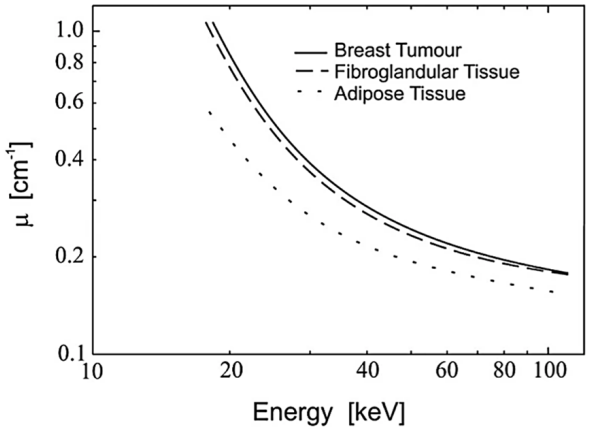

Figure 1.13: Linear attenuation coefficient as a function of energy for adipose and fibroglandular tissues, and breast carcinoma. Source: [60].

the difference in the attenuation of an x-ray beam by normal and cancerous tissues is very small. This is shown in figure 1.13 where the linear attenuation coefficient for fat, glandular and cancerous tissues is plotted as a function of beam energy. As it can be seen, the curves corresponding to the glandular tissues and the breast tumour are almost overlapping, indicating that discrimination between the two in a mammogram is challenging. For this reason, an appropriate level of contrast resolution is required.

In addition to this, figure 1.13 also shows that at lower beam energies the attenuation curves corresponding to the glandular and cancer tissues are slightly distinct, before converging at higher beam energies. Because of this, contrast in mammography can be optimised through the use of a low energy x-ray spectrum. Indeed, since $\sigma \propto E^{-3.5}$, attenuation due to photoelectric interactions is important, and contrast is improved thanks to the differential absorption according to the tissue type.

The underlying assumption of projection radiography is that the photons reaching the detector will have travelled along straight lines. This is only applicable in the absence of scattering interactions with the medium. In fact, as it can be seen in figure 1.4, in the energy range used in x-ray imaging, the contribution of scattering to the mass attenuation coefficient is significant. Under these circumstances, a degradation of image quality in terms of loss of contrast is to be expected.

The presence of scattering in an image can be quantified by introducing a term S

in the definition of contrast, which represents an additive, gradually varying radiation distribution that degrades subject contrast and adds random noise [17]:

$$C = \frac{(N_1 + S) - (N_2 + S)}{N_1 + S} = \frac{N_1 - N_2}{N_1 + S} = \frac{1 - e^{-w[\mu_w - \mu_T]}}{\left(1 + \frac{S}{N_1}\right)}. \tag{1.11}$$

The expression in equation 1.11 indicates that, in the presence of scattering, contrast is reduced by the factor $\left(1 + \frac{S}{N_1}\right)$, where $\frac{S}{N_1}$ is the scatter to primary ratio, *SPR*. The *SPR* is the amount of scattered radiation S with respect to the primary radiation N_1, consisting of the detected photons that have travelled along a straight line and therefore carry information regarding the attenuation characteristics [17]. In general $SPR \geq 0$. The contrast degradation factor is defined as

$$CDF = \frac{C_\mathrm{s}}{C_0} = \frac{1}{1 + SPR} \tag{1.12}$$

where C_s is contrast in the presence of scattered radiation, whereas C_0 is contrast resulting from primary radiation only, hence it represents the maximum attainable subject contrast [39].
Knowledge of the acquisition factors that influence scattering can help maintain an adequate level of contrast. Namely:

- Beam energy: as it is illustrated in figure 1.13, the probability for scattering varies as a function of the energy of the x-ray beam;
- Thickness of the object to be imaged: the greater the thickness, the higher the probability for interaction, since photons will travel longer paths;
- The area of the x-ray field, FOV: beam collimation ensures that scattered photons do not reach the detector.

Figure 1.14 shows the increase in the scatter to primary ratio as the x-ray field of view and the object thickness are also increased, at a beam energy of 100 kVp. Given this behaviour, it is possible to reduce the *SPR* thus improve contrast by acting on the FOV and the object thickness.

All in all, mammography comes with several imaging challenges resulting from the anatomy of the breast and the detection goals. In order to address these needs, mammographic equipment and detectors differ from those used in general radiography [17]. For instance, x-ray tubes with specific anode/filter combinations to obtain appropriate beam qualities, the use of an anti-scatter grid to limit the level of scattering and high efficiency detectors. All of these aspects will be discussed in detail in the sections that follow.

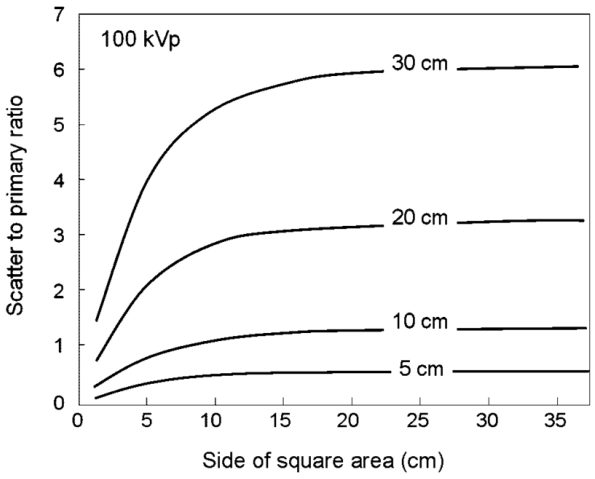

Figure 1.14: Scatter to primary ratio, *SPR*, at 100 kVp for different object thickness values as a function of area irradiated. Source: [55].

1.3.1 Beam filtration in mammography

In the previous section, the importance of the optimisation of contrast resolution, whilst keeping dose levels within acceptable limits, was highlighted. To this end, specific anode filter combinations and kV values are selected, with the objective to obtain beam qualities which are tailored to the detection needs in mammography. While tungsten is the most common anode material used in general radiography, molybdenum (Mo) and rhodium (Rh) are often chosen in mammography. This is because the energies of the K-shells of Mo (17.5 keV and 19.6 keV) and Rh (20.2 keV and 22.7 keV) fall within the optimal energy range for mammography. As a consequence the number of x-rays in that energy range is increased by characteristic x-ray emission [17]. As an example, figure 1.15 shows the unfiltered x-ray spectrum produced by a Mo target. Looking at the superimposed attenuation curve for Mo, one can see that the characteristic x-ray lines occur at the lowest attenuation of the filter.

In order to selectively remove the lowest and highest energy x-rays, x-ray tube filters made from elements with K-absorption edge energies between 20 keV and 27 keV are used. These include Mo, Rh and Ag. In addition to these alumnium (Al) is used in DBT. As a result, only a narrow band of x-ray energies is transmitted, from about 15 keV up to the K-absorption edge of the filter [17]. Since the choice of a specific target-filter combination determines the x-ray spectrum, the breast thickness and tissue composition must be taken into account. For instance, a denser and thicker breast requires an x-ray beam of higher penetrating power.

Since the introduction of FFDM, which allows for post-acquisition image processing, the advantages of tungsten (W) in terms of x-ray production efficiency and improved

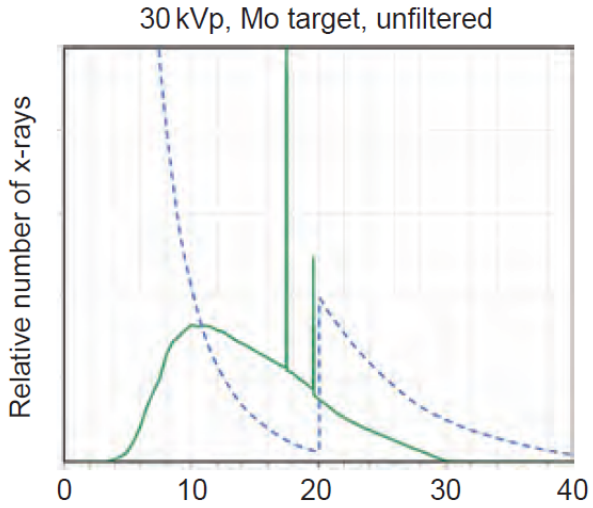

Figure 1.15: Unfiltered x-ray spectrum resulting from a Mo target, showing the continuous Bremsstrahlung radiation and the characteristic x-ray lines at 17.5 keV and 19.6 keV. The dashed curve represents the linear attenuation coefficient of Mo. Source: [17].

heat loading have made it the preferred choice of target material [17]. Most digital breast tomosynthesis systems use a W target whereas an Al filter is usually used to reduce dose. The reason for this is shown in figure 1.16, where the attenuation curves

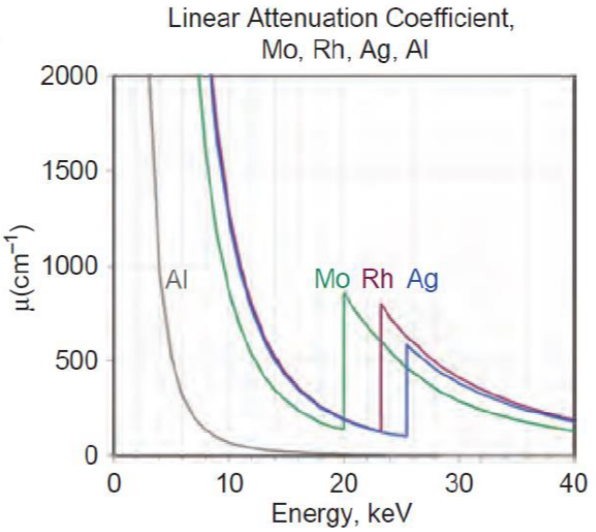

Figure 1.16: Attenuation curves of Mo, Rh, Ag and Al filters. Source: [17].

for Mo, Rh, Ag and Al are plotted. Looking at the curve corresponding to the Al filter, it can be seen that the attenuation of low energy x-rays is higher compared to

the attenuation caused by other filters. Moreover, the absence of characteristic x-ray lines resulting from the choice of a W-Al combination is compensated by the contrast enhancement tomosynthesis reconstruction algorithms can provide.

1.3.2 Compression of the breast and the anti-scatter grid

In the mammography energy range (20 to 40 keV) scatter is a dominant contributor to x-rays attenuation. However, by inspecting the cross section curves in figure 1.13 it is possible to note that the scattering component is roughly constant in the energy range used in mammography. This means that the amount of scattered radiation is independent on kV and is mostly affected by the breast thickness and the FOV size. In fact, similarly to figure 1.14, figure 1.17 shows the *SPR* plotted as a function of the diameter of a semi-circular field area aligned to the chest wall edge, this time for different breast thickness values [17]. The graph shows that for a breast thickness of 6 cm, the

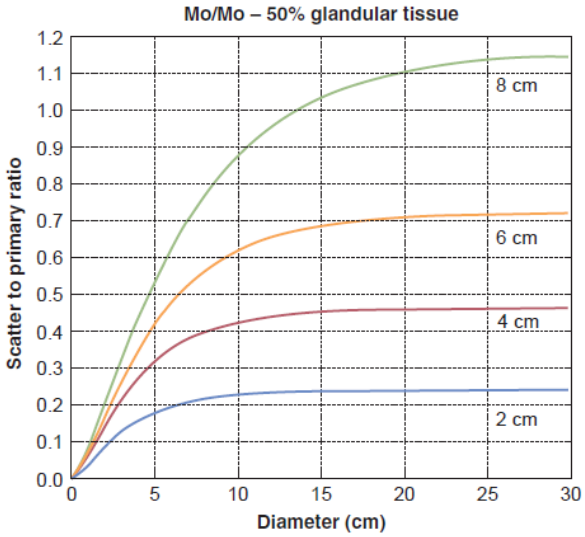

Figure 1.17: Scatter to primary ratio for different breast thickness values as a function of irradiated area. Source: [17].

SPR is approximately 0.6. Using equation 1.12, the resulting *CDF* is about 62.5%, meaning that only a fraction of subject contrast is transmitted. Since the *SPR* increases as a function of thickness, compression of the breast is a key part of a mammographic procedure. Indeed, during an examination the breast is placed on the breast support table and compressed by a compression paddle consisting of a thin polycarbonate (Lexan) plate. In addition to a reduction of scattered radiation, breast compression comes with several other advantages. Namely, lower radiation dose to tissue, the equalisation of breast thickness ensuring constant image quality throughout the image, spreading out of

overlapping anatomy and a reduction of motion of the breast, resulting in less geometric blurring [17].

In 2D acquisitions, the amount of scattered radiation reaching the image receptor is also reduced by collimating the x-ray beam through the use of an anti-scatter grid. Placed between the patient and the detector, the anti-scatter grid consists of inter-space material layers (e.g., carbon fibre) alternated with x-ray absorbing septa regions usually made of lead (Pb). The geometry, shown in figure 1.18, is such that the inter-space

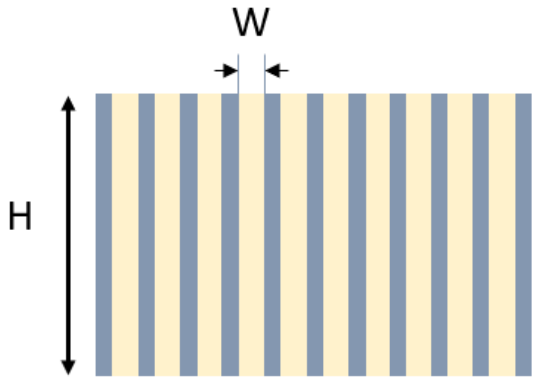

Figure 1.18: Geometry of a linear anti-scatter grid. Source: Adapted from [39].

material and the septa are aligned with the x-ray tube focal spot. This is essential in order for the primary photons, travelling along straight lines, to reach the detector, and the scattered radiation exiting the patient to be absorbed by the septa. An antiscatter grid is characterised by the grid ratio G, which is the ratio of the height of the inter-space material H to its width W. Typically in mammography $G \approx 5$ [17]. It is worth pointing out that the anti-scatter grid as shown in figure 1.18 cannot be used in DBT acquisitions since, as the x-ray tube moves along an arc, the x-ray tube focal spot and the grid lines are no longer aligned.

1.3.3 Detector technology

Before the introduction of digital detectors, a mammography system was only based on analogue screen film image receptors, consisting of a cassette, an intensifying screen (usually phosphor), and a light-sensitive film. The incoming x-rays induce visible light emission from the phosphor screen, a phenomenon known as luminescence. The incident light pattern is then recorded by a layer of emulsion material featuring on the film, and a latent image is formed. The response of the film is measured in terms of the optical density OD, which describes the darkening of the film upon irradiation, and is defined

as

$$OD = \log_{10} \frac{I_0}{I_t} \tag{1.13}$$

where I_0 and I_t are the incident and transmitted light intensities respectively. A film characteristic curve, shown in figure 1.19, relates the OD to the incident radiation exposure and, as it will be described later on in this thesis, a curve of this type is known as the response function of a detector. The subject contrast as defined in equation 1.10

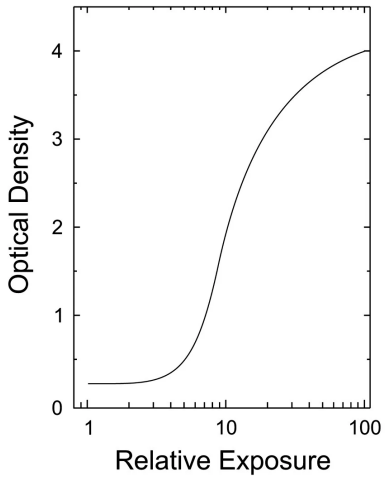

Figure 1.19: A film characteristic curve relating the optical density OD to the logarithm of the radiation exposure. Source: [60].

is converted to OD differences according to the film's characteristic curve. Given the non-linearity of the curve, this will result in variable contrast in the film image.

Screen-film mammography was the known gold standard for x-ray breast imaging during the transition to digital detectors in the early 2000's. For this reason, it was of utmost importance to develop a new technology which would continue to meet the spatial resolution requirements for the detection of microcalcifications, and, at the same time, overcome the shortcomings of screen-film based systems (e.g., limited contrast resolution and variability, and film-processing artefacts).

Full Field Digital Mammography (FFDM) is mostly based on flat panel detectors consisting of a thin film transistor (TFT) array. Each detector element, i.e., the pixel, contains a charge collection electrode, a charge storage capacitor and a transistor which acts as an on-off switch in the signal readout step. TFT flat panel detectors can either operate on direct or indirect x-ray conversion. In indirect conversion detectors, incoming ionising radiation interacts with a scintillator material which emits light in the visible or UV region as a de-excitation process. Scintillation photons are emitted in all directions and a fraction, which is determined by the scintillator's light collection efficiency, reaches a photodetector. The photodetector is a light sensor whose purpose is to convert the

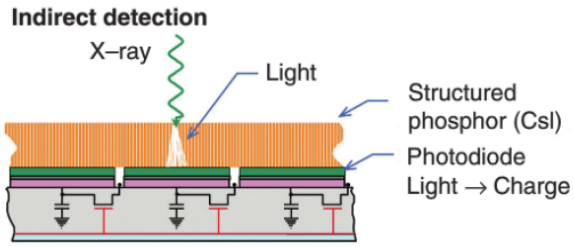

Figure 1.20: Components of an indirect conversion detector. Source: Adapted from [17].

absorbed photons into an electrical charge and amplify the signal. There are two types of photodetectors: photomultiplier (PM) tubes and silicon photodiodes.

In a PM tube, a photocathode of high Z material absorbs the incoming light photon and emits a photoelectron of about 1 eV. The photoelectron is then accelerated in a vacuum to an electrode, where it deposits an energy of a few hundred electron-volts. This results in the emission of secondary electrons and the offset of an avalanche process taking place over a series of dynodes, and ending with an electron gain of the order of 10^6. On the other hand, the photodiode is a semiconductor device made of a thin layer of silicon in which the absorption of scintillation light induces the creation of electron-hole pairs. These charge carriers are then collected by the anode and cathode of the photodiode.

The most common scintillator detector used in mammography is structured Cesium Iodide (CsI) in which the scintillator material is shaped as a needle. The CsI is in turn coupled to a photodiode and TFT matrix, which together form the receptor sensitive area (figure 1.20). In direct conversion detectors the scintillator is replaced by a semiconductor material which is placed between two electrodes. The x-ray radiation impinging on the semiconductor material induces the production of electron-hole pairs, and an applied voltage causes the electrons and holes to travel to their respective electrode. Figure 1.21 shows a typical semiconductor detector used in digital mammography, in which the strucutred CsI is replaced with an amorphous selenium (a-Se) layer. Given the direct conversion mechanism, the photodiode is also missing.

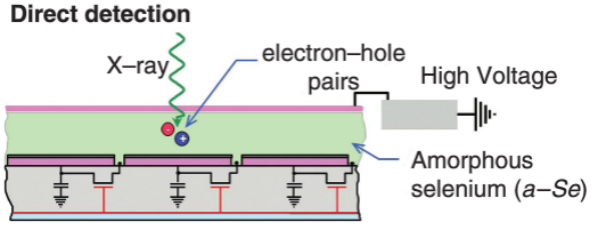

Figure 1.21: Components of a direct conversion detector. Source: Adapted from [17].

The performance of a detector is quantified via the Quantum Detection Efficiency,

QDE, which, in general terms, describes the fraction of the input photons contributing to the signal formation. With reference to scintillator detectors, the *QDE* is the ratio between the number of emitted electrons in a PM tube or photodiode, and the number of light photons reaching the photodetector. It is therefore related to the scintillation efficiency, which is the number of light photons emitted, per unit energy absorbed.

The type of detector and its geometrical features affect the spatial resolution of an imaging system, which, in general terms, is the minimum distance at which details are distinguishable. The width of the system's response function to a perfectly collimated radiation beam, also known as pencil beam, is an indication of the spatial resolution. Regarding scintillators which emit light throughout a full solid angle, the spreading of the signal reaching the photodetector depends on the distance between the interaction point and the photodetector or, in another words, the thickness of the scintillator. For this reason, thin scintillators would provide better spatial resolution, at the expense of the scintillation efficiency, which would be inevitably reduced if the available scintillation material is decreased. A compromise between spatial resolution and scintillation efficiency is indeed found in the needle shaped CsI used in mammography. In semiconductor detectors, however, signal spreading is inherently missing since the electrons are accelerated towards the TFT matrix by the electric field acting between the two electrodes [17], [47], [40].

The spatial resolution is also limited by the pixel pitch, which is the distance between the centre of two adjacent pixels, and varies depending on the manufacturer. Typical values are 100 µm in CsI detectors and 65-75 µm in a-Se detectors. The pixel pitch also determines the TFT matrix readout time. For this reason, as it will be further explained in the coming chapters, pixel binning is usually applied in DBT acquisitions, in which adjacent pixels are combined by summing or averaging their responses [30].

All things considered, the transition to FFDM and the introduction of flat panel detectors have advanced x-ray imaging of the breast by offering a wider dynamic range and rapid read-out times. Moreover, digitisation has given access to the realms of image post-processing, through which image quality can be improved, hence reducing the need for retakes. More relevant to this thesis is the fact that, when flat panel detectors first became available, their advantageous properties sparked a research and clinical interest in tomosynthesis, and this marked the beginning of the development and ongoing refinement of DBT [36].

1.4 Dosimetric quantities

In response to the growing concerns regarding the effects of ionising radiation, the International Commission on Radiation Units and Measurements (ICRU) and the International Commission on Radiological Protection (ICRP) were established at the second International Congress of Radiology (ICR) in Stockholm, Sweden in 1928. Since then,

ICRU and ICRP have developed special dosimetric quantities for the evaluation of ionising radiation exposures, which are based on measurements of the energy imparted to organs and tissues of the human body [14], [35].

One of the first dosimetric quantities to be introduced is the exposure X, that is used to describe the ability of EM radiation to produce ionisation in air. It is defined as

$$X = \frac{dQ}{dm} \tag{1.14}$$

where dQ is the absolute value of the total charge of the ions, of a single sign, produced in air when all the electrons released by the photons, in the volume element of mass dm, are completely stopped in air [48]. In SI units, it is measured in Ckg^{-1}, however the röntgen unit ($1\ \mathrm{R} = 2.58 \times 10^{-4}\ \mathrm{Ckg}^{-1}$) is most commonly used.

Photons are indirectly ionising radiation meaning that their release of energy in matter is a two-step process. First of all, the incoming energy of the photons is converted into kinetic energy of the atomic electrons, by either photoelectric absorption, Compton scattering or pair production only at very high photon energies. The electrons in turn deposit their energy via ionisation and excitation processes. For this reason, like other high energy charged particles, they are referred to as directly ionising radiation. *Kerma* (K) stands for kinetic energy released in matter and quantifies the kinetic energy imparted to charged particles by indirectly ionising radiation. It can be computed as

$$K = \Phi E \left(\frac{\mu_{\mathrm{tr}}}{\rho_0} \right), \tag{1.15}$$

where Φ denotes the fluence, which is the number of photons of energy E crossing a unit cross sectional area. The term $\left(\frac{\mu_{\mathrm{tr}}}{\rho_0}\right)$ is the mass energy transfer attenuation coefficient, calculated by multiplying the mass attenuation coefficient (μ/ρ_0) by the fraction of the incident photon energy that is transferred to charged particles as kinetic energy. Since in SI units Φ is measured in m^{-2} and the mass energy transfer coefficient in $\mathrm{m}^2\mathrm{kg}^{-1}$, the unit of K is J/kg which is known as gray, and is denoted by Gy ($1\ \mathrm{Gy} = 1\ \mathrm{J/kg}$).

The absorbed dose D is defined for all types of ionising radiation and is given by

$$D = \frac{d\bar{\epsilon}}{dm} \tag{1.16}$$

where $d\bar{\epsilon}$ is the mean energy delivered by ionising radiation to a volume element of mass dm. Equation 1.16 shows that the SI unit of D is also Gy. Historically D was measured as radiation absorbed dose (rad) and 1 Gy = 100 rad. Similarly to equation 1.15, D can be computed as:

$$D = \Phi E \left(\frac{\mu_{\mathrm{en}}}{\rho_0} \right), \tag{1.17}$$

where $\left(\frac{\mu_{\text{en}}}{\rho_0}\right)$ is now the mass energy absorption coefficient. It is equal to the mass energy transfer coefficient if all the incident photon energy is absorbed locally in matter, that is, if the probability of Bremsstrahlung is low. This is true for low photon energies (roughly below 200 keV) and low Z materials, and is therefore applicable to diagnostic radiology. In this case D and K are also equal.

The absorbed dose D in equation 1.16 is defined at any point in matter. In order to define radiation protection quantities, the absorbed dose needs to be averaged and then summed over the different organs and tissues of the human body. However, D is not appropriate to specify limiting dose values and thresholds, since radiation effects also depend on the type of radiation, on the time and spacial distribution of energy absorption within the human body, and on the radio-sensitivity of the exposed tissues or organs [14]. For this reason, the ICRP first introduced the quantity effective dose equivalent:

$$H_{\text{T}} = \sum_R w_R \cdot D_{T,R} \tag{1.18}$$

where $D_{T,R}$ is the absorbed dose averaged over the volume of a tissue T, due to radiation of type R with weighting factor w_{R}, and the sum is performed over all radiation types involved in the interaction. In SI units, H_{T} is measured in sievert (Sv) and 1 Sv = J/Kg. The values of w_R are determined experimentally and are related to the relative biological effectiveness, *RBE*, which quantifies the biological damage caused by a given type of radiation, with respect to the effects produced by x-rays and γ-rays. As a matter of fact, the *RBE* depends on the *Linear Energy Transfer*, *LET*, which describes the ionisation density of radiation. More specifically, the *LET* is the energy transferred per unit distance in matter, in proximity of the radiation track:

$$LET = \frac{dE}{dx}. \tag{1.19}$$

High *LET* radiation, like heavy charged particles (e.g., protons and α-particles) and neutrons, produces dense ionisation tracks, therefore causing more biological damage than low *LET*, comprising photons and light charged particles such as electrons [17]. The table 1.1 lists the weighting factors w_{R} for some types of radiation. As it can be seen, radiation of higher *LET* is characterised by a higher w_{R}, meaning that, for a given absorbed dose expressed in Gy, the biological damage created is greater.

The concept of dose equivalent was further advanced with the introduction of the effective dose E, also measured in Sv, which takes into account the differences in radiation sensitivities of organs and tissues as well [14]:

$$\begin{aligned} E &= \sum_T w_T \sum_R w_R \cdot D_{T,R} \\ &= \sum_T w_T \cdot H_T. \end{aligned} \tag{1.20}$$

Radiation	LET (keV/µm)	w_{R}
X-rays, γ-rays, e^-	2	1
Protons	20	5-10
Neutrons	4-20	5-20
α-particles	40	20

Table 1.1: Weighting factors w_{R} for radiation types of different LET. The LET and w_{R} of neutrons are a continuous function of their energy, hence a range of values is provided.

The sum in equation 1.20 is now computed over all irradiated tissue types T, which are distinguished by their respective weighting factor w_{T}. Moreover, $\sum w_T = 1$. The value w_{T} indicates the contribution of each tissue to the total detriment, that is an estimate of the risk of reduction in length and quality of life following exposure. In general, tissues with a higher reproduction activity are less resistant to radiation and are referred to as early responders. On the other hand, tissues with a lower proliferative rate are more radio-resistant and are called late responders. For instance, w_{T} of the breast, red bone marrow, colon, lung and stomach is 0.12, whereas w_{T} of the brain, bone surface, salivary glands and the skin is 0.01.

1.4.1 Radiation protection

Energy absorption in biological tissues leads to the ionisation of the atoms making up macromolecules. At high doses, tissue functionality may be compromised as a result of cell killing. This type of damage is referred to as tissue reactions or deterministic effects, since an identical dose will lead to predictable effects. For small doses, the probability of deterministic damage is zero whereas above a certain threshold (500 mSv), immediate somatic damage is observed, and its severity increases with the dose. Examples of deterministic somatic damage are skin erythema, fibrosis, hematopoietic damage and, in the case of global irradiation of the body with acute doses, the Acute Radiation Syndrome (ARS) [48].

At lower doses, the irradiated cells may survive, whilst bearing changes to the genetic material, i.e., the DNA in the cell nucleus. This can cause an increase in the risk of radiation-induced cancer, which could occur after a latency period, or hereditary disease in future generations. This type of damage is probabilistic in nature and is therefore termed stochastic. The probability of its effects, following exposure to radiation, increases with dose, with no threshold, whereas its severity is independent of dose.

The ICRP Publication 60 "1990 Recommendations of the International Commission on Radiological Protection" has formed the basis of radiation protection, which is concerned with controlling exposure to ionising radiation, in order to prevent deterministic

damage, and limit to acceptable levels the risk of long-term stochastic effects [14]. The objective of radiological protection in the low dose range is protection against stochastic effects, which are the principal health risks affecting, for instance, patients and staff during diagnostic imaging procedures [14]. Given the linear no threshold (LNT) dose response characterising stochastic effects, no exposure to radiation can be considered safe. For this reason, radiation protection programs are based on three principles:

- Justification of the practice;
- Optimisation of protection;
- Limitation of individual doses.

The ICRP defines practices as human activities that involve radiation exposure. According to the first principle, as well as being justified, the implementation of such practices should be re-considered periodically. With regards to the optimisation of protection, the goal of radiation protection programs is to keep the dose as low as reasonably achievable. This statement is known as the ALARA principle of radiation protection. For instance, the optimisation of dose is key to quality control in screening mammography, where acceptable image quality for the detection of lesions and the ALARA principle must be balanced. Finally, the overall dose received by individuals should not exceed the established limits. The effective dose limit established by the ICRP varies between exposed workers and the public. Exposed workers are people who perform activities which entail exposure to radiation doses higher than those received by the public. The third principle prescribed that the effective dose of such exposure should not exceed 20 mSv per year. On the other hand, doses to members of the public should be kept within 1 mSv per year [48].

1.4.2 Dose in mammography

Given the risk of stochastic effects associated with the use of ionising radiation and the radio-sensitivity of the breast ($w_{\mathrm{T}} = 0.12$), the estimation and optimisation of breast dose is an essential part of quality control in mammography.

Because of the low energy x-rays used in mammography, the dose in the breast decreases rapidly as a function of depth. Moreover, since the glandular tissues found in the breast ducts and lobules are the most sensitive to radiation-induced carginogenesis, the dosimetric quantity used in mammography to describe the radiation absorbed by the whole breast is the *Average Glandular Dose*, *AGD*, or *Mean Glandular Dose*, *MGD*. Given the difficulty of directly measuring the *AGD*, the latter is instead estimated by multiplying the incident air kerma at the upper surface of the breast K, also known as *Entrance Skin Kerma* (*ESAK*), without back scatter, by an appropriate conversion factor g:

$$AGD = Kg, \tag{1.21}$$

where K, expressed in mGy, is related to the dose absorbed by the breast glandular tissues through g. The g values were first calculated by using Monte Carlo simulations based on a simple model of the breast, consisting of a central region made of an equal mixture by weight of adipose and glandular tissues (50% glandularity), and an adipose surface layer 0.5 cm thick. By simulating a simple mammographic imaging system, the conversion factors were calculated for a breast thickness ranging from 2 to 8 cm, and for a variety of x-ray spectra obtained from different anode-filter combinations, e.g, Mo-Mo, W-Al and W-Rh [7].

Further simulations were carried out to account for breast thickness values outside the 2-8 cm range, for which the 50% glandularity assumption may not be appropriate, and additional x-ray spectra. New tabulated values of g were therefore obtained by varying the breast thickness in the range 2–11 cm, and the composition of the central region of the breast model between 0.1% glandularity and 100% glandularity, in steps of 25% glandularity. Equation 1.21 is thus extended to:

$$AGD = Kgcs, \tag{1.22}$$

where c corrects for any difference in breast composition from the 50% glandularity, and s accounts for the use of different x-ray spectra [12].

With the growing interest in Digital Breast Tomosynthesis, equation 1.22 has been extended to include the "tomo" factors t and T, which allow to calculate the AGD for a single projection and for a complete examination, respectively. These factors were once again determined with Monte Carlo simulations for a breast thickness in the range of 20–110 mm, different target/filter combinations and breast glandularities. Projection angles of 0° to 30° were used in two different acquisition geometries, which will be explained in more detail later on, i.e., full-field irradiation of the breast with a rotating x-ray tube, and a scanned narrow beam geometry. In the full-field geometry, the dose for a single projection at an angle θ is:

$$D(\theta) = Kgcst(\theta), \tag{1.23}$$

where $t(\theta)$ is $D(\theta)/D(0)$, that is the ratio of the Monte Carlo calculated AGD at projection angle θ and at projection angle 0° for the same tube mAs. The kerma K is also measured at 0°. For a complete tomosynthesis acquisition, the dose to the breast is:

$$D_{\mathrm{T}} = K_{\mathrm{T}}gcsT \qquad \text{with} \quad T = \sum_{i=1}^{N} \alpha_i t(\theta_i) \tag{1.24}$$

where the sum is computed over all projections N, and α is the fraction of the mAs distributed over the N projections. K_T is again measured at 0^o, but using the total mAs.

Finally, in the scanned narrow beam geometry, the AGD is defined as:

$$D_{\mathrm{S}} = K_{\mathrm{S}} gcs T_{\mathrm{S}} \tag{1.25}$$

where K_{S} is calculated for a complete scan. The factor T_{S} is:

$$T_{\mathrm{S}} = \frac{D_{\mathrm{S}}}{K_{\mathrm{S}}} \frac{K}{D_{2\mathrm{D}}} \tag{1.26}$$

where K and $D_{2\mathrm{D}}$ are the kerma and absorbed dose calculated in 2D, using the same x-ray spectrum, breast and tube loading as the tomosynthesis acquisition [6].

To sum up, it can be concluded from the above discussion that the conversion factors used to determine the AGD depend on the breast thickness and composition, and on the x-ray beam quality, which is in turn determined by the kVp, the mAs and the target/filter combination. Intuitively, since the HVL describes the penetrability of an x-ray beam, the conversion factors g and c for each breast thickness and glandularity, are usually provided as a function of HVL. On the other hand, s is tabulated for the various tube target/filter combinations, whereas t and T are given for the different projection angles and angular range respectively.

1.5 Digital Breast Tomosynthesis: the working principle

So far, key aspects concerning x-ray imaging of the breast have been outlined, focusing on the physical processes leading up to the formation of a 2D projection image. The technological solutions to meet the imaging requirements in mammography were also discussed, as well as the importance of keeping dose levels as low as reasonably achievable. This part will now cover a detailed description of the imaging mechanism in Digital Breast Tomosynthesis (DBT), touching on the hardware components of a typical DBT system, the different acquisition geometries, and image reconstruction from projection data.

1.5.1 Hardware components and acquisition geometries

With regards to its hardware components, a DBT system features the same units found in standard FFDM systems, which have however been adapted to the new technology (e.g. different x-ray spectrum filtration, detector readout time and pixel binning, [53]). Figure 1.22 illustrates the components of typical DBT systems. A direct or indirect full field digital detector is contained in a detector housing or bucky which also serves as the breast support table. A removable compression paddle is placed between the breast and the detector and an x-ray tube performs an arc motion around a point, whose position depends on the specific acquisition geometry. Currently there are two types of DBT geometries available or under development. These are shown in figure 1.23 and are:

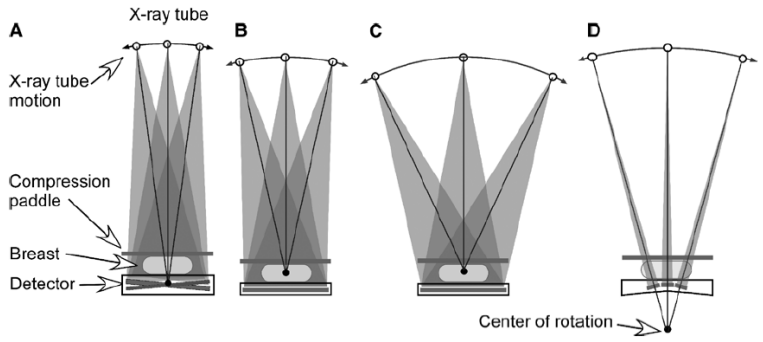

Figure 1.22: Schematic illustration of DBT systems of varying set ups (A,B,C and D), showing their main components, e.g., the detector, compression paddle and x-ray tube. The centre of rotation of the x-ray tube is also represented. Source: [30].

- Full field geometry, in which a series of individual projection images is acquired, with the whole breast being irradiated in each exposure. The x-ray tube moves over a range of angles while the detector and the compressed breast are still;
- Scanning geometry, which is based on a scanning slit photon counting detector. The breast is therefore partially irradiated by a collimated beam as the x-ray tube and the image receptor rotate. The centre of rotation is below the detector.

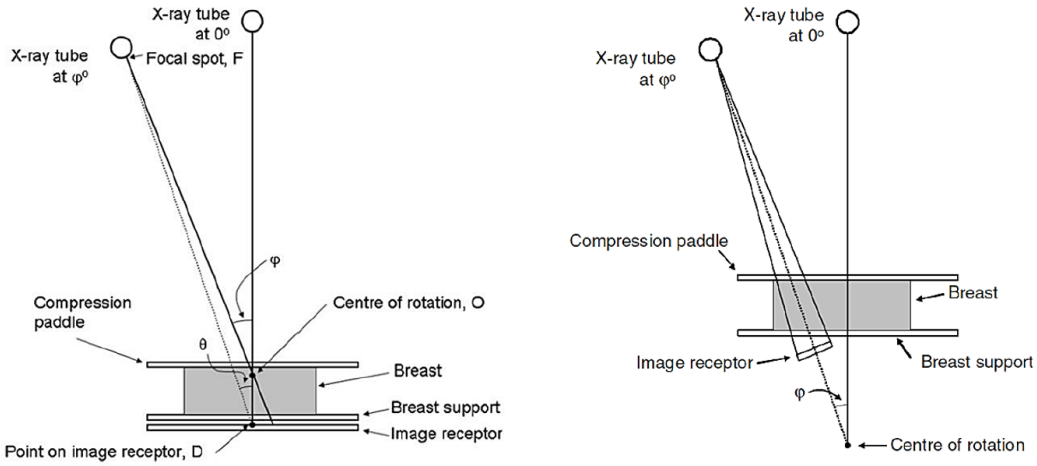

Figure 1.23: In systems based on a full field geometry (left) the centre of rotation is above a full field digital detector. Conversely, in the scanning geometry (right) the centre of rotation is below a scanning slit detector. Source: [6].

The angles φ and θ shown in figure 1.23 are the tube rotation angle and the projection angle for the rotated position respectively. Most commercially available systems are

based on the full field geometry, however the acquisition geometry may still differ in terms of x-ray tube motion. Indeed there a three kinds of design:

- Continuous, in which the x-ray tube moves with constant velocity throughout the scan [57];
- Step-and-shoot, designed so that the x-ray tube stops at each angular position, to take an exposure [57];
- Continuous sync and shoot, recently developed for the Planmed Clarity 3D system. Along with a continuous x-ray tube motion, the detector and the breast are tilted, and follow the rotation of the x-ray tube. This way the detector and focal spot stay aligned [21].

In the continuous and step-and-shoot designs, the detector may also be tilted with respect to the centre of rotation of the x-ray tube, hence perform an isocentric motion during exposures, or stay stationary, as it can be seen in set ups A and B in figure 1.22.

Undoubtedly, the type of tube motion plays a role in determining the image quality of DBT acquisitions. For instance, the step-and-shoot design is advantageous in terms of spatial resolution since focal spot blurring due to the tube motion is reduced. However, residual mechanical shaking from stopping the tube may still introduce some degree of blur [57]. On the other hand, a continuous type of motion, whilst being more affected by blurring, would entail shorter scan times, which in turn results in less dose to the patient.

1.5.2 The tomosynthesis imaging mechanism

In a complete tomosynthesis acquisition several exposures of the stationary compressed breast are performed as the x-ray tube travels over an arc. The angular range covered by the x-ray tube is known as the scan angle and varies depending on the manufacturer. Typically, the tube spans 10° to 20° and 10-20 exposures are made approximately every 1°, resulting in a total scan time of about 5 seconds or less. At each angular step, only a fraction of the radiation dose is delivered to the breast, by distributing the mAs over the single 2D projections, each acquired with a short exposure. This ensures that the dose levels in digital breast tomosynthesis are comparable to those outputted in conventional mammography [30].

The next step in the tomosynthesis imaging chain is image reconstruction. Contrary to what happens in projections obtained at 0°, in the off-axis acquisitions objects at different heights in the breast appear shifted with respect to each other, due to parallax. Through a dedicated reconstruction algorithm, the visibility of objects at a selected hight can be enhanced by appropriately shifting and summing the single projections, so that the structures in that plane are all lined up and thus in focus. Structures at other heights

are distributed over the image and appear blurred. By varying the amount of shifting, planes at different depths within the breast can be brought into focus. This algorithm is known as shift-and-add, and allows retrospective reconstruction of an arbitrary number of planes from a single acquisition sequence.

The resulting reconstructed object is a stack of tomographic planes or "slices", each reproducing the content of the breast at a different depth. The number of reconstructed slices depends on the thickness of the compressed breast and on the sampling interval, which determines the separation between slices and is typically around 1 mm [56].

Image reconstruction

The mathematical tools which form the basis for tomography were developed by Radon in a paper published in 1917, in which the Radon transform is defined. The Radon transform mathematically describes the acquisition process by which an image, defined by an unknown function $f(x, y)$, is mapped onto the projection domain (θ, t). That is, the Radon transform of $f(x, y)$ provides the projection data $P(\theta, t)$ at a distance t from a reference point and acquired at an angle θ. Image reconstruction then consists in applying the inverse Radon function to the projection data $P(\theta, t)$ in order to obtain the image $f(x, y)$.

The inverse Radon transform is most commonly calculated through Filtered Back Projection (FBP), an analytical algorithm consisting in back-projecting the projection data onto the object plane. More specifically, in the parallel rays geometry shown on

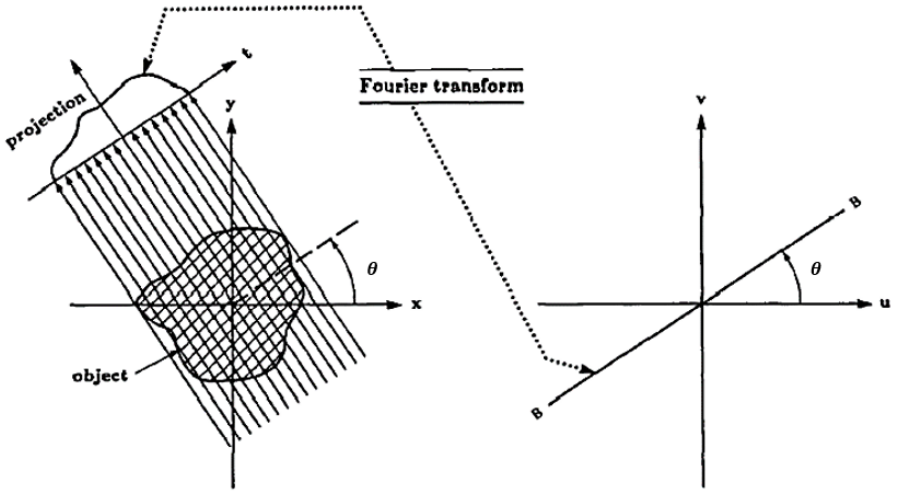

Figure 1.24: Schematic representation of the parallel rays geometry. On the left, projection data at the angle θ is obtained by integrating the attenuation coefficients along the ray paths. The projection data is mapped onto the spatial frequency domain (u, v) shown on the right. Source: [38].

the left of figure 1.24, the detected pixel value at a point in a projection of orientation θ is the line integral of the attenuation coefficients along the ray path crossing that projection point. A back-projected image of an object can thus be obtained by taking the line integral detected at each pixel in the projection, for all possible angles, and redistributing the data along the ray lines.

Based on this concept, the FBP algorithm proceeds as follows. Given the Radon transform data acquired at a direction θ, the *Fourier Transform* (FT) is first applied to sample the projection data in the spatial frequency domain (u, v), as it is shown on the right of figure 1.24. The Fourier Slice Theorem states that, in the parallel rays geometry, the FT of such projection data $F(u, v)$ gives a slice in the spatial frequency domain, subtending an angle θ with the u axis. This is indicated by the line BB in figure 1.24. As further projections are acquired at different angles, the Fourier space image is progressively sampled.

Basic shift-and-add tomosynthesis is equivalent to simple unfiltered back-projection. However, as the name suggests, FBP entails the use of filtering, that is the application of "masks" which selectively remove frequencies from the frequency spectrum. In the Fourier domain, low frequencies correspond to large features, whereas high frequencies represent small details. Now, projection data of greater value result from a longer integration path across the object being imaged. For this reason, larger features will produce a greater signal and, as a result, low frequencies are amplified, introducing blurring in the image. Taking this into account, a ramp filter is usually applied which filters out low frequencies. In the presence of statistical noise however, a band pass filter is the preferred choice since it mitigates the high frequency components of noise. In general, the choice of filter significantly affects the quality of the reconstruction. Finally, the Inverse Fourier Transform is applied to map the data back to the spatial domain and back-projection is performed.

Image reconstruction in DBT is usually performed with FBP, nevertheless some systems employ iterative or discrete reconstruction algorithms in which the object to be imaged is approximated as a finite set of n discrete planes. A projection element p_i is then obtained from:

$$p_i = \sum_j w_{ij} f_j \tag{1.27}$$

where f_j is the image or pixel element, and w_{ij} is a weighting factor describing the contribution of f_j to the projection formation. The sum is performed over the number of pixels N whereas the index i denotes the number of rays M. Reconstruction is then achieved by estimating f iteratively. More specifically, given a starting image, a pseudo projection p_i is generated from it. The pseudo projection is then compared with the detected projection data by computing a metric, and the image f is updated accordingly. This procedure is repeated for a number of steps. Examples of iterative reconstruction algorithms are the Algebraic Reconstruction Technique (ART), Simultaneous Iterative

Reconstruction Technique (SIRT) and Matrix Inversion Tomosynthesis (MTS).

As a deterministic algorithm, FPB is faster than iterative methods but fails to discriminate against noise components which will therefore also be back-projected. In iterative reconstruction algorithms on the other hand, it is possible to account for physical events responsible for noise, e.g., scattering interactions, by including their effect in the weighting factors w_{ij} [36], [38], [54].

Chapter 2

Quality Control in Digital Breast Tomosynthesis

In the previous chapter, the imaging mechanism and the different acquisition geometries of a Digital Breast Tomosynthesis system were outlined, highlighting the variability in design parameters across manufacturers. Now, the choice of the design parameters is driven by the optimisation of system performance, which is strictly connected to the detection goals and the system's clinical applications.

In their papers published in the 1990's, Fryback and Thornbury defined a scale of efficacy of an imaging system, consisting of different stages. Stage one is denoted as "technical capacity", and, as the name suggests, entails the assessment of the technical parameters at the component or system level. This is done as part of Quality Control (QC) activities, by computing figure of merits that provide objective measurements of system performance [16].

Such QC procedures involve the use of test objects or phantoms containing details that are relevant to the imaging task, to determine a metric of overall imaging performance. The material making up the phantom is designed to simulate the absorption properties of breasts of different glandularity, which is defined as the percentage by mass of glandular tissue in the breast, excluding the skin layer. For instance, a breast of 50/50 glandularity is constituted by an equal amount of glandular and adipose tissues.

Breasts of varying size are often simulated with the use of polymethyl methacrylate (PMMA) layers. PMMA is an affordable and easily obtainable absorber whose x-ray attenuation properties make it a reasonable breast model. In fact, the mass attenuation coefficient of PMMA in the energy range used in mammography (20-40 keV) varies from 5.7×10^{-1} cm^2/g to 2.4×10^{-1} cm^2/g, and is of the same order of magnitude as the mass attenuation coefficient of breast tissues (from 7×10^{-1} cm^2/g to 2.5×10^{-1} cm^2/g) [50].

In this context, EUREF's European guidelines for quality assurance in breast cancer screening and diagnosis, and the more recent DBT QC protocol provide a set of requirements and criteria that need to be met in the technical performance evaluation of FFDM

and DBT systems, taking into account the detection goals.

This part of the thesis will therefore focus on the assessment of the technical performance of DBT systems and the resulting image quality, as part of QC activities. To this end, the EUREF DBT protocol will be presented, to then move on to the quantitative metrics the tests are based on, which will be described in detail.

2.1 The EUREF protocol

The European Guidelines for quality assurance in breast cancer screening and diagnosis produced by EUREF came about in response to the need to align the quality and standards of screening programmes taking place across all EU Member States, with the objective to improve care of breast disease, and ultimately reduce cancer death rates.

In the guidelines, QC procedures are distinguished between acceptance and constancy testing, and type testing. The latter consists in assessing whether digital imaging systems of a given type or brand meet the acceptability criteria of the European protocol. A successful type test establishes that a given type of system is, in principle, capable of fulfilling the requirements of the protocol. For this reason, the clinical use of individual systems of the same type is still conditioned on the acceptance test. Then, the stability of the system is assessed through constancy testing, in which tests are performed over a specified time interval, to ensure the system continues to meet the established criteria, or to detect changes in performance.

The physico-technical procedures described in the fourth edition of the European Guidelines have been written for acceptance and constancy testing. Type testing on the other hand, is described in the EUREF type testing protocol and consists of three phases. In the first phase the system specifications and a set of clinical images provided by the manufacturer are evaluated. Next, the system undergoes two rounds of physico-technical evaluations, as described in the European guidelines, with additional measurements depending on the outcome of phase one. Finally, the performance of the system is evaluated in a clinical setting for a period of at least three months [31].

With the growing number of DBT installations and their introduction in screening programmes, in 2015 EUREF published a preliminary protocol for the Quality Control of the Physical and Technical Aspects of Digital Breast Tomosynthesis. Since then, the protocol has been continuously updated and a third version is currently available, which was first published in 2018. Since most current DBT systems are based on existing FFDM systems, the tests described in the protocol have been adapted from the current version of European Guidelines, but are still under development.

As a matter of fact, full coverage of all aspects concerning DBT performance testing is still to be achieved, and some QC tests are not in their final version. Moreover, since the image quality requirements of DBT systems are still a subject of research, limiting values are missing in some tests, and will become available once the clinical role of DBT

is clearly defined. For the time being, reference values from FFDM are considered, or baseline values need to be calculated for stability testing.

The protocol is organised in seven chapters, each dedicated to the performance of a specific system component. Namely, x-ray generation, the automatic exposure control (AEC) system, compression, the image receptor, image quality of the reconstructed image, dosimetry and image presentation. In this thesis, QC procedures assessing the AEC-system, the image receptor and the image quality of the reconstructed image were considered. For this reason, in the following sections, a detailed description of the metrics used for the evaluation of such components will be provided, whereas a thorough explanation of the full procedures and their implementation can be found in Chapter 3.

2.2 Image quality parameters

2.2.1 Detector contrast

The contrast defined in equation 1.10 is known as subject contrast, and describes the difference in signal intensity N_1 and N_2 between two regions. Through equation 1.10 it was also shown how subject contrast depends on the linear attenuation coefficient μ and the thickness of the object being imaged.

The contrast recorded in an image however, is determined by the response curve characterising a detector. The response function of a detector relates the signal recorded by the detector elements, *grey level* or *pixel value* (PV), to the dose at the detector surface. For instance, if the response is non-linear, the recorded contrast will depend on the level of exposure, even though the subject contrast is the same. More specifically, exposure intervals corresponding to regions of the curve of a greater slope would produce higher contrast.

Usually the response of a digital detector is linear, or can be linearised, and shift-invariant, meaning that the output signal remains unchanged throughout the detector area, given the same input signal. This type of system is referred to as Linear Shift-Invariant (LSI) and LSI system theory can be applied to fully characterise the performance of a detector. According to LSI system theory, the response of a detector to an input signal is given by the convolution of the signal produced by a test object $f(x, y)$ with the transfer function. Depending on the type of stimulus that is provided to the image receptor, the transfer function considered is either the *Point Spread Function* (PSF), *Line Spread Function* (LSF) and *Edge Spread Function* (ESF).

2.2.2 Spatial Resolution

As the name suggests, the *Point Spread Function* is the image produced by a point source. For this reason, by inspecting the PSF, it is possible to gain an insight into the

amount of blurring affecting the detector, which is reflected by the spreading or width of the curve. Naturally, blurring is detrimental to the spatial resolution, which, as it was mentioned in Chapter 1, defines the minimum distance at which two adjacent small objects are discernible.

In linear shift-invariant system theory, the spatial resolution is measured through the *Modulation Transfer Function* (*MTF*), which indicates the fraction of contrast per spatial frequency that is transferred to the output signal, i.e., the final image. The *MTF* is dimensionless and normalised so that its values lie in the range $[0, 1]$, where 1 corresponds to 100% transmittance of contrast, hence optimal spatial resolution. The spatial frequency is expressed in terms of line-pairs per millimetre (lp/mm), which refers to a bar pattern usually used to measure the spatial resolution. The bar pattern consists of groups of equally spaced lines, with each line pair comprising a dark line and an adjacent bright line.

Mathematically, the *MTF* is computed by taking the Fourier Transform (FT) of the normalised *LSF* [17]. That is:

$$MTF(f) = \left| \int_{-\infty}^{\infty} LSF(x) e^{-2\pi i f x} dx \right|, \tag{2.1}$$

where f denotes the spatial frequency. Since high frequencies correspond to small details and low frequencies to large distances, a typical *MTF* curve decreases as a function of spatial frequencies. That is, the contrast between finer details is reduced. An image characterised by low *MTF* appears to be blurry and of lower quality. However, since noise is associated to high frequencies in the spatial frequency domain, an image of low *MTF* is less affected by the noise components, which are filtered out. For this reason, for a more complete assessment of image quality, other metrics which also take into account noise need to be considered.

2.2.3 Noise

The physical process underlying image formation is subjected to the statistical fluctuations in the number of detected photons, which follow the Poisson distribution. This results in random variations in the grey levels recorded in the digital image, representing noise.

One metric used to quantify the amount of noise present in an image is the *Signal-to-Noise Ratio* (*SNR*), which is simply the ratio between the desired image signal and the noise component. In the context of Poisson statistics, the useful signal is given by the number of incoming photons N, while the statistical noise is the standard deviation of the distribution $\sigma = \sqrt{N}$. Putting everything together:

$$SNR = \frac{N}{\sigma} = \frac{N}{\sqrt{N}} = \sqrt{N}. \tag{2.2}$$

Equation 2.2 indicates that by increasing the statistics, i.e. the number of photons, the *SNR* is also increased.

Since detectors are characterised by a *Quantum Detection Efficiency* (*QDE*) which reaches unity only in an ideal case, the photons that are actually detected should only be considered in the *SNR*. For this reason, equation 2.2 becomes

$$SNR_{\text{real}} = \sqrt{N_{\text{detected}}} = \sqrt{QDE \times N_{\text{incident}}} \tag{2.3}$$

which is clearly less than the theoretical *SNR* defined in equation 2.2.

From a practical point of view, the *SNR* can be measured by computing the *Signal Difference-to-Noise Ration* (*SDNR*) instead. The *SDNR* is related to the human capability of detecting "large" objects with a given contrast in a noisy background. First formulated by Albert Rose, it is defined as

$$SDNR = \frac{PV_{\text{sig}} - PV_{\text{bkg}}}{SD_{\text{bkg}}} \tag{2.4}$$

where PV stands for pixel value, and SD is the associated standard deviation due to statistical noise. Hence, PV_{sig} denotes the signal produced by a uniform detail of interest, PV_{bkg} is the signal detected the background, and SD_{bkg} quantifies the amount of noise in the background. The *SDNR* is also known as *Contrast-to-Noise Ratio* (*CNR*). As a matter of fact, Rose's criterion sets a lower bound on the *CNR* perceivable by the human eye, namely $CNR \geqslant 5$ [34].

2.3 Technical evaluation of system components in DBT

The tests described in the EUREF DBT QC protocol are intended to be performed using tomosynthesis reconstructed images, so that the reconstruction algorithm is also included in the assessment. However, this approach poses some challenges in tests based on the application of linear system theory. The reason for this is the lack of a clear understanding of the relationship between the pixel values in the reconstructed DBT focal planes and the x-ray attenuation. On top of that, the shift-invariance assumption in DBT is still under investigation, since the reconstruction algorithm could produce region specific *SDNR* and spatial resolution values [59].

For this reason, some QC tests are performed on projection images, which are planar images acquired at a specific tube rotation angle [59]. This is the case for the tests assessing the Automatic Exposure Control (AEC) system and the image receptor. Tomosynthesis reconstructed images are instead used for the assessment of the total system sharpness.

2.3.1 The Automatic Exposure Control (AEC) system

The automatic exposure control (AEC) system is designed to select all the parameters that define the beam quality, namely the target-filter combination, kVp and mAs, according to the absorption properties of the breast. Since x-ray attenuation is mainly determined by the compressed thickness of the breast, most AEC systems select the filter and kVp values according to the height of the compression paddle. The selection of the exposure factors, on the other hand, is based on the assessment of the breast density. The latter is accomplished through a pre-exposure, during which an area of the detector, the AEC sensor area, serves as an exposure meter [18], [34]. This way, the resulting beam quality will deliver an appropriate dose level, whilst keeping the image quality sufficiently high for diagnostic purposes. The operator typically has three options for the AEC mode:

- A fully automatic AEC mode;
- Automatic kVp, with user-selected target and filter values;
- Automatic time of exposure using manually set target, filter, and kVp values [17].

.

The AEC system performance assessment

Since image quality is degraded by the presence of noise, the AEC should adjust the dose level to keep the noise component unchanged. For this reason, the control variable used to assess image quality and the AEC compensation capability is the *SDNR*, which is a good indicator of detectability.

Moreover, given the goal of the AEC to optimise dose and image quality, another quantity to take into account in this evaluation is the AGD for tomosynthesis, as defined in equation 1.24.

2.3.2 Image receptor

In principal, an ideal detector should be noise-free and fully transmit the input signal. However, this is not the case for real detectors, whose performance is therefore assessed with LSI system theory metrics, which quantify the amount of signal actually transmitted. The amount of noise can also be evaluated by analysing the contribution of different noise components, to the total noise in an image.

Response function

The first task in the assessment of the image detector consists in confirming the compliance of the response function with the manufacturer's specifications, which is usually

linear or logarithmic. As it was mentioned earlier, the response function describes the relationship between grey levels and detected photons, and is expressed as

$$PV = m \cdot DAK + q \tag{2.5}$$

$$PV = m \cdot \ln(DAK) + q, \tag{2.6}$$

where PV is again the pixel value, and DAK (*detector air kerma*) is the dose imparted to the detector surface. The outputs of this assessment are the slope m and the ordinate axis point intercept q. Now, the slope represents the gain of the detector, and q is an offset which is added to PV to prevent negative values. For instance, this offset needs to be taken into account when computing the *SNR*.

Should the measured image data diverge from equation 2.5, linearisation is required, and is performed using m and q.

Noise Analysis

Noise in images is measured in terms of variance in pixel values, which may result into a decreased visibility of small lesions, such as microcalcification, or low contrast objects, leading to poor image quality. In addition to the statistical nature of the interaction between the incident x-ray photons and the detector, noise can also arise from structured and electronic variations in the detector response.

The method proposed in the protocol takes into account all three main contributors to image noise:

1. Electronic noise, SD_{e};
2. Quantum noise, SD_{q};
3. Structured noise, SD_{s}.

As the name suggests, electronic noise SD_{e} is stochastic additive signal, arising from the electronic readout of the pixels, hence it is independent of dose [26]. Quantum noise SD_{q} is the known statistical noise, described by the Poisson distribution. For this reason it is proportional to $\sqrt{N}$ where N is the amount of information carriers, i.e., the x-ray photons. Finally, the structured noise SD_{s} is superimposed static signal, resulting from the spatially fixed variations in the detector response, and is therefore proportional to the detector dose. It is important to note that the above division is only applicable if the system under investigation has a linear response function. Should this be not the case, linearisation is required.

The purpose of the noise evaluation is to confirm the above trends in a given dose range, as well as the dominance of SD_{q}. In order to do this, the three different noise

components need to be determined. Being the latter uncorrelated, for a system with a linear response, the image noise can be written as

$$\begin{aligned} SD^2 &= SD_{\mathrm{e}}^2 + SD_{\mathrm{q}}^2 + SD_{\mathrm{s}}^2 \\ &= c_1^2 + c_2^2 \cdot p + c_3^2 \cdot p^2, \end{aligned} \tag{2.7}$$

where SD_{e}^2, SD_{q}^2 and SD_{s}^2 are the variances describing the individual noise sources, p is the average pixel value and c_1, c_2 and c_3 are coefficients to be determined. Given the linearity between the dose D and the pixel value, the expression in equation 2.7 can be rewritten as

$$SD^2 = k_{\mathrm{e}}^2 + k_{\mathrm{q}}^2 \cdot D + k_{\mathrm{s}}^2 \cdot D^2, \tag{2.8}$$

where k_{e}, k_{q} and k_{s} represent the different noise components.

2.3.3 Detector and system sharpness

Sharpness in an image is achieved when the fraction of contrast transferred from the original scene to the final image is enough to resolve spatial details. The *Modulation Transfer Function*, *MTF*, can therefore be used to assess the sharpness of a medical imaging system or component, without considering noise.

The *MTF* cannot be computed analytically according to equation 2.1, given the discrete nature of the *LSF*. A practical method is thus provided by Samei et al. [13], which consists in imaging a sharp attenuating edge tool. This produces an edge gradient in the image, which can be used to measure the *ESF* [17]. The *LSF* can then be determined by differentiating the *ESF*, and the *MTF* is calculated according to equation 2.1. At this stage of the assessment, projection images are used to compute the DBT system's *MTF*, whereas evaluation of the system's sharpness using tomosynthesis reconstructed images will be shown later in this chapter.

System projection *MTF*

For the case of a linear and shift invariant system, and x-rays normally incident on the detector, the total system *MTF* is the product of the *MTF* of the sub-components:

$$MTF(u,v) = MTF(u,v)_{\mathrm{geom}} MTF(u,v)_{\mathrm{conv}} MTF(u,v)_{\mathrm{aper}} \tag{2.9}$$

where $MTF(u,v)_{\mathrm{geom}}$, $MTF(u,v)_{\mathrm{conv}}$ and $MTF(u,v)_{\mathrm{aper}}$ are defined in the spatial frequency space (u,v), and are associated to the x-ray source, converter and pixel size respectively. The quantity $MTF(u,v)$ is known as the pre-sampling $MTF(u,v)$, that is the analogue $MTF(u,v)$ prior to sampling and digitisation.

Taking a step further, the $MTF(u,v)_{\mathrm{geom}}$ takes into account the finite size of the focal spot size of the x-ray tube, $MTF(u,v)_{\mathrm{fs}}$, and blurring caused by its motion, $MTF(u,v)_{\mathrm{fm}}$.

Whereas the product of $MTF(u,v)_{\text{conv}}$ and $MTF(u,v)_{\text{aper}}$ is the MTF associated to the detector $MTF(u,v)_{\text{d}}$. The pre-sampling MTF of a DBT system therefore becomes

$$MTF(u,v)_{\text{pre}} = MTF(u,v)_{\text{fs}} MTF(u,v)_{\text{fm}} MTF(u,v)_{\text{d}}. \tag{2.10}$$

Looking at equation 2.10, in order to obtain the detector pre-sampling MTF in DBT mode, the geometric blurring should be minimised, i.e., $MTF(u,v)_{\text{geom}} \approx 1$. This can be achieved by placing a radio-opaque test object on the breast support table, and considering projection images acquired at 0° so that there is no focus motion.

The reason for this can be explained by considering the acquisition geometry in x-ray imaging, which leads to magnification in the image, by the factor M:

$$M = \frac{a+b}{a} \geq 1, \tag{2.11}$$

where a is the x-ray source-to-object distance and b is the object-to-detector distance. Since the focal spot of an x-ray tube is of finite size L_{f}, its projection in the imaging plane L_{g} will also be magnified. The focal spot effective size is therefore:

$$L_{\text{g}} = L_{\text{f}} \cdot \frac{b}{a}. \tag{2.12}$$

As a result, spatial resolution is decreased. The effect of the tube travel is then added in by replacing L_{f} with the focus size due to motion g_{fm}. The latter can be calculated from the total distance travelled by the focus during the DBT scan, and the exposure time per projection image, expressed as a fraction of the total exposure time [46]. Given equation 2.12, in order to reduce blurring due to the focal spot size, the magnification factor should be reduced by placing the test object as close as possible to the detector.

Finally, to assess the system MTF, the geometrical blurring is included by acquiring images with the edge positioned at different heights above the breast support table, and a moving x-ray tube.

The design factors affecting the system MTF are the angular range, pixel binning, tube motion, and exposure time. First of all, the MTF is reduced when the x-ray tube spans a wide angle. The reason for this is illustrated in figure 2.1, where the incident x-ray is detected by more than one pixel, as a consequence of its oblique incidence on the detector sensitive area.

The MTF, could also be degraded by the application of pixel binning, which on the other hand would be beneficial to the SNR, thanks to the increase in N. The degree of the effect of pixel binning, however, also depends on the type of detector used. For instance, a-Se based detectors are able to produce high spatial resolution, despite the use of binning. With regards to the tube motion, a system based on step-shoot imaging would be less affected by blurring due the to focal spot motion, compared to a system characterised by a continuous tube motion. However, a continuous motion guarantees shorter exposure times, which can also affect the spatial resolution. In fact, long exposure times increase the risk of patient motion, leading to blurring [57].

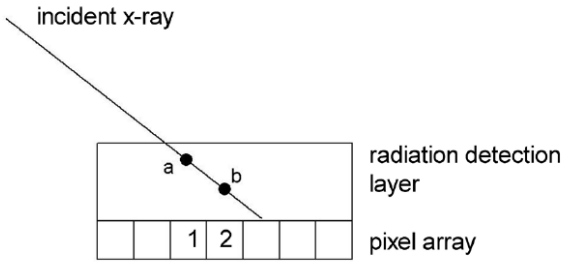

Figure 2.1: Schematic illustration of an x-ray beam entering the detector sensitive area at a wide angle. Because of the oblique incidence, the signal is recorded in two adjacent pixels. Source: [57].

2.3.4 Image quality of the reconstructed image

Total system *MTF*

Being DBT a pseudo three-dimensional imaging technique, a three-dimensional *MTF* should ideally be measured. However, the current EUREF DBT protocol suggests a method that instead outputs the *MTF* in the *x-y* plane of the reconstructed image, in the tube travel and chest wall-nipple directions. Nevertheless, the *MTF* measured in the reconstructed tomosynthesis stack provides the total system *MTF*, which also includes the effect of image reconstruction on sharpness [46].

For this measurement, the protocol suggests the use of a radio-opaque wire which allows to measure the *LSF*. Once the *LSF* is obtained, equation 2.1 can again be used to compute the pre-sampling *MTF*.

Z-resolution

The method described above provides an indication of the spatial resolution in the reconstructed *x-y* imaging plane. This test is instead concerned with the assessment of the resolution along the axis perpendicular to the reconstructed plane, usually the z axis.

An indication of the out-of-plane resolution, or z-resolution, is provided by the so called *Artefact Spread Function* (*ASF*), which measures the spread of the signal produced by a feature, between the tomographic planes. That is to say, because of the limited angular sampling characterising a tomosynthesis scan, a feature in focus within a plane generates artefacts in the adjacent planes, whose intensity decreases as the distance from the focal plane containing the object increases.

The *ASF* is defined as:

$$ASF = \frac{\overline{PV}_{\text{sig}}(z) - \overline{PV}_{\text{bkg}}(z)}{\overline{PV}_{\text{sig}}(z_0) - \overline{PV}_{\text{bkg}}(z_0)} \tag{2.13}$$

where $\overline{PV}_{\text{sig}}(z)$ and $\overline{PV}_{\text{bkg}}(z)$ are the mean pixel values quantifying the signal produced by the artefact, and an artefact-free region respectively, whereas $\overline{PV}_{\text{sig}}(z_0)$ and $\overline{PV}_{\text{bkg}}(z_0)$ are the same quantities, but calculated in the focal plane z_0. The ASF therefore describes the intensity of the artefact with respect to the signal produced by the object.

DBT systems characterised by a wider scan angle intuitively offer better resolution in the z direction, and this would be reflected by a smaller $FWHM$, computed from a Gaussian fit to the ASF data. The ASF is also affected by the reconstruction algorithm, and the type of coordinate system used in the reconstructed volume [46].

Chapter 3

Materials and Methods

In this chapter a description of CIRS DBT QC Phantom, model 021, and Sun Nuclear's Mammo 3D Performance Kits will be provided, together with the design features of the Hologic Selenia Dimensions and Fujifilm AMULET Innovality systems.

After this, following the structure in which the analysis was organised, the QC procedures in the EUREF DBT protocol considered in each part will be outlined, as well as their implementation using the ImageJ software, and scripts written in the Python programming language.

3.1 Phantoms

The choice of CIRS DBT QC Phantom, model 021, and Sun Nuclear's Mammo 3D Performance Kits was first of all dictated by their instant availability for use at Tecnologie Avanzate. That being said, the two phantoms present differences in material, imaging targets and ease of use. As a result, although both phantoms were designed to meet EUREF's requirements, their usage in the implementation of the tests inevitably differs, and some discrepancies in the test results are to be expected. For this reason, both the DBT QC Phantom and Mammo 3D Performance Kits were considered in this feasibility study.

3.1.1 CIRS DBT QC Phantom, model 021

CIRS Digital Breast Tomosynthesis QC phantom (model 021), henceforth referred to as CIRS 021 for simplicity, consists of eight semicircular homogeneous slabs made of BR50/50, which is a homogeneous 50/50 mixture of breast glandular and adipose tissue simulating material. Three of these slabs contain imaging targets and are distinguished by colour, e.g, pink, green and blue.

Figure 3.1 shows the top and front views of the three target slabs, in which the

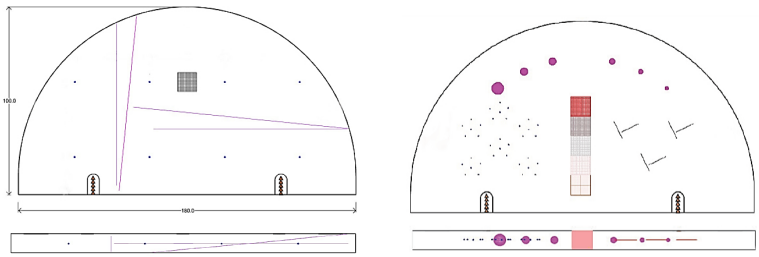

(a) Target slab 1 (blue).

(b) Target slab 2 (pink).

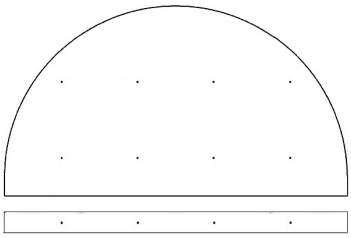

(c) Target slab 3 (green).

Figure 3.1: Top and front views of CIRS 021 target slabs. Source: [4].

different imaging targets are visible. More specifically, the target slab in 3.1a contains a pair of tungsten wires tilted horizontally, with respect to the x and y axis respectively, and another pair of tungsten wires tilted vertically in the z direction, considering a reference system in which the x-y plane corresponds to the imaging plane. A 10 x 10 mm^2 sheet of 200 µm thickness, made of pure aluminium is also present, together with a 40 mm x 40 mm array of ceramic balls, which is also included in 3.1c. Lastly, missed tissue targets made of five elements of 2 mm length are placed on the surface of the slab in the chest-wall to nipple direction. The target slab in 3.1b, on the other hand, contains features simulating breast pathologies, and are therefore used for visual detectability assessments. These are six clusters of specks, six spheroidal masses of varying dimension, together with six fibres. A step wedge made of materials of different glandularity and missed tissue targets are also included [4].

A summary of the slabs, and details of their size are provided in table 3.1. All the slabs listed in table 3.1 can be assembled with a magnetic positioning holder to simulate different breast thickness values, up to 75 mm. Figure 3.2 shows the fully assembled phantom.

The phantom at Tecnologie Avanzate has two additional homogeneous slabs which were made upon request to CIRS, in order to reach a total thickness of 65 mm, target slabs excluded. As it will be shown later, the added uniform layers are required for the implementation of several tests, and facilitate the comparison with Mammo 3D Performance Kits, which comes with 75 mm of uniform slabs.

Figure 3.2: CIRS DBT QC phantom. Also shown are the two optional swirl slabs. Source: [4].

Quantity	Size (mm)	Description
3	110 x 180 x 10	Solid homogeneous slab
1	115 x 180 x 10	Homogeneous support slab
1	110 x 180 x 5	Solid homogeneous slab
3	110 x 180 x 10	Target homogeneous slab

Table 3.1: CIRS 021 specifications [4].

The phantom used during the internship also includes two optional "swirl" slabs, made of 100% adipose and 100% glandular tissues equivalent materials, in a 50/50 ratio by weight (BRSW5050), shown in figure 3.2 too. They can be used to simulate more clinically-relevant, inhomogeneous conditions but, being this beyond the scope of this thesis, they were not used in the measurements.

3.1.2 Mammo 3D Performance Kits

As it can be seen in figure 3.3, Sun Nuclear's Mammo 3D Performance Kits significantly differs from CIRS 021 in terms of size, material and imaging targets. Designed to comply with the current version of EUREF's DBT protocol, this phantom comes in a custom hard case and consists of several PMMA plates and spacers, listed in table 3.2. Test tools for the implementation of QC measurements are also included and described in table 3.3. In addition to the tools listed in table 3.3, the phantom also comes with 100 cm of a 25 µm tungsten wire, and two 1 mm x-ray rulers.

Figure 3.3: Sun Nuclear's Mammo 3D Performance Kits. Source: [5].

Quantity	Size (mm)	Description
7	320 x 260 x 10	PMMA plate
1	320 x 260 x 5	PMMA plate
1	320 x 260 x 45	Standard test plate
7	40 x 20 x 2	PMMA plate
2	180 x 30 x 30	PMMA spacers
2	180 x 15 x 10	PMMA spacers
5	240 x 180 x 20	Foam spacers

Table 3.2: List of Mammo 3D Performance Kits PMMA plates and spacers [5].

Quantity	Size (mm)	Description
1	100 x 100 x 2	Aluminium plate
1	10 x 10 x 0.2	Aluminium foil sheet
8	100 x 100 x 0.1	Aluminium foil sheet
1	320 x 260 x 3	Stainless steel plate
1	120 x 60 x 0.6	MTF edge tool
1	320 x 260 x 5	PMMA with array of Al spheres

Table 3.3: List of Mammo 3D Performance Kits QC test tools [5].

3.2 DBT systems

The DBT systems tested are the Hologic Selenia Dimensions, which is the first DBT system to be approved by the FDA and to recently have passed EUREF's type testing, and Fujifilm AMULET Innovality. Both systems are based on the full field acquisition geometry, which ensured the implementation of measurements was identical between

systems.

However, differences in design parameters as shown in table 3.4, made it possible to observe the dependence of image quality measurements on acquisition settings, and assess whether this dependence was captured by the phantoms under evaluation. Taking this into account, one of the tasks was to assess whether the results obtained when using the phantoms, on both systems, reflected the differences in design.

System	**Selenia Dimensions**	**AMULET Innovality**
Detector type	a-Se direct	a-Se direct
Detector pixel size	70 µm	50 µm
Binned pixel size	140 µm	100/150 µm
Detector motion	Rotating (±2.1°)	Static
Source-to-detector	700 mm	650 mm
X-ray tube target	W	W
X-ray tube filter	Al, Rh, Ag, Cu	Rh, Al, Cu
X-ray tube motion	Continuous	Continuous
Angular range	± 7.5°	± 7.5° or ± 20°
Angular step	1°	1° or 2.67°
Scan time	3.7 s	4-9 s
Reconstruction alg.	FPB	Iterative

Table 3.4: Design parameters of the Hologic Selenia Dimensions and Fujifilm AMULET Innovality DBT systems [56].

3.2.1 Hologic Selenia Dimensions

Measurements from the Hologic Selenia Dimensions system were carried out at Molinette Hospital, part of the Azienda Ospedaliero-Universitaria Città della Salute e della Scienza, in Turin. Further acquisitions were made at Tecnologie Avanzate's laboratory, where another DBT system of the same model was being reconditioned and was available for use. These were used for repeatability studies, together with data acquired from another Selenia Dimensions at IRCCS Ospedale Policlinico San Martino, in Genova.

The Selenia Dimensions at Molinette Hospital is shown in figure 3.4, in which all the system components described in 1.5.1 can be seen, namely the x-ray tube arm, the compression paddle and detector housing. Referring to table 3.4, the x-ray tube contains a tungsten (W) target and four options for filtration. Rhodium (Rh) is selected in 2D mode, and replaced by silver (Ag) when the recorded breast thickness is greater than 6 cm. For the reasons explained in 1.3.1, aluminium (Al) is used in the tomosynthesis modality. Finally copper (Cu) is set in contrast-enhanced-mammography (CEM), the

latest addition to FFDM, which is based on the intravenous administration of a iodinated contrast material, and dual energy imaging techniques [19].

Figure 3.4: The Hologic Selenia Dimensions at Molinette Hospital, of the Azienda Ospedaliero-Universitaria Città della Salute e della Scienza, Turin, Italy. Two 10 mm PMMA plates of Mammo 3D Performance Kits are placed on the breast support table.

In addition to the tomosynthesis modality, denoted Tomo, the Selenia Dimensions also offers Combo-mode imaging, through which both tomosynthesis and 2D scans are acquired during the same compression. As well as reducing patient discomfort thanks to the need of one compression only, the Combo-mode produces co-registered image sets, meaning that detected features in the tomo and 2D images will have the same coordinates.

Both Tomo and Combo-mode imaging are also available in High Definition (HD) mode, which is achieved by operating in unbinned mode. Now, the Selenia Dimensions comprises a direct conversion a-Se detector, with pixels of size 70 µm. By applying 2 x 2 pixel binning, the effective size of the detector elements becomes 140 µm. This results in a faster readout time and a reduction of noise, at the expense of the intrinsic spatial resolution. Operating in the unbinned mode however, makes it possible to recover the high spatial resolution, with no increase in the 3.7 s scan time.

During a tomosynthesis acquisition the x-ray tube spans a total angular range of 15° (± 7.5°) with a continuous motion, taking exposures roughly every 1°. This results in 15 projection images which are reconstructed through a FBP algorithm into a volume

made of 1 mm planes or "slices" of varying number, depending on the compressed breast thickness, plus five additional slices. Moreover, throughout the scan, the detector slightly rotates by $\pm$ 2.1°. This type of motion is illustrated in figure 1.22, set up A, and mitigates the effect of the oblique incidence of the x-ray beam.

3.2.2 Fujifilm AMULET Innovality

The Fujifilm AMULET Innovality system used for the data acquisition is located at the European Institute of Oncology (IEO), in Milan, and shown in figure 3.5. Like the Selenia

Figure 3.5: The Fujifilm AMULET Innovality at the European Institute of Oncology (IEO).

Dimensions, this system contains a direct conversion a-Se detector, but of differing pixel size. In fact, the detector elements are 50 µm, with the possibility to obtain a size of 100 µm or 150 µm, by applying respectively 2 x 2 and 2 x 1 binning.

The Innovality offers two tomosynthesis acquisition modes, Standard (ST) and High Resolution (HR), which are characterised by a different angular range. More specifically, in the ST mode the x-ray tube covers a total angle of 15° with a step of 1°, whereas in HR imaging a wide angle of 40° is spanned, with exposures taken every 2.67°. The HR mode provides greater depth resolution, but longer scan times, roughly 9 s as opposed to about 4 s in the ST mode. A Combo-mode as seen in Hologic was not available on this system, and different compressions were required per image set. The 15 projections obtained with both modes are reconstructed through an Iterative algorithm called Iterative Superior Reconstruction (ISR), which optimises image quality [32]. The outputted volume is made

of 1 mm thick slices, with a variable number of slices added to the original compressed thickness.

With regards to the x-ray tube, the anode material and filters are the same as the ones found in the Selenia Dimensions, with the exception of silver. Considering the geometry of acquisitions, the motion of the x-ray source is also continuous, but the detector is static (see figure 1.22, set ups B and C). Finally, the source-to-detector distance is 650 mm, as opposed to the 700 mm in the Selenia Dimensions [33], [32].

3.3 Image data

The signal detected by an image receptor represents raw image data. Before becoming accessible to users, the image data undergoes some pre-processing steps. These include a flat-field correction through which variations in gain or sensitivity of detector elements are removed, and a bad pixel correction to eliminate the effect of defective detector elements. In addition to this, corrections for geometrical distortions and readout time variation are also carried out. As a result, non-uniformities either due to the radiation field or the image receptor are compensated for.

The resulting images are referred to as "unprocessed" or "for processing" and are saved in the DICOM format. DICOM stands for Digital Imaging and Communications in Medicine and is the international standard for the storage and exchange of medical imaging data. Images saved in the DICOM format also include a Header with information regarding the patient and the acquisition parameters, appropriately labelled by a DICOM tag. Processing to adjust the clinical appearance of the unprocessed images is then applied, resulting in processed or "for presentation" images.

In DBT, depending on the acquisition mode used, the following types of images are available:

- Breast Projection Object (BPO);
- Breast Tomosynthesis Object (BTO);
- Standard 2D planar images, marked as MG.

A complete tomosynthesis scan provides BPO and BTO images. A BPO dataset consists of a series of planar images acquired at each angular position of the x-ray tube. For instance, a scan acquired with a total angular range of 15° would produce 15 BPO images. BPO images are unprocessed and are the data used by the reconstruction algorithm to produce a BTO stack.

The BTO stack thus represents the reconstructed volume and consists of a set of images reproducing the content of planes at different depths in the breast. The distance between adjacent planes is known as the slice thickness.

Since most DBT systems include FFDM imaging, standard two-dimensional mammograms images (MG) are also available, of both "for processing" and for "presentation types". In addition to this, synthetic 2D views can be generated from the tomosynthesis dataset by collapsing the breast reconstructed volume onto a plane. However, the EUREF tests are not applicable to 2D synthesised images, since it cannot be assumed they contain the same information as the FFDM images [59].

3.4 Part one: comparison of phantoms for a given DBT system

For this part of the analysis, given the variability between the imaging targets included in CIRS 021 and Mammo 3D Performance Kits, only EUREF's DBT QC tests applicable to both phantoms were selected. These are:

- AEC system performance;
- Z-resolution.

The analysis was carried out on the datasets acquired with the Hologic Selenia Dimensions at Molinette Hospital and the Fujifilm AMULET Innovality at the IEO.

3.4.1 AEC system performance

The assessment of the AEC system performance consists in computing the *SDNR* on the first projection image of seven BPO series, each corresponding to a different phantom thickness, ranging from 20 mm to 70 mm. Given equation 2.4, in order to calculate the *SDNR* a phantom providing a signal difference is required.

This can be achieved by using a homogeneous background slab containing a small test object that generates a homogeneous signal, so that the mean grey value calculated in a region of interest (ROI) is representative of the entire object [17].

With Mammo 3D performance Kits, such a phantom can be assembled by using homogeneous PMMA plates, together with the 10 x 10 x 0.2 mm^3 aluminium plate. Likewise, the solid homogeneous slabs of CIRS 021 can be used, along with target slab 2, also containing an aluminium insert of size 10 x 10 x 0.2 mm^3.

Experimental set up

According to the EUREF protocol, the aluminium test object should be placed at a distance of 60 mm from the chest wall side and centred laterally, sandwiched between two 10 mm homogeneous PMMA plates. This way an initial total thickness of 20 mm is reached.

Using Mammo 3D Performance Kits, this was done by placing the aluminium foil between two 10 mm PMMA homogeneous plates. With CIRS 021 however, since the target slab containing the Al insert is 10 mm thick, only one 10 mm homogeneous slab was used, which was placed below the target slab. This way, assuming the Al insert is in the middle of the target slab, about 5 mm of homogeneous material were on top of it.

Exposures under AEC were thus acquired, adding in each measurement a layer of homogeneous plate and setting the height of the compression paddle to the values reported in table 3.5, which lists the equivalent breast thickness for each phantom thickness considered, defined in their paper by Dance et al. [12]. This was to ensure that the AEC system selected the clinically relevant exposure factors, for the simulated breast glandularity. For instance, 20 mm of PMMA would simulate a breast of thickness 21 mm and 97% glandularity, whereas 70 mm would simulate a 90 mm thick breast, of 4% glandularity. Tables 3.6 and 3.7 list the components of the phantoms used in the test.

Phantom thickness (mm)	Height of compression paddle (mm)
20	21
30	32
40	45
45	53
50	60
60	75
70	90

Table 3.5: Equivalent breast thickness for each phantom thickness [59].

Quantity	Description	Size (mm)
5	Solid homogeneous slab	110 x 180 x 10
1	Solid homogeneous slab	110 x 180 x 5
1	Target homogeneous slab 1	110 x 180 x 10

Table 3.6: Components of CIRS 021 used in the AEC system performance assessment.

On the Selenia Dimensions, the Combo imaging mode was selected so that 2D mammograms would also be obtained from the same compression. Then the AEC mode was set to "AutoFilter", meaning that the *kilovoltage peak* (kVp) would be selected according to the height of the compression paddle, and the current-time product (mAs) would be determined from a pre-exposure. The acquisition workstation also offered the option to select the AEC sensor area which would be used to determine the mAs during the

Quantity	Description	Size (mm)
6	PMMA plate	320 x 260 x 10
1	PMMA plate	320 x 260 x 5
1	Al foil sheet	10 x 10 x 0.2

Table 3.7: Components of Mammo 3D Performance Kits used in the AEC system performance assessment.

pre-exposure, denoted by "cell". The position of these cells is indicated on the compression paddle, allowing the user to directly visualise the area of the detector in which the exposure factors are determined.

Given the greater density of aluminium compared to PMMA and BR50/50, care was taken in selecting a cell which did not correspond to the position of the Al insert, since this could have resulted in a higher mAs. For this reason, a reasonable choice for the AEC sensor area was setting "2".

On the other hand, the AEC system of the AMULET Innovality system, the Intelligent AEC (iAEC), is designed to automatically detect regions of greater density, from low dose pre-shot images [32]. The option to manually select a sensor area was therefore not available on this system. Moreover, standard tomosynthesis and FFDM acquisitions were acquired separately since a Combo imaging mode was not included in the system.

Quantitative measurements: the *SDNR*

The measurements required for the calculation of the *SDNR* were performed using ImageJ, an image processing software based on the Java programming language.

First of all, in order to compute the *SDNR* according to equation 2.4, the signal produced by the aluminium test object and the background, together with the amount of noise in the background are required. These were obtained by measuring the average pixel value and standard deviation in appropriate regions of interest (ROI), drawn in the first projection image. More specifically, a 5 x 5 mm^2 ROI was placed in the centre of the image of the Al sheet, and two additional 5 x 5 mm^2 ROIs were positioned in the background, on the chest wall and nipple side, as shown in figure 3.6.

To compensate for any non-uniformity in the projection images, the ROIs in figure 3.6 were further divided into 1 x 1 mm^2 sub-ROIs. This way, the averages of the mean pixel values and standard deviations measured in the single elements in figure 3.7 could be used to compute the *SDNR* instead.

Given the small x-ray attenuation change produced by the 0.2 mm thick aluminium plate, signal linearity could be assumed even for non-linear systems [42]. Thus, the *SDNR* could be calculated by plugging in equation 2.4, the mean pixel value measured in the Al image, and the average of the measurements taken from the two background

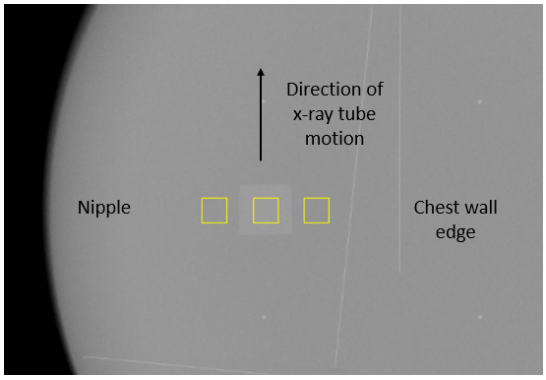

(a) CIRS 021.

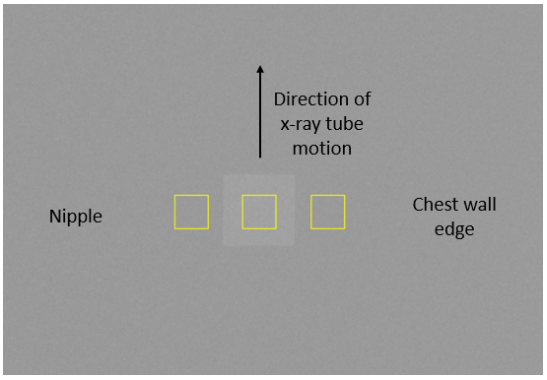

(b) Mammo 3D Performance Kits.

Figure 3.6: ROIs for the *SDNR* calculation on CIRS 021 and Mammo 3D Performance Kits.

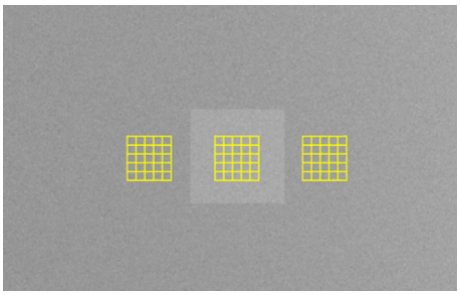

Figure 3.7: ROIs for the *SDNR* calculation further divided into 1 x 1 mm^2 sub-ROIs.

ROIs:

$$PV_{\text{bkg}} = \frac{\sum_{n=1}^{2} PV(ROI_n)}{2} \tag{3.1}$$

$$SD_{\text{bkg}} = \frac{\sum_{n=1}^{2} SD(ROI_n)}{2}. \tag{3.2}$$

The computation was performed on all seven acquisitions corresponding to the different breast thickness values, making sure the first projection image was always selected. This guaranteed that the exposure parameters were the ones determined by the AEC system, and the effect of lag and ghosting was limited.

Automation

The sampling from the ROIs shown in figure 3.6 was automated through the use of the ImageJ macro language.

When the macro is run, a reference ROI of size 5 x 5 mm^2 is first positioned 60 mm away from the chest wall edge and centred laterally, where the aluminium insert should be according to the protocol. Then, the user is asked to re-position the ROI so that it is centred in the Al plate. Next, two background ROIs are automatically positioned so that their centres are 10 mm away from the the centre of the signal ROI. Then the mean pixel value and standard deviation are measured in each ROI, and the results are saved as comma-separated values (csv) files.

The same ROIs can be used in the other projection images of the dataset, provided the signal ROI is still centred in the Al plate. Should this not be the case, the macro can be ran again to create a new set of ROIs. Finally, the results are imported into a Python script that implements the *SDNR* calculation.

Should it be necessary to subdivide the ROIs into smaller regions, a separate macro was implemented which, using the 5 x 5 mm^2 as boundaries, measures the mean pixel value and standard deviation in adjacent 1 x 1 mm^2 sub-ROIs. The data can then be imported into a Python script, through which the averages from the single elements are computed, and the *SDNR* calculation is carried out.

3.4.2 Z-resolution

The assessment of the spatial resolution in the direction perpendicular to the reconstructed planes (x-y direction) entails the use of reconstructed images containing small high contrast details.

The method described in the EUREF protocol requires an array of aluminium spheres of 1 mm diameter, positioned within 60 mm of PMMA plates, at different heights above the breast support table. This experimental set up was therefore reproduced using both types of phantoms, bearing in mind their differences in material.

Quantitative measurements consisted in computing the *Full Width at Half Maximum* (*FWHM*) of the *ASF* profile. To this end, two different methods to measure the pixel values in the relevant ROIs were implemented and compared.

Experimental set up

The z-resolution phantom of Mammo 3D Performance Kits consists of a 50 mm x 50 mm array of aluminium spheres of 1 mm diameter, embedded in 5 mm of PMMA. This was used together with six of the 10 mm homogeneous PMMA plates, for a total thickness of 65 mm.

Similarly, target slab 3 of CIRS 021 containing a 40 mm x 40 mm array of ceramic balls of 0.8 mm diameter was added to six of the BR50/50 homogeneous slabs. This way, considering the size of the target slab too, a total thickness of 70 mm was reached.

With both the Selenia Dimensions and AMULET Innovality systems, three tomosynthesis acquisitions were acquired under AEC. The height of the compression paddle de-

termined the number of slices in the reconstructed volume. In the first exposure, the slab containing the array of spheres was placed between the first and second homogeneous plates, then between the third and fourth, and lastly between the fifth and sixth. Assuming the spheres are in the middle of the slab, the set ups corresponded respectively to a height of 12.5 mm, 32.5 mm and 52.5 mm for Mammo 3D performance Kits, and 15 mm, 35 mm and 55 mm for CIRS 021. This way, it was possible to observe the variation of the z-resolution as a function of the position of the spheres on the z-axis. With the Innovality, acquisitions in both the ST and HR modes were performed, in order to notice the effect of the tomosynthesis scan angle on the depth resolution.

Further acquisitions of Mammo 3D Performance Kits with the Selenia Dimensions at Tecnologie Avanzate and San Martino Hospital in Genova were also used to compare the two quantitative methods for the *ASF* calculation.

Quantitative measurements: choice of the ROI size

Given the definition of the *ASF* in equation 2.13, two methods were implemented to measure $PV_{\text{sig}}(z)$ and $PV_{\text{bkg}}(z)$ with ImageJ, on the BTO dataset.

The first method consisted in positioning a circular ROI over the sphere and measuring the mean pixel value in all the slices making up the stack. The size of the ROI was first of all determined by considering the sphere diameters in both phantoms, and the pixel spacing in the reconstructed images.

Moreover, for this method to produce satisfactory results, the mean value measured in the ROI would have to be representative of the maximum signal produced by the sphere. For this reason, care was taken in choosing a ROI that would provide enough statistics, and at the same time guarantee the least variation in pixel values in the in-focus plane.

Three values were thus considered and compared, according to the measured standard deviation *SD*, starting from the actual sphere diameter, and decreasing it in steps of 1 pixel. The ROIs are shown in figure 3.8a. From this preliminary analysis, it was concluded that a ROI size of 7 x 7 pixels was a reasonable choice for both phantoms and DBT systems.

For the background signal, 300 x 300 pixels circular ROIs were placed on artefact free regions, halfway between each sphere, if the extent of the FOV allowed it (see figure 3.8b). Then, for each sphere, the average of the mean pixel values measured in the two adjacent background regions was considered.

In the second method, ROIs of the same size were placed on the spheres and the background regions, as shown in figure 3.9a. A size of 160 x 160 pixels was chosen, so that the full artefact spread would be contained within the ROI. This is illustrated in figure 3.9b. In this case, the *ASF* would be computed by taking as $\overline{PV}_{\text{sig}}$ the maximum pixel value in the ROI centred in the sphere.

A summary of the ROIs used in each method is provided in table 3.8. Each method was implemented on repeated acquisitions of Mammo 3D Performance Kits carried out

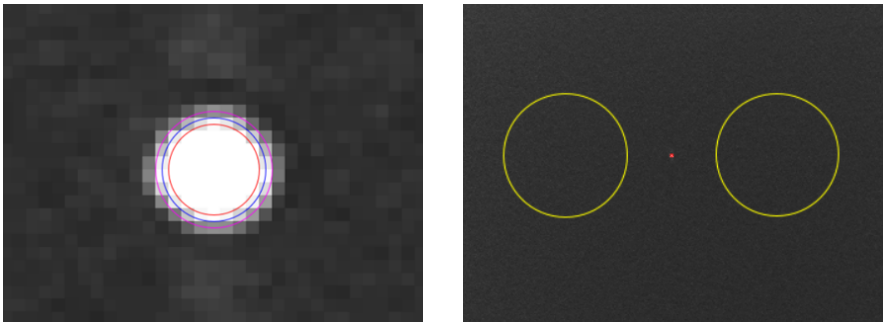

(a) (b)

Figure 3.8: Representation of the ROIs used for the *ASF* calculation, drawn on a slice of Mammo 3D Performance Kits (a) 9 x 9 pixels (magenta), 8 x 8 pixels (blue), 7 x 7 pixels (red) (b) 300 x 300 pixels ROIs placed on the artefact free regions adjacent to the sphere.

with the Selenia Dimensions systems at Molinette Hospital, at Tecnologie Avanzate's laboratory and at San Martino Hospital.

In this preliminary analysis, only acquisitions with the z-resolution phantom between the third and fourth PMMA slab were considered. Moreover, the *ASF* was only computed on one sphere, positioned approximately 11 cm away from the chest wall edge. The results were compared with the available literature and, based on this, one method only was chosen for the comparison between the phantoms.

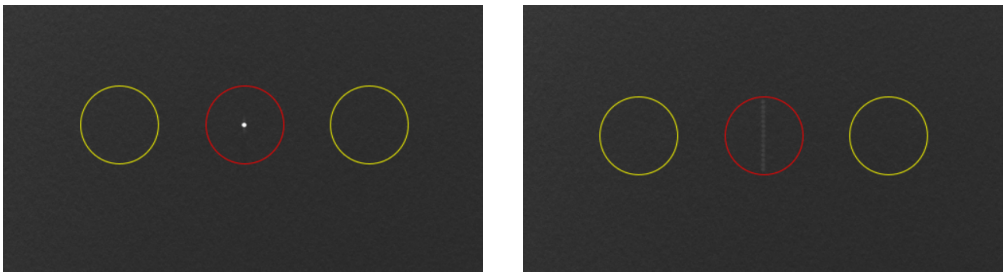

(a) (b)

Figure 3.9: Representation of the ROIs used for the *ASF* calculation, drawn on a slice of Mammo 3D Performance Kits (a) 160 x 160 pixels ROIs drawn on both the sphere (red) and the background regions (yellow) (b) Out of focus plane showing the artefact spread, fully contained within the red ROI.

	Signal	Background
Method 1	7 x 7 px	300 x 300 px
Method 2	160 x 160 px	160 x 160 px

Table 3.8: Size of the signal and background ROIs compared in the preliminary analysis.

Quantitative measurements: *ASF* calculation

Using one of the methods described above, the pixel value data was acquired from the phantoms. Since previous studies have demonstrated worse reproducibility for objects located near the edges of the detector and away from the chest wall edge side [9], with Mammo 3D Performance Kits measurements were limited to 12 spheres within the useful FOV. Whereas, all 8 spheres of CIRS 021 were considered. Moreover, just like in the AEC system performance test, system linearity can be assumed even for non-linear systems, given the small signal difference produced by the phantom spheres.

Once the pixel value data was acquired from the set of ROIs, the next step consisted in calculating the *FWHM* of the *ASF* profiles. Using the Python programming language, first of all the *ASF* formula defined in equation 2.13 was implemented and computed by plugging in the average pixel values measured in the ROIs. The focal plane z_0 was found by measuring the standard deviation in ROIs surrounding the spheres. The slice with the greatest standard deviation was hence taken to be the focal plane z_0. Then the *ASF* values were plotted as a function of slice number of the reconstructed volume, this way producing an *ASF* profile along the z-direction. Next, a Gaussian curve was fitted to the data, and the outputted standard deviation parameter was used to calculate the *FWHM* according to:

$$FWHM = 2\sqrt{\ln 2} \cdot \sigma \approx 2.355 \cdot \sigma. \tag{3.3}$$

Automation

The automation of measurements is based on the detection of the high contrast details, and the recording of the corresponding (x, y) coordinates in the image plane, according to which the required ROIs are positioned.

Despite the greater density of aluminium and ceramic, the signal produced by the spheres is greater than the background pixel values, suggesting a greater attenuation of the x-ray beam by the combined thickness of the six PMMA and BR50/50 slabs. For this reason, the spheres are located by first of all applying the ImageJ *Z-project* method which, if the maximum intensity projection type is chosen, highlights the brightest pixels within the stack.

Before proceeding to the next step, the macro prompts the user to select a ROI containing all the spheres to be included in the analysis. Then, by running the *Find*

Maxima function in small ROIs encompassing each sphere within the useful FOV, starting from the far left, a list of ordered (x, y) coordinates corresponding to the position of the spheres is obtained.

Next, pixel value data is gathered from circular ROIs, whose centre corresponds to the maxima coordinates. It should be however noted that the procedure just described, when applied in method 1, would result in ROIs not correctly centred in the sphere. As a consequence, background pixels would also be included, leading to an increased standard deviation, hence an overestimated *ASF FWHM*, i.e., worse resolution. For this reason, in implementing method 1, the signal ROIs should be positioned manually. The background ROIs are instead generated by adding to the x coordinate of the maxima points, half the size of the array of spheres, e.g., 27.5 mm for Mammo 3D Performance Kits and 20 mm for CIRS 021.

The macro is written so that the results associated to each sphere are saved in separate csv files, containing the pixel data measured in all the slices making up the stack. Measurements from each background area are also saved individually. Then, the signal and associated background pixel data can be imported one by one in a Python script, for the calculation of the *ASF*.

3.5 Part two: phantom performance in the physical characterisation of DBT systems

The objective of this part of the analysis was to further validate the usage of the phantoms in tomosynthesis QC procedures, by comparing the results obtained with the available literature regarding the physical characterisation of DBT systems. To this end, the following tests were considered:

- Response function and noise analysis of the image receptor;
- System projection *MTF* with an edge test object;
- *MTF* in the reconstructed image;
- Z-resolution with spheroidal masses of varying diameter.

3.5.1 Response function and noise analysis of the image receptor

Experimental set up

In order to determine the relationship between the grey values in an image and the number of detected photons (equation 2.5), projection images acquired within a detector dose range, starting from a nearly zero dose to a level close to saturation were required.

This was done by placing a 2 mm thick aluminium plate included with Mammo 3D Performance Kits as close as possible to the x-ray tube, as shown in figure 3.10. The additional aluminium filter ensured that the resulting x-ray beam simulated the spectrum exiting an average breast [26]. Then, in manual mode, the tube voltage that would be chosen by the AEC syste, for a thickness of 45 mm was selected. This was 31 kVp for the Selenia Dimensions and 32 kVp for the AMULET Innovality. Exposures of the

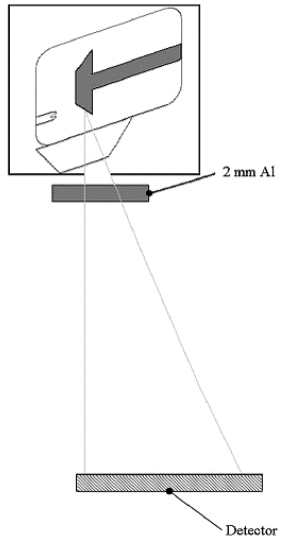

Figure 3.10: Experimental set up for the detector response function and noise components analysis. Source: [28].

aluminium plate were thus acquired starting with the minimum mAs value that could be selected, and increasing it by a factor of about 1.4 between exposures, covering the full operating current range of the x-ray tube [46]. The number of acquisitions was therefore system dependent.

Quantitative measurements

The response function can be determined by plotting the mean pixel values as a function of either the mAs, or the incident air kerma on the detector surface, also known as detector air kerma (DAK). For a given mAs, the incident air kerma can be calculated from the tube output, which is defined as:

$$Output = \frac{Dose\,[\text{mGy}]}{Exposure\,[\text{mAs}]}. \tag{3.4}$$

The tube output can be experimentally measured with a dose meter positioned within the x-ray field, 45 mm above the breast support table, and 60 mm away from the chest

wall edge. The tube output of the Hologic Selenia Dimensions at 31 kVp is 11.435 mGy/mAs. For the Fujifulm AMULET Innovality, the tube output at 32 kVp measured at the bucky (620 mm) is 0.11 mGy/mAs. Both values were available from previous measurements.

However, using equation 3.4 for the Selenia Dimensions with the available tube output data would provide the entrance dose at 45 mm. The detector entrance dose therefore needs to be derived by applying the inverse square law, according to which:

$$\frac{I_1}{I_2} = \frac{D_2^2}{D_1^2} \tag{3.5}$$

where I_1 and I_2 are the photon intensities measured at the distances D_1 and D_2 from the x-ray source respectively. Correcting the entrance dose for the inverse square law would thus give:

$$DAK = ESK \cdot \frac{(D_{\text{det}} - 45\,\text{mm})^2}{D_{\text{bucky}}^2} \tag{3.6}$$

where *ESK* is the entrance skin kerma at 45 mm, D_{det} is the system's source to detector distance, which is 700 mm on the Selenia Dimensions. The variable D_{bucky} is the source to bucky distance, which unlike D_{det}, provides the distance from the source to the detector's sensitive area, which is the quantity required for the measurement of the *DAK*. On the Selenia Dimensions, it is equal to 675 mm.

The mean pixel values and standard deviations were measured in unprocessed first projection images, in a 5 x 5 mm^2 ROI positioned 60 mm away from the chest wall edge and centred laterally, which is where the dose meter should be placed in the tube output measurement.

Once the required data was gathered, for the purpose of this thesis it was chosen to plot the mean pixel values as a function of the mAs data, to then perform a weighted linear fit. In case of a non-linear response function, the output of the fit would be used to perform linearisation of the pixel values, before proceeding with the noise analysis.

The latter consisted in determining the noise coefficients $k_{\text{e}}, k_{\text{q}}$ and k_{s} in equation 2.8 at every exposure level. In particular, given the definitions of the noise components provided in 2.3.2, k_{e} can be determined from a zero-dose or flood image, which only contains readout noise. This condition is achieved in the images acquired at the lowest dose level, thanks to the presence of the 2 mm Al filter, which prevents the low intensity x-ray beam from reaching the image receptor [28].

Thus, to find the noise components, the square of the measured *SD* was plotted as a function of the linearised pixel values, and a second order polynomial fit was performed. The resulting coefficients were then used to compute the percentage fraction of the total noise, for all noise components:

$$e = \frac{SD_{\text{e}}^2}{SD_{\text{theor}}^2} \cdot \% \qquad q = \frac{SD_{\text{q}}^2}{SD_{\text{theor}}^2} \cdot \% \qquad s = \frac{SD_{\text{s}}^2}{SD_{\text{theor}}^2} \cdot \% \tag{3.7}$$

which were then plotted as a function of the *DAK* corresponding to the current-time product used for the acquisitions.

Automation

An ImageJ macro was also written to automate measurements, and simply consists in positioning a 5 x 5 mm^2 ROI at 60 mm from the chest wall edge, and centred laterally, in the first projection image of the BPO series. Once the procedure has been repeated for the full dataset, the pixel value data are then saved in a csv file, whose number of rows is equal to the number of mAs values used for the acquisitions.

The results are then imported in a Python script which first of all asks the user to enter the number of images to be used for the analysis, and the corresponding mAs values. Then the user is also asked to provide the tube output of the system being tested, which is required to determine the entrance dose according to equation 3.4. Next, once the source-to-bucky distance of the system being tested is also given, the *DAK* values can be computed by applying the inverse square law. Alternatively, the current-time product data can be used. Finally, depending on the system, a linear or logarithmic fit is performed with the Python routine `curve_fit`, of the SciPy library, and the offset and gain values are exported in a new csv file.

3.5.2 System projection *MTF*

The objective of this test is to measure the system projection pre-sampling *MTF* defined in equation 2.10, starting from the signal produced by an edge test object. The latter is provided as part of the Mammo 3D Performance Kits and consists of two orthogonal edges, which make it possible to compute the *MTF* along two directions: parallel and orthogonal to the tube motion.

Experimental set up

Once again, a 2 mm thick aluminium plate was placed as close as possible to the x-ray tube, in order to attenuate the x-ray beam. The edge test object was then placed on top of the detector housing, at an angle of about 3°, and with its centre 60 mm away from the chest wall edge, as shown in figure 3.11. The slight tilt of the test object was required to tackle the issue of aliasing due to discrete sampling.

More specifically, the Nyquist theorem states that in the digitisation of signals, the sampling step must be less than half the size of the smallest perceivable object. Should this criterion not be met, aliasing occurs, resulting in signal loss. Consequently, it is possible to define the Nyquist frequency, representing an upper bound to the spatial frequency that can be detected:

$$F_{\mathrm{N}} = \frac{1}{2\Delta x} \tag{3.8}$$

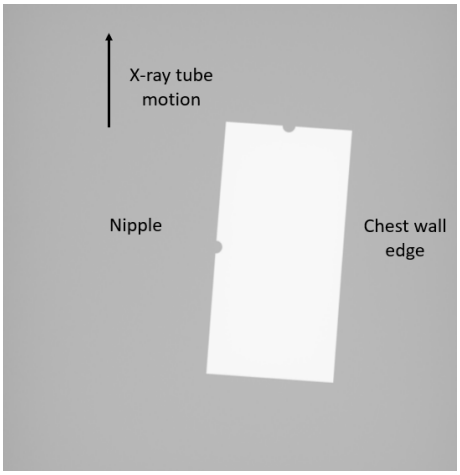

Figure 3.11: Projection image of the angulated edge test object positioned on the breast support table, with its centre 60 mm away from the chest wall edge.

where Δx is the sampling step or detector pitch.

Now, if the pre-sampling *MTF* (equation 2.10) is non-zero beyond F_{N}, aliasing occurs. However, by tilting the edge test object, multiple *ESF*s corresponding to the different alignments of the edge with respect to the sampling coordinate are obtained, in the range between two different half-pixel-shifted alignments. Each *ESF*, characterised by the same sampling distance Δx, can thus be used to generate a composite *ESF*, with a smaller effective sampling distance. This way, the effect of aliasing on the measured *MTF* can be eliminated [15].

Tomosynthesis acquisitions were performed in manual mode, by selecting the kVp and mAs that would be chosen by the AEC system for a standard test block of 45 mm. The acquisition paramenters are summarised in table 3.9. As it can be seen, DBT scans

System	Acquisition mode	Voltage (kV)	Exposure (mAs)
Selenia Dimensions	Tomo manual	31	40
AMULET Innovality	Tomo ST manual	32	31
AMULET Innovality	Tomo HR manual	32	50

Table 3.9: Acquisition parameters for the EUREF *MTF* edge test.

in HR mode were also acquired with the AMULET Innovality in order to observe the effect of the angular range on the *MTF*.

Since, as it was shown in 2.3.3, geometrical blurring depends on the position above the bucky, acquisitions were repeated with the edge positioned approximately 40 mm and 70 mm above the breast support table. To achieve this, the edge test object was

placed on top of foam spacers also included with Mammo 3D Performance Kits, which were positioned in such a way as to not affect the *MTF* measurement, as shown in figure 3.12.

The kVp and mAs were also changed to values appropriate for the simulated thickness, by referring to the acquisition parameters automatically selected in the AEC system performance test. This is because the exposure factors, hence the breast thickness, can affect the exposure time for a projection image, which in turn largely influences geometric blurring.

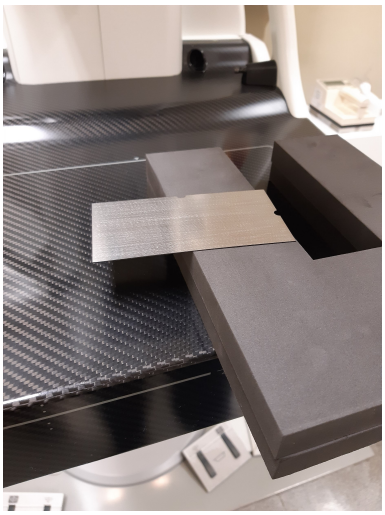

Figure 3.12: Experimental set up for the system projection *MTF* measurement with the Fujifilm AMULET Innovality system at IEO. The edge test object is placed on two foam spacers, at a total height of approximately 40 mm.

Quantitative measurements: MAMMO QC

The measurements were performed on the BPO datasets using the ImageJ plugin "MAMMO QC" [52], which implements the edge method outlined by Samei et al. in their paper [8].

The edge technique aims to prevent the occurrence of aliasing, by computing a finely sampled *ESF*. This is done by re-projecting the grey-level data within a 40 x 40 mm^2 ROI in the linearised image, along the direction of the edge angle, into a one-dimensional array of sub-pixel elements. This results in an array of discrete *ESF* samples, with the sampling rate $\Delta s = 0.1p$, p being the pixel pitch. The *ESF* array is then differentiated to determine the *LSF*. Finally, the *Fast Fourier Tranform FFT* of the *LSF* is carried out, providing the pre-sampling *MTF*, which is lastly normalised to its value at zero frequency [8].

Hence, using the MAMMO QC plugin the pre-sampling *MTF* was measured in both the tube scan and orthoscan directions, by positioning the 40 x 40 mm^2 ROI on the

relevant edge, as shown in figure 3.13. The measurements were carried out on the

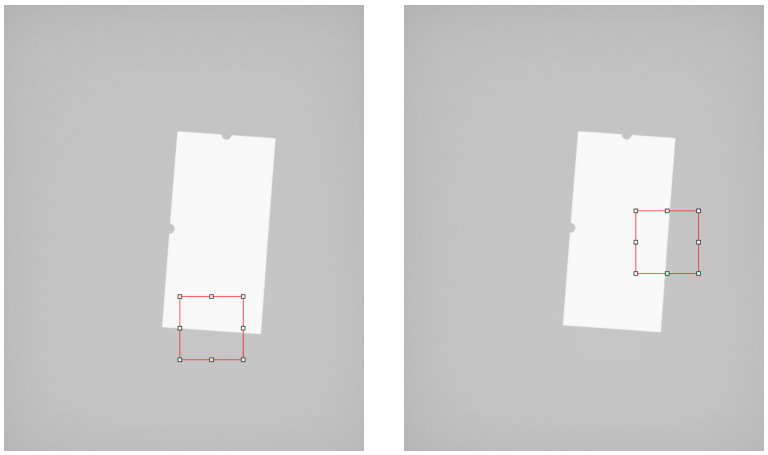

(a) (b)

Figure 3.13: MAMMO QC ROIs of size 40 mm x 40 mm used for measuring the pre-sampling *MTF* along the tube travel (a) and chest wall-nipple (b) directions.

linearised projection image acquired at roughly 0°, that is, whose DICOM tag "0018,1530 Detector Primary Angle" $\approx 0°$. Further pre-sampling *MTF* curves were also acquired from non-zero projection angles in order to characterise blurring due to the oblique incidence [46].

The pre-sampling *MTF* data corresponding to the projections acquired with the edge on the breast support table, represents the detector $MTF(u,v)_{\mathrm{d}}$, since the condition $MTF(u,v)_{\mathrm{geom}} \approx 0$ is reached.

3.5.3 *MTF* in the reconstructed image

The measurement of the *MTF* in the x-y plane of the reconstructed tomosynthesis image, or in more simple terms, the in-plane *MTF*, entails the use of a tungsten wire. Such a test object is available with both CIRS 021 (target slab 1) and Mammo 3D Performance Kits. However, due to damage of the wire during the acquisitions of Mammo 3D Performance Kits, only measurements from CIRS 021 with both DBT systems were available.

Experimental set up

According to the protocol, the wire should be held under tension on 10 mm of PMMA plate, with an additional 5 mm thick PMMA plate placed on top of it. The assembled *MTF* phantom of a total thickness of 15 mm, should then be positioned 40 mm above the breast support table.

Moreover, in order to measure the *MTF* in both the scan and orthoscan directions, two arrangements of the wire should be considered. First the wire is stretched left to right at 60 mm from the chest wall edge, across the detector, for the measurement of the *MTF* in the chest wall-nipple direction. Then, the wire is rotated by 90° so that it is centred left-right, and is perpendicular to the tube travel direction.

Since the target slab of CIRS 021 has a built-in set of wires oriented in the required directions, the arrangement of the phantom was considerably facilitated, and an accurate positioning of the test objects was guaranteed.

Given the thickness of the target slab (10 mm), in reproducing the set-up described above, two arrangements were considered, and are shown in figure 3.14. In figure 3.14a,

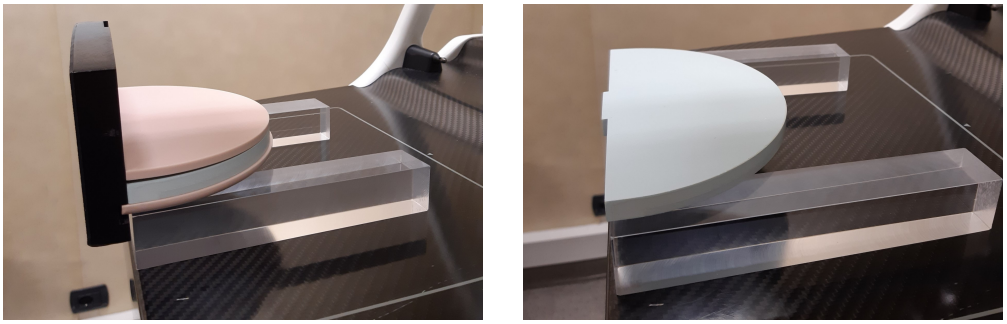

(a) (b)

Figure 3.14: Different arrangements of CIRS 021 with target slab 1 (blue), on the Fujifilm AMULET Innovality system at IEO.

the target slab (in blue) was stacked between 10 mm and 5 mm thick homogeneous slabs (in pink), reaching a total thickness of 25 mm. The phantom was then placed on top of 30 mm thick PMMA plates, included with Mammo 3D Performance Kits. This way, assuming the wires are roughly in the middle of the target slab, a total height of 45 mm above the breast support table was reached. In the set-up shown in figure 3.14b on the other hand, only the target slab was included, positioned once again above the 30 mm thick PMMA spacers. Thus, the wires were this time held at approximately 35 mm above the breast support table.

Tomosynthesis acquisitions were performed in manual mode, setting the exposure parameters that would be chosen by the AEC system for a phantom thickness of 45 mm. These were 31 kVp and 40 mAs on the Selenia Dimensions. Acquisitions with the Innovality were performed in both the ST and HR modes, setting the voltage and exposure to 32 kVp and 32 mAs, and 32 kVp and 50 mAs respectively.

Quantitative measurements

MAMMO QC also includes a plugin for the calculation of the pre-sampling *MTF* in the reconstructed images. The method implemented is mostly based on the routine described by Samei et al. [8], with some differences deriving from the use of a different test object.

As a matter of fact, from the image of the wire it is possible to construct the *LSF*. In doing so, the effect of non-uniformities in the background needs to be minimised. The plugin achieves this by performing a two-dimensional fit to the ROI containing the wire. The resulting surface is then subtracted from the ROI before determining the finely sampled *LSF*. This way, any low frequency trends, e.g., large area spatial variations, are removed [26]. The pre-sampling *MTF* is finally computed by taking the modulus of the *FFT* of the *LSF*, which is then normalised to its maximum value [46]. In applying the

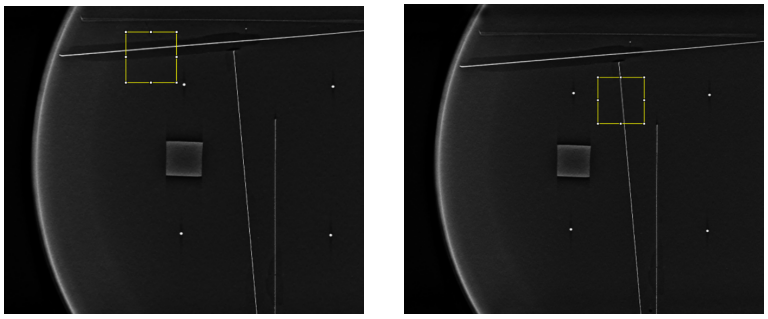

(a) (b)

Figure 3.15: MAMMO QC ROIs of size 15 mm x 15 mm used for measuring the pre-sampling *MTF* in the x-y plane, along the tube travel (a) and chest wall-nipple (b) directions.

MAMMO QC plugin to the BTO images of target slab 1, care was taken in positioning the ROI so as not to include the other imaging targets present in the phantom slab, as shown in figure 3.15.

3.5.4 Z-resolution with spheroidal masses of varying diameter

Following the same experimental set up described in 3.4.2, acquisitions of CIRS 021 with the Selenia Dimensions at Molinette Hospital and the AMULET Innovality at IEO were repeated. However, the target slab containing the array of spheres was this time replaced by the one represented in figure 3.1b.

The goal was to compute the *ASF* from spheroidal masses of varying diameter effectively simulating small mass lesions. It should be noted that these test objects are meant to be used for visual pass-fail evaluation, and are therefore made of breast tissue equivalent material [4]. As a result, the local contrast is reduced, compared to the

ceramic and aluminium spheres seen in the previous section. For this reason, only the masses that were always visible in the BTO images were chosen, which had a diameter of 6.3 mm, 4.7 mm and 3.9 mm. These are shown in figure 3.16.

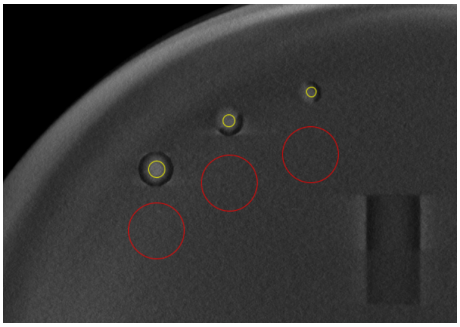

Figure 3.16: Spheroidal masses included in target 2 of CIRS 021, together with the ROIs used for the ASF computation.

The signal produced by the masses was measured in ROIs of size half the diameter of the spheres, as shown in figure 3.16. The background mean pixel values and standard deviations were instead sampled from ROIs of size 100 x 100 pixels. The ASF was then computed following the same procedure described in 3.4.2, however, the ROIs in figure 3.16 were selected manually.

Chapter 4

Results and discussion

In this final chapter the experimental results obtained from the measurements outlined in Chapter 3 will be presented and discussed. Throughout the analysis, as well as assessing whether the system components under evaluation meet the protocol requirements, the features of each phantoms and their impact on the calculations will also be highlighted.

4.1 Part one: comparison of phantoms for a given DBT system

4.1.1 AEC system performance

Hologic Selenia Dimensions

The *SDNR* was calculated on tomosynthesis projection images of CIRS 021 and Mammo 3D Performance Kits, acquired with the Hologic Selenia Dimensions system at Molinette Hospital. The results are reported in tables 4.1 and 4.2. In addition to the *SDNR* values computed for each phantom thickness, an estimate of the entrance dose is also included, which was extracted from the respective DICOM tag, indicating the average dose measured at the surface of the phantom. The *SDNR* values were also plotted as a function of phantom thickness, as shown in figure 4.1.

The curves indicate that in both phantoms, as expected, the *SDNR* decreases as a function of phantom thickness. Such behaviour is a manifestation of the adverse effect of scattering. As it was previously discussed, the scattering cross section is approximately constant in the mammography energy range, with scattering mostly depending on the breast thickness and on the size of the FOV. As a matter of fact, figure 1.17 showed an increasing scatter-to-primary ratio (*SPR*) with breast thickness. The scattered radiation leads to a reduction in signal difference and an increase of random noise, thus degrading the *SDNR*.

Phantom thickness (mm)	Body part thickness (mm)	kVp	mAs	Entrance dose (mGy)	*SDNR*
20	21	26	35	2	4.9 ± 0.1
30	32	28	36	3	3.8 ± 0.1
40	45	30	41	4	3.1 ± 0.1
45	53	31	46	5	3.0 ± 0.2
50	60	33	48	6	2.7 ± 0.1
60	75	36	56	9	2.6 ± 0.1
70	90	42	52	12	2.1 ± 0.1

Table 4.1: *SDNR* measured in projection images of Mammo 3D Performance Kits acquired with the Selenia Dimensions. Propagation of uncertainty was used to estimate the errors. The entrance dose was extracted from the respective DICOM tag.

Phantom thickness (mm)	Body part thickness (mm)	kVp	mAs	Entrance dose (mGy)	*SDNR*
20	21	26	37	2	4.9 ± 0.1
30	32	28	38	3	3.8 ± 0.1
40	45	30	42	4	3.2 ± 0.2
45	53	31	46	5	2.9 ± 0.1
50	60	33	47	6	2.8 ± 0.2
60	75	36	59	9	2.6 ± 0.1
70	90	42	53	12	2.2 ± 0.2

Table 4.2: *SDNR* measured in projection images of CIRS 021 acquired with the Selenia Dimensions. Propagation of uncertainty was used to estimate the errors. The entrance dose was extracted from the respective DICOM tag.

The reported data demonstrates that the *SDNR* results obtained from the two phantoms are in agreement. The slight discrepancies, which are nevertheless contained within the uncertainty ranges, can be first of all explained by the difference in background material (PMMA and BR50/50), affecting the level of exposure established by the AEC system. In fact, the mAs values are determined during the pre-exposure of the phantom, and are therefore dependent on the beam attenuation properties of the material.

The *SDNR* is also influenced by the position of the ROIs used for the pixel value and standard deviation measurements, which in turn depends on the location of the aluminium plate. The reason for this is the heel effect, which consists of the anode self-filtration of x-rays directed towards the anode side of the field, leading to variations in the x-ray beam intensity [17].

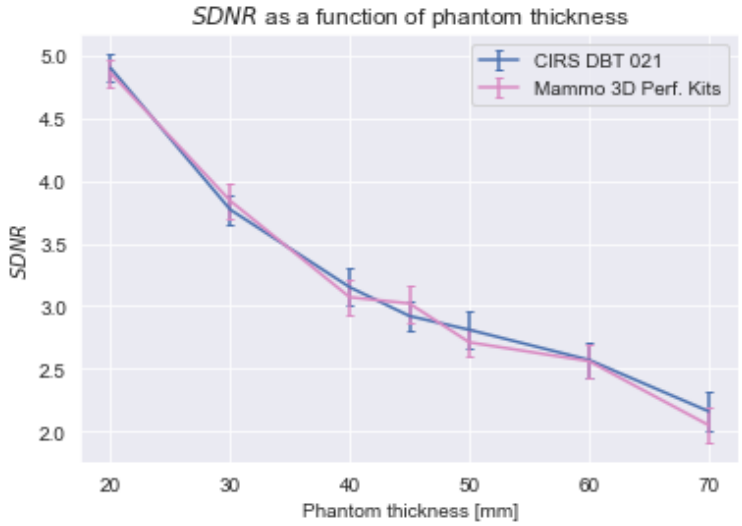

Figure 4.1: *SDNR* as a function of PMMA thickness, measured in projection images of CIRS 021 and Mammo 3D Performance Kits acquired with the Selenia Dimensions.

Ideally, the coordinates of the ROIs are the same in all projection images. However, this condition could not be achieved in the measurements because of the following reasons. First of all, the location of the imaging target differs between the two phantoms. Mammo 3D Performance Kits allows the user to adjust the Al insert according to the EUREF guidelines, i.e. with its centre at 60 mm from the chest wall edge. On the other hand, this option is not available with CIRS 021, being the Al plate integral to the target slab, and at a distance of approximately 50 mm from the chest wall edge side.

Moreover, when using Mammo 3D Performance Kits, the Al plate is subjected to movements between acquisitions, as more PMMA layers are added to the phantom. For this reason, during the measurements it was often required to readjust the position of the ROI, so that it would be centred in the imaging target. This variability inevitably impacted the *SDNR* calculation. As an example, figure 4.2 shows the *SDNR* as a function of PMMA thickness, for three datasets of Mammo 3D Performance Kits, acquired from the same system at Tecnologie Avanzate. The repeatability between the measurements was assessed by computing the coefficient of variation (COV) according to:

$$COV = \frac{\hat{\sigma}}{\mu} \tag{4.1}$$

where $\hat{\sigma}$ is the standard deviation estimated from the three *SDNR* measurements, and μ is the computed average. The COV was found to be within 2% to 6%.

Also shown in figure 4.2 is the *SDNR* calculated from FFDM acquisitions, which is approximately a factor of 2 greater than in tomosynthesis mode. The corresponding data is listed in table 4.3, and indicate that in 2D mode the AEC system selected exposure

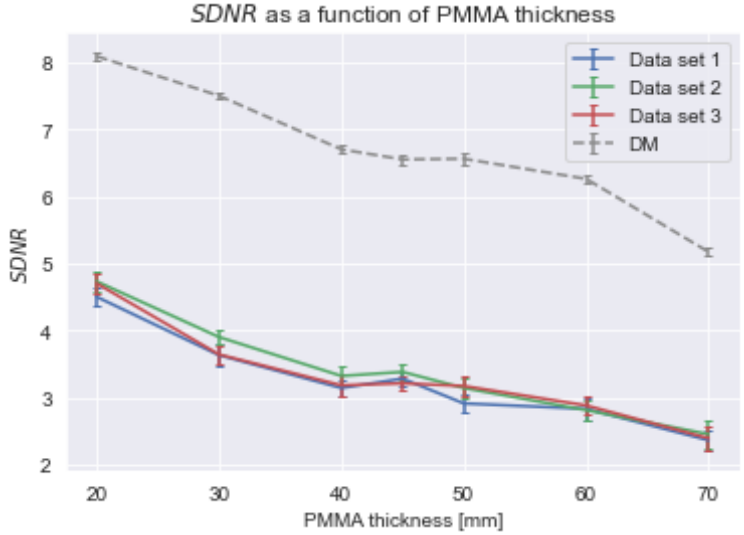

Figure 4.2: *SDNR* as a function of PMMA thickness, measured in three datasets acquired with the Selenia Dimensions at Tecnologie Avanzate. The dashed curve (DM) is the *SDNR* calculated in the FFDM images.

levels twice as big as the tomosynthesis mAs values. This is due to the presence of the

Phantom thickness (mm)	Body part thickness (mm)	kVp	mAs	Entrance dose (mGy)	*SDNR*
20	21	25	43	1	8.09 ± 0.05
30	32	26	63	2	7.50 ± 0.05
40	45	28	78	3	6.70 ± 0.06
45	53	29	96	4	6.55 ± 0.08
50	60	31	118	6	6.56 ± 0.08
60	75	31	138	9	6.26 ± 0.06
70	90	34	136	12	5.17 ± 0.06

Table 4.3: *SDNR* measured in 2D planar images of Mammo 3D Performance Kits acquired with the Hologic Selenia Dimensions at Tecnologie Avanzate. Propagation of uncertainty was used to estimate the errors. The entrance dose was extracted from the respective DICOM tag.

anti-scatter grid, resulting in a reduction of the photon fluence reaching the detector. Greater exposure levels thus ensure that the transmitted fraction of photons is sufficient to deliver an appropriate entrance dose, whose values are in fact comparable to the ones in table 4.1. The greater *SDNR* could therefore be explained by the differing anode filter

combinations used in 2D, namely W/Rh and W/Ag.

Fujifilm AMULET Innovality

Tables 4.4 and 4.5 report the *SDNR* calculated in projection images of Mammo 3D Performance Kits and CIRS 021, acquired with the Fujifilm AMULET Innovality system at IEO. Also shown in figure 4.3 are the *SDNR* values plotted as a function of phantom thickness.

Phantom thickness (mm)	Body part thickness (mm)	kVp	mAs	Entrance dose (mGy)	*SDNR*
20	21	27	24	2	6.9 ± 0.1
30	32	29	23	2	4.9 ± 0.2
40	45	31	26	3	3.8 ± 0.2
45	53	32	31	5	3.7 ± 0.2
50	60	33	35	5	3.3 ± 0.2
60	75	36	41	8	2.9 ± 0.2
70	90	37	48	11	2.4 ± 0.2

Table 4.4: *SDNR* measured in projection images of Mammo 3D Performance Kits acquired with the AMULET Innovality. Propagation of uncertainty was used to estimate the errors. The entrance dose was extracted from the respective DICOM tag.

Phantom thickness (mm)	Body part thickness (mm)	kVp	mAs	Entrance dose (mGy)	*SDNR*
20	21	27	21	2	6.3 ± 0.2
30	32	29	23	2	4.6 ± 0.2
40	45	31	26	3	3.6 ± 0.1
45	53	32	31	4	3.6 ± 0.2
50	60	33	34	5	3.1 ± 0.2
60	75	36	41	7	2.6 ± 0.2
70	90	37	48	11	2.3 ± 0.2

Table 4.5: *SDNR* measured in projection images of CIRS 021 acquired with the AMULET Innovality. Propagation of uncertainty was used to estimate the errors. The entrance dose was extracted from the respective DICOM tag.

Once again, as more phantom layers are added, the *SDNR* decreases because of scattering. The two phantoms produce differing results for the 20 mm and 70 mm

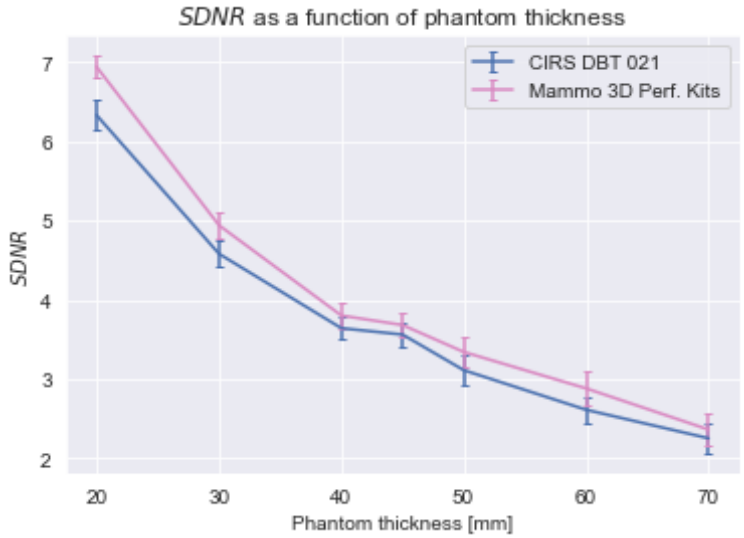

Figure 4.3: *SDNR* as a function of PMMA thickness, measured in projection images of CIRS 021 and Mammo 3D Performance Kits acquired with the AMULET Innovality system.

thickness values, with a difference between the computed *SDNR* of approximately 3σ and σ respectively. On the other hand, taking into account the uncertainty ranges, the *SDNR* measured in the additional phantom layers are in agreement. This suggests that for lower thickness values, hence lower doses, greater contrast could be produced by PMMA. As more phantom layers are added, and hence the *SPR* is increased, the apparent greater attenuation produced by BR50/50 could be compensated for by the current-time product selected by the AEC system, resulting in the convergent curves in 4.3. Nevertheless, repeated measurements from both phantoms with the same system are required to confirm this pattern.

In conclusion, considering the differences in design between DBT systems and the resultant variability in the computed technical parameters, limiting values for the *SDNR* have not yet been established in the EUREF protocol. It is instead suggested that the output measurements are taken as a reference for stability testing. In this regard, from the analysis that has been presented so far, it can therefore be concluded that both Mammo 3D Performance Kits and CIRS 021 fulfil the protocol requirements for the assessment of the AEC system performance.

4.1.2 Z-resolution

ROI size

First of all, the two methods described in section 3.4.2, were tested on the four datasets of Mammo 3D Performance Kits, acquired with the Selenia Dimensions. The results are reported in table 4.6. Taking into account the associated uncertainties, the results

	ASF FWHM (mm)	
Dataset	Method 1	Method 2
Lab 1	11.7 ± 0.4	10.8 ± 0.3
Lab 2	11.4 ± 0.3	10.8 ± 0.3
San Martino	11.8 ± 0.4	11.2 ± 0.3
Molinette	11.6 ± 0.3	10.9 ± 0.3

Table 4.6: Comparison of two methods for the computation of the *ASF FWHM*, with three different Selenia Dimensions systems. Propagation of uncertainty was used to estimate the errors.

obtained from the different DBT systems, using both methods, are in agreement with each other, and with the available literature [46], [9]. Moreover the COV is 1.5% and 1.7% with methods 1 and 2 respectively.

However, in method 1 the average pixel value is used to quantify the signal produced by the sphere, as opposed to the maximum value considered in method 2. The advantage of this approach would be a greater *SNR* for the sphere, resulting from the increased statistics provided by the 7 x 7 pixels in the ROI, hence lower statistical noise. For this reason, method 1 was chosen for the analysis.

Hologic Selenia Dimensions

ASF profiles along the z-direction were obtained from the spheres within the useful FOV, and the average of the *FWHM* values was used to characterise the degree of artefact spreading [46]. In figure 4.4 the *ASF* as a function of the distance from the breast support table is shown, calculated from one sphere of both phantoms, positioned at a height of roughly 35 mm. Since the reconstructed planes are separated by 1 mm, the distance from the breast support table is equivalent to the slice number.

As expected, the peak of the *ASF* occurs at the slice corresponding to the in-focus plane. The latter, however, slightly deviates from the expected focal plane. In fact, considering the experimental set up with the array of spheres between the third and fourth homogeneous slabs, the in-focus plane was at approximately 33 mm in Mammo 3D Performance Kits, and 36 mm in CIRS 021.

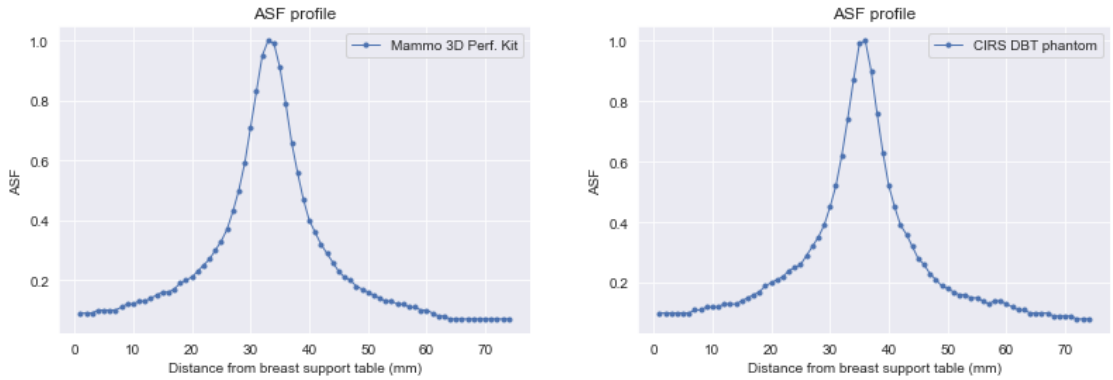

(a) (b)

Figure 4.4: *ASF* as a function of the distance from the breast support table (a) Mammo 3D Performance Kits (b) CIRS 021.

Moreover, at first glance, it can be noticed that the *ASF* profile produced by CIRS 021 is slightly narrower than that of Mammo 3D Performance Kits. This is confirmed by the values reported in table 4.7, which represent the average of the *ASF FWHM* calculated from 12 spheres of Mammo 3D Performance Kits, and 8 spheres of CIRS 021. As it can be seen, the values differ by a factor of approximately 1.1, and, taking into account their uncertainties, they are separated by one to two standard deviations. The reason for this lies in the difference between the phantoms' imaging targets.

	ASF FWHM (mm)		
Height above table (mm)	Mammo 3D Perf. Kits	CIRS 021	Ratio
15	12.8 ± 0.4	12.1 ± 0.4	1.06
35	11.8 ± 0.4	10.7 ± 0.4	1.1
55	11.2 ± 0.3	10.5 ± 0.4	1.06

Table 4.7: Average *FWHM* of the *ASF* profiles for the Selenia Dimensions. Propagation of uncertainty was used to estimate the errors.

Previous studies have shown that the *ASF* strongly depends on the magnitude of the initial in-plane stimulus, which is in turn determined by the size and composition of the detail used. In particular, it has been demonstrated that the *ASF* profile produced by small test objects is usually narrower [46]. The results in table 4.7 are consistent with this statement, since the spheres in CIRS 021 have a diameter of 0.8 mm, as opposed to the 1 mm diameter spheres of Mammo 3D Performance Kits.

As well as a different diameter, the details of the phantoms are made of differing materials, namely aluminium in Mammo 3D Performance Kits and ceramic in CIRS 021. Given the greater density of ceramic (about 6 g/cm^{-3}) compared to that of aluminium (2.7 g/cm^{-3}), the details in CIRS 021 are expected to produce a greater attenuation of the x-ray beam, hence superior contrast. As a consequence, a more extended signal spread would be expected in CIRS 021 . However, this was not confirmed by the results, suggesting that, for the Selenia Dimensions, the difference in diameter, although small, could have a greater influence on the *ASF*, than the detail composition.

Also in agreement with the literature is the slight reduction in *FWHM* (at most by 12%) as the height above the breast support table of the phantom layer containing the spheres is increased. This is explained by the increase in the apparent angular range at the position of the sphere, as the height of the sphere is increased above the detector [46].

Fujifilm AMULET Innovality

Tables 4.8 and 4.9 list the average *ASF FWHM* calculated from the spheres of both phantoms, for the HR and ST mode respectively. As expected, the data corresponding to the 0.8 mm spheres of CIRS 021 are lower by a maximum factor of 1.17 in the HR mode, and 1.24 in the ST acquisitions.

	ASF FWHM (mm)		
Height above table (mm)	Mammo 3D Perf. Kits	CIRS 021	Ratio
15	3.4 ± 0.1	2.9 ± 0.1	1.17
35	3.3 ± 0.1	3.0 ± 0.1	1.1
55	3.3 ± 0.1	2.9 ± 0.1	1.14

Table 4.8: Average *FWHM* of the *ASF* profiles, HR mode. Propagation of uncertainty was used to estimate the errors.

The results also confirm that the wide angle of the HR mode ($\pm$ 20°) leads to a better resolution in the direction perpendicular to the reconstructed planes, as quantified by the *ASF FWHM*. The latter, is increased by nearly a factor of 3 when computed from the 1 mm spheres of Mammo 3D Performance Kits imaged in HR mode, in line with the data in [10]. Whereas, considering the 0.8 mm spheres of CIRS 021, the HR and ST results differ by a factor of 2.3.

The effect of the wide angle characterising the HR mode is reflected by the narrower *ASF* profiles shown in figure 4.5. Similarly to the curves in figure 4.4, the *ASF* profiles were obtained with the array of spheres positioned at roughly 35 mm above the breast

Height above table (mm)	*ASF FWHM* (mm)		Ratio
	Mammo 3D Perf. Kits	CIRS 021	
15	8.3 ± 0.1	6.7 ± 0.1	1.24
35	8.3 ± 0.1	6.7 ± 0.1	1.24
55	7.9 ± 0.1	6.6 ± 0.2	1.2

Table 4.9: *FWHM* of the *ASF* profiles, ST mode. Propagation of uncertainty was used to estimate the errors.

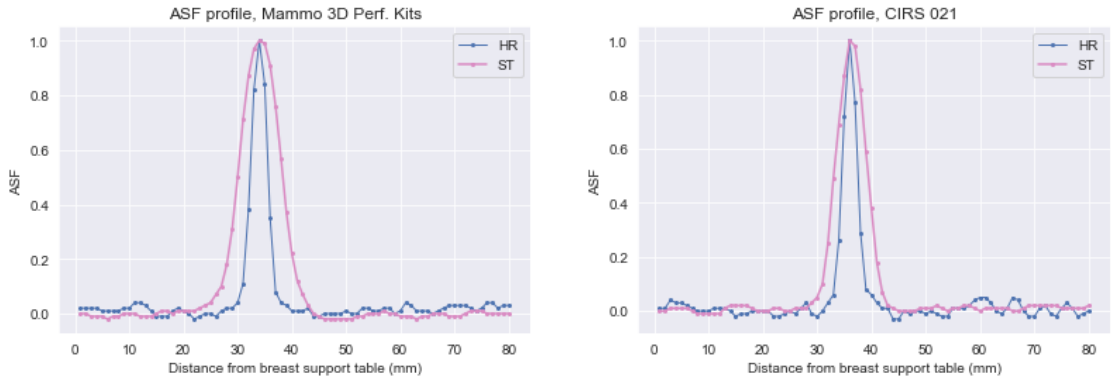

(a) (b)

Figure 4.5: *ASF* with the phantom at approximately 35 mm from the breast support table, for the ST and HR modes of the Innovality (a) Mammo 3D Performance Kits (b) CIRS 021.

support table. Once again, the maximum *ASF* value occurs at the distance corresponding to the in-focus plane, which slightly differs between the two phantoms.

Finally, a modest reduction (at most by 5%) in the *ASF FWHM*, i.e., an improvement of resolution, as the distance from the detector is increased was only observed in the ST acquisitions. This is also consistent with the literature [46].

Overall, it was found that both Mammo 3D Performance Kits and CIRS 021 make it possible to estimate the z-resolution of a DBT system, in terms of the *ASF*. Therefore, the two phantoms can be used to establish baseline values for constancy testing, as it is suggested in the current version of the EUREF DBT QC protocol [59].

4.2 Part two: phantom performance in the physical characterisation of DBT systems

4.2.1 Response function and noise analysis of the image receptor

Response function

The response function of the Selenia Dimensions was found to be linear, with $R^2 = 0.999$. A logarithmic trend with $R^2 = 0.999$, was instead confirmed for the Innovality. The response functions are shown in figures 4.6a and 4.6b, and were obtained by fitting respectively linear and logarithmic curves to the mean pixel values, measured in the 5 x 5 mm^2 ROI, as a function of the exposure.

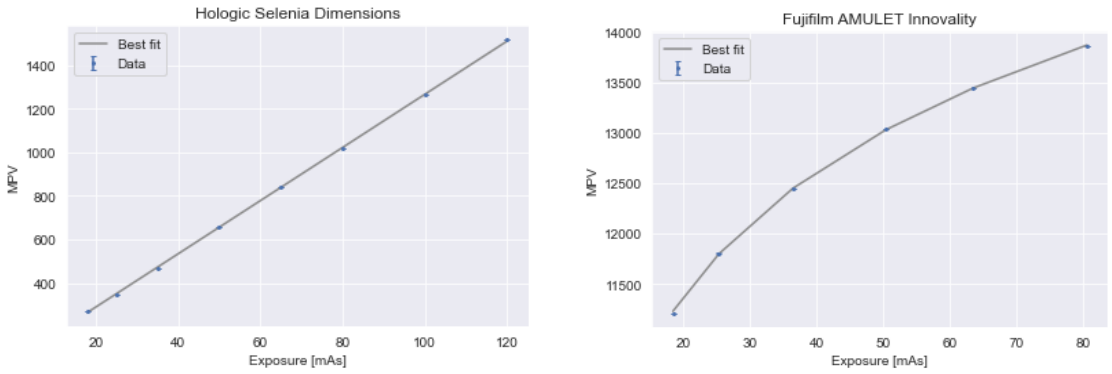

(a) (b)

Figure 4.6: Mean pixel value measured in a 5 mm x 5 mm ROI in first projection images, as a function of the exposure (mAs) (a) linear detector response of the Selenia Dimenions (b) logarithmic detector response of the AMULET Innovality.

The coefficients outputted by the linear and logarithmic fits can be found in table 4.10, where the gain is the gradient term of the response function, namely the coefficient m, whereas the offset q is added to prevent negative pixel values. It was found that the fitted coefficients are coherent with the values found in the literature [46], [9].

Since the response function of the Innovality is logarithmic, linearisation of the pixel values needed to be performed, before proceeding with the noise analysis. This was done by using the inverse of the response function:

$$\mu'_p = e^{\frac{\mu_p - q}{m}} \tag{4.2}$$

where μ_p is the mean pixel value measured in the 5 x 5 mm^2 ROI, and q and m are the coefficients outputted by the logarithmic fit. Likewise, the linearised standard deviation

System	Response	m	q
Selenia Dimensions	$PV = m \cdot (Exposure) + q$	12.215 ± 0.003	44.5 ± 0.1
AMULET Innovality	$PV = m \cdot \ln(Exposure) + q$	1793.4 ± 0.5	6000 ± 2

Table 4.10: Response function coefficients. The uncertainty was calculated from the covariance matrix outputted by the fits. Units for the m and q coefficients are $(\text{mAs})^{-1}$ and arbitrary digital units respectively [46].

is:

$$\sigma' = |(\mu_p + \sigma_p)' - (\mu_p)'| \tag{4.3}$$

where σ_p is the measured standard deviation and $(\cdot)'$ denotes linearisation using equation 4.2 [41]. Although linear, the inverse of the response function of the Selenia Dimensions was also used to recompute the mAs values, in order to improve accuracy at low exposure levels [28].

Noise analysis

Using the same datasets with which the response functions were determined, the individual noise components were computed at every exposure level, by fitting a curve to the SD^2 plotted as a function of the detector air kerma. The fitted coefficients can be found in table 4.11, and could be used to verify the stability of the DBT systems, as recommended by the protocol [59]. By squaring the computed noise component coefficients, it

	Noise component coefficients		
System	k_e	k_q	k_s
Selenia Dimensions	$(1.6 \pm 0.6) \times 10^{-1}$	$(8.3 \pm 0.4) \times 10^{-2}$	$(4.8 \pm 0.6) \times 10^{-3}$
AMULET Innovality	$(9 \pm 5) \times 10^{-2}$	$(6.3 \pm 0.4) \times 10^{-2}$	$(3.7 \pm 0.6) \times 10^{-3}$

Table 4.11: Noise component coefficients outputted by a fit to the measured variance as a function of the detector air kerma, for the Hologic Selenia Dimensions and Fujifilm AMULET Innovality systems.

was also found that the results are of the same order of magnitude as the data reported in [46], in which squared fit coefficients were found.

In figure 4.7 the percentage contribution of each noise source to the total noise is plotted as a function of the detector air kerma, for the two DBT systems. In both cases, as expected, the quantum noise component denoted by q is dominant and slowly decreases as a function of dose. With regards to the electronic and structured noise, figure 4.7 shows that e dominates over s at the lowest dose levels, to then decrease to

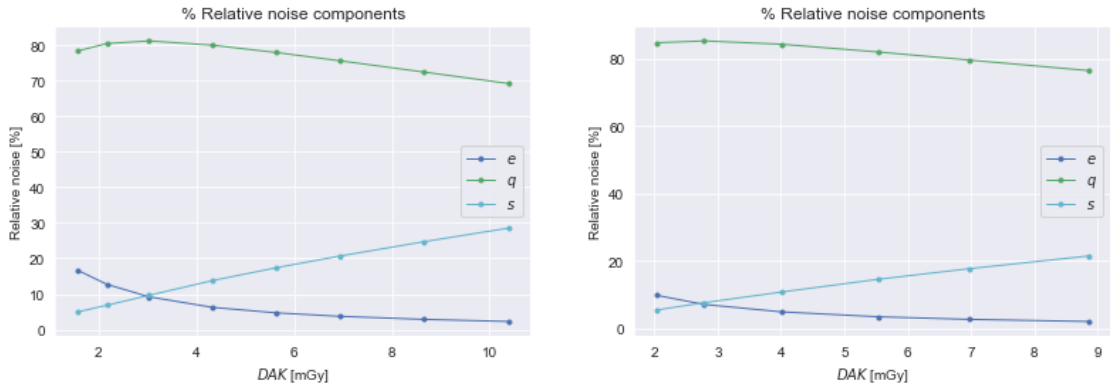

(a) (b)

Figure 4.7: Percentage contribution of each noise source to the total noise measured in first projection images (a) Hologic Selenia Dimensions (b) Fujifilm AMULET Innovality.

a constant value, no longer exhibiting a dependence on dose. On the other hand, the increase of s with exposure is confirmed.

For comparison purposes, the standard clinical entrance dose chosen by the AEC system for a phantom thickness of 45 mm is generally taken as a reference. By referring to tables 4.1 and 4.4, this is 4.5 mGy in the Selenia Dimensions and 4.2 mGy in the Innovality. Using the inverse square law, the values correspond to a *DAK* of 3.9 mGy

	Relative noise component		
System	e	q	s
Selenia Dimensions	6%	80%	14%
AMULET Innovality	5%	84%	11%

Table 4.12: Percentage relative noise for each noise component at the standard clinical entrance doses of 4.5 mGy and 4.2 mGy.

and 3.6 mGy respectively. The contribution of each noise component to the total noise at the clinical entrance dose can be found in table 4.12. The values are also in line with the data reported in the relevant literature [9].

4.2.2 System projection *MTF*

Figure 4.8 shows the pre-sampling *MTF* calculated with MAMMO QC, in the tomosynthesis projection images of the edge test object included with Mammo 3D Performance

Kits, for the Selenia Dimensions. Each curve corresponds to the edge positioned at different heights above the breast support table, and represents the average of two repeated acquisitions.

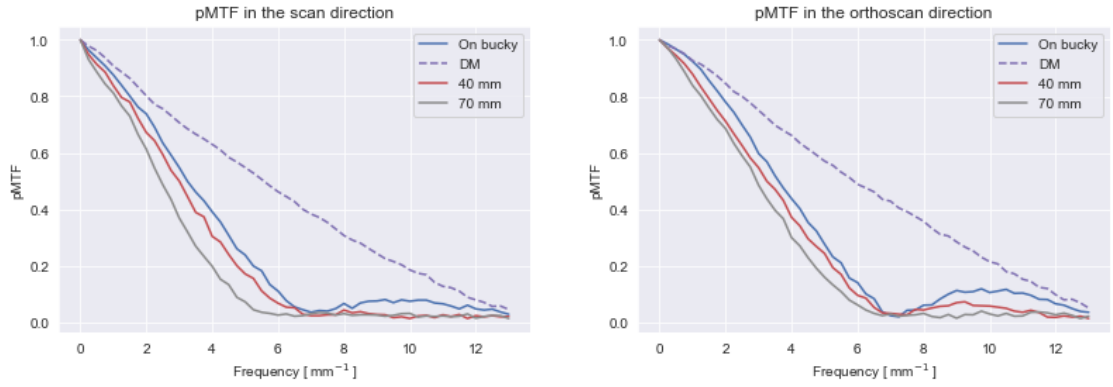

(a) (b)

Figure 4.8: Pre-sampling *MTF* curves measured in the zero-degree BPO images of the Selenia Dimensions at Tecnologie Avanzate, with the edge at different heights above the bucky (a) *pMTF* in the tube travel (scan) direction (b) *pMTF* in the chest wall-nipple (orthoscan) direction.

First of all, by inspecting the curves in 4.8a, a decrease of the pre-sampling *MTF* as a function of the distance from the breast support table can be observed. More specifically, taking as a reference the frequency at which a 50% reduction of the *pMTF* occurs, denoted as MTF_{50}, a difference of approximately 27% was found between the values measured with the edge on the bucky, and at a distance of about 70 mm above it.

The reason for this is that, as the distance from the breast support table is increased, so is the projected size of the focal spot, contributing to the geometric blurring MTF_{geom}. Moreover, previous studies have shown that blurring from tube motion also increases with the height above the table [45].

The *pMTF* was also measured in FFDM acquisitions with the edge placed on the breast support table, and is represented by the dashed curves in figure 4.8. As it can be seen, since there is no tube motion, FFDM provides greater sharpness in both directions. Moreover, being the edge the closest it can be to the detector, $MTF_{\text{geom}} \approx 1$, and the measured *pMTF* can be taken to be an estimate of the sharpness of the detector, that is MTF_{d} in equation 2.10.

Looking now at figure 4.9, it can be noticed that, as expected, computing the *pMTF* in the scan and orthoscan directions leads to differing results. As a matter of fact the MTF_{50} in the chest-wall nipple direction is increased by 11% for the edge on the breast support table, up to 17% with the edge at 70 mm. Demonstrated in the literature [46],

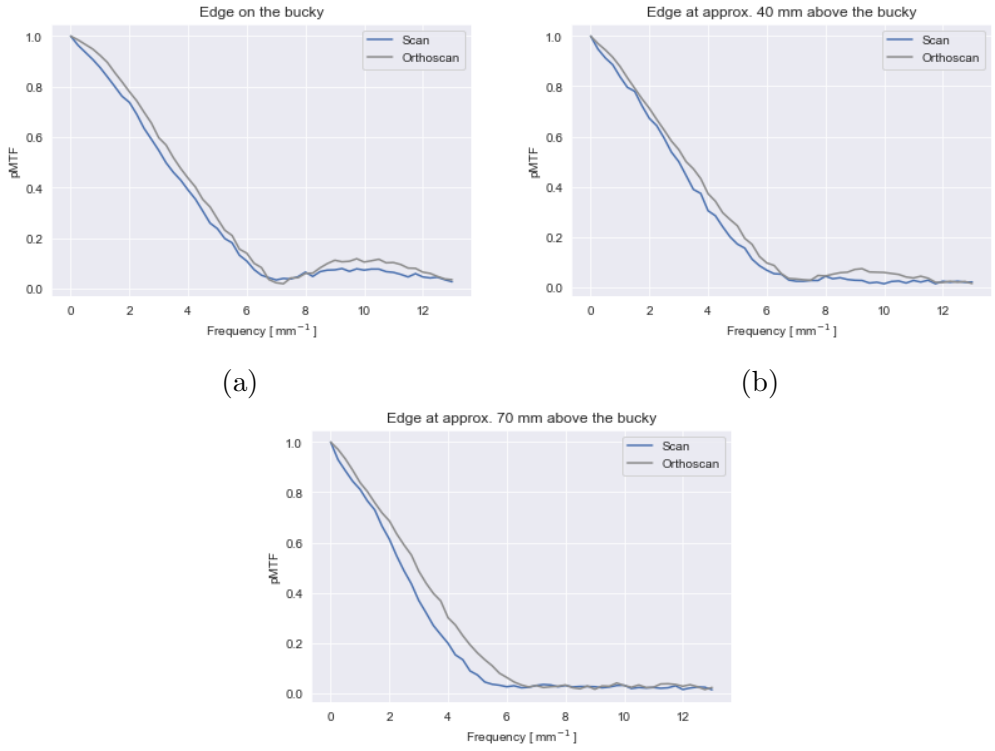

Figure 4.9: Comparison between the *pMTF* curves computed in the tube travel (scan) and chest-wall nipple (orthoscan) directions, in the Selenia Dimensions dataset. The edge test object is placed (a) on the bucky (b) at approximately 40 mm and (c) at approximately 70 mm.

this anisotropy of the *MTF* is due to the absence of the focal spot motion in the orthoscan direction, with only the extended size of the focal spot contributing to geometric blurring.

Similarly, figure 4.10 shows the pre-sampling *MTF* curves measured in the zero degree tomosynthesis projection images, acquired in ST mode with the AMULET Innovality. Once again, the different curves in each graph correspond to a different height of the edge test object above the breast support table.

The system projection *MTF* of the AMULET Innovality also deteriorates as a function of the height above the bucky, consistently with the expected behaviour [9], [45]. In this case the MTF_{50} at 70 mm is reduced by 32%, compared to the value measured with the edge on the breast support table. In addition to this, as anticipated, being unaffected by the focal spot motion, the MTF_{50} in the orthoscan direction is increased by 24% up to 50% the values measured in the scan direction, as shown in figure 4.11a. Additionally, from the overlapping curves in figure 4.10b, it can be inferred that the effect of the focus

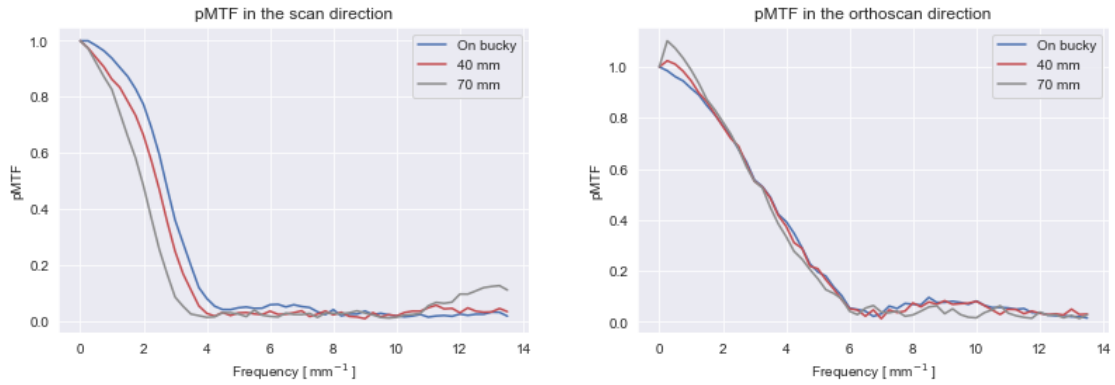

(a) (b)

Figure 4.10: Pre-sampling *MTF* curves measured in the zero-degree BPO images of the AMULET Innovality at IEO, with the edge at different heights above the bucky (a) *pMTF* in the tube travel (scan) direction (b) *pMTF* in the chest wall-nipple (orthoscan) direction.

on the *pMTF* measured in the orthoscan direction is almost negligible.

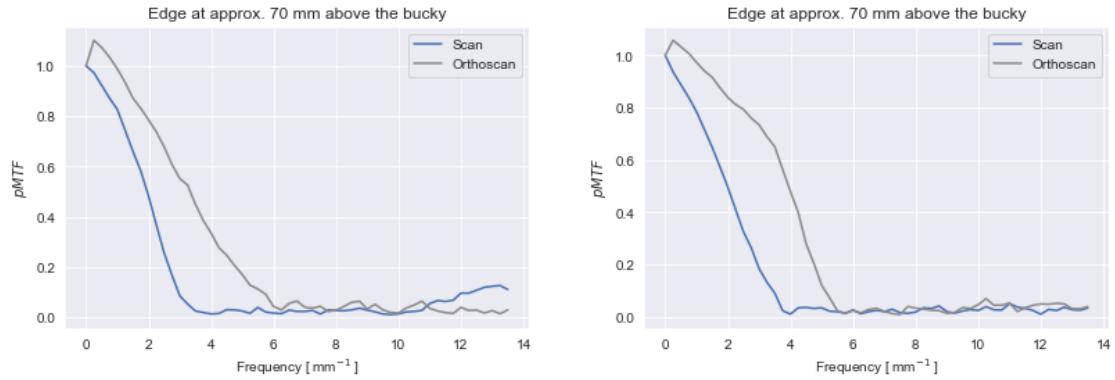

(a) ST (b) HR

Figure 4.11: Comparison between the *pMTF* curves computed in the tube travel (scan) and chest-wall nipple (orthoscan) directions, from the Innovality (a) ST and (b) HR datasets. The edge test object is placed approximately 70 mm above the bucky.

By comparing the *pMTF* curves of the two DBT systems (figures 4.8a and 4.10a), slight discrepancies were observed. Considering that the two datasets were acquired with the same angular range (15°), this is most likely due to differences at the detector level between the two DBT systems [46].

Finally, the *pMTF* curves measured in projection images acquired in the HR mode

are presented in figure 4.12. Looking at the *pMTF* in the scan direction (4.12a), the

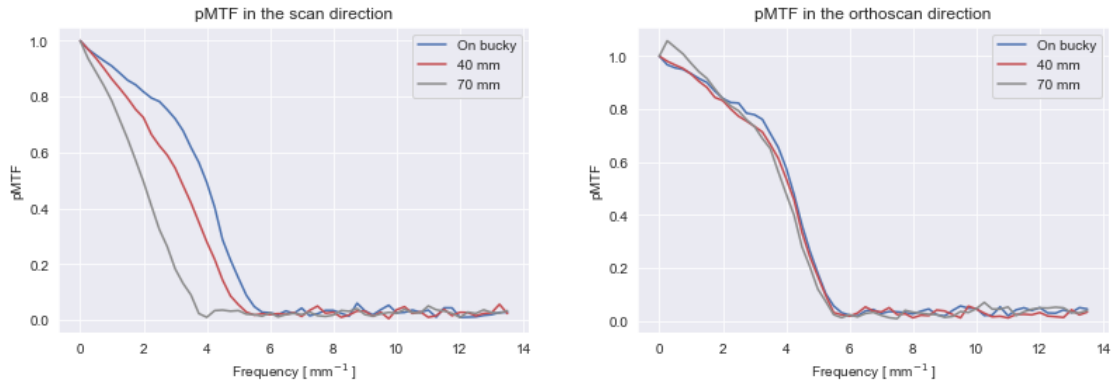

(a) (b)

Figure 4.12: Pre-sampling *MTF* curves measured in the zero-degree BPO images of the AMULET Innovality (HR mode), with the edge at different heights above the bucky (a) *pMTF* in the tube travel (scan) direction (b) *pMTF* in the chest wall-nipple (orthoscan) direction.

first striking feature is the pronounced variation with the height above the bucky, with the MTF_{50} being considerably reduced by 60%. On the other hand, the increase of the MTF_{50} in the orthoscan direction compared to the tube travel direction ranges from 5% when the edge in on the bucky, to 66% with the edge at 70 mm, which is illustrated by the curves in figure 4.11b.

To observe the effect of the angular range on the *pMTF*, measurements were repeated on the first projection image of the ST and HR datasets, which correspond respectively to a projection angle of roughly $-7.5°$ and $-20°$. Because of the oblique incidence of the x-ray beam, it was expected that the projection image acquired in ST mode would output a greater *pMTF*.

However, the effect of the wider scan angle only became noticeable for the measurements with the edge at 70 mm, for which the MTF_{50} computed in HR mode was lower by 26%, as seen in figure 4.13a. This could be related to an increase in the apparent tomosynthesis angle as the height above the detector is increased, which was mentioned in the z-resolution assessment, that would therefore enhance the effect of the x-ray oblique incidence.

To conclude this part, a summary of the spatial frequencies at MTF_{50} and MTF_{10} measured with both DBT systems, with the edge test object at approximately 40 mm, is provided in table 4.13. As it is recommended by the EUREF protocol, this type of data could be used as a reference in future constancy testing measurements, which should stay within 10% of the baseline values.

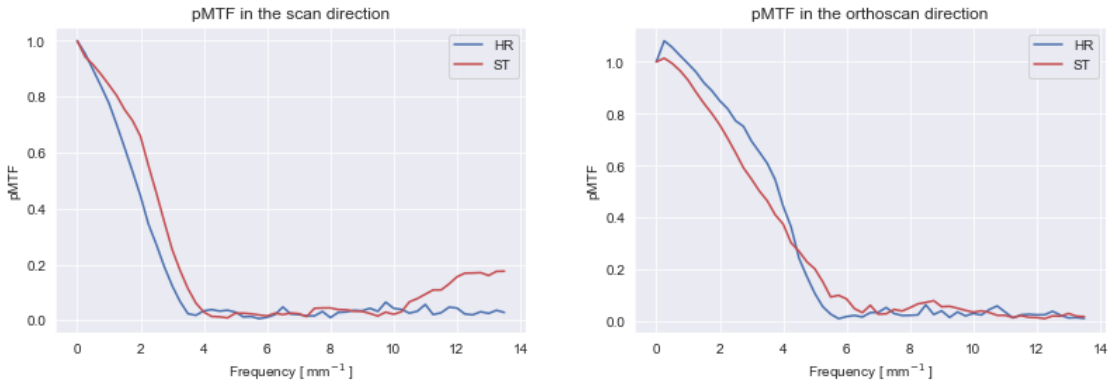

(a) (b)

Figure 4.13: Pre-sampling *MTF* curves measured in first projection images acquired in ST and HR mode, with the edge at approximately 70 mm above the bucky in the (a) tube travel (scan) direction and in the (b) chest wall-nipple (orthoscan) direction.

	MTF_{50} (mm^{-1})		MTF_{10} (mm^{-1})	
System	Scan	Orthoscan	Scan	Orthoscan
Selenia Dimensions	3.03	3.31	5.72	5.97
Innovality ST	2.42	3.42	3.55	5.68
Innovality HR	3.18	4.12	4.69	5.23

Table 4.13: MTF_{50} and MTF_{10} outputted by MAMMO QC, corresponding to the edge positioned at 40 mm above the breast support table.

4.2.3 *MTF* in the reconstructed image

This part of the analysis focuses on the assessment of the *MTF*, also taking into account the effect of the reconstruction algorithm on image sharpness, and therefore providing a total system *pMTF*.

Using MAMMO QC, *pMTF* curves in the chest wall-nipple and scan directions were computed from reconstructed stacks of CIRS 021, arranged according to the two experimental set ups described in Chapter 3. First of all, no significant differences between the measurements obtained from the two set ups was found, with a *COV* between the MTF_{50} values of at most 4%.

The results corresponding to the phantom set up in figure 3.14a are presented in figure 4.14, which shows the *pMTF* curves normalised to the peak value, in the scan and orthoscan directions,for the two DBT systems. The MTF_{50} and MTF_{10} points taken from the curves can be found in table 4.14.

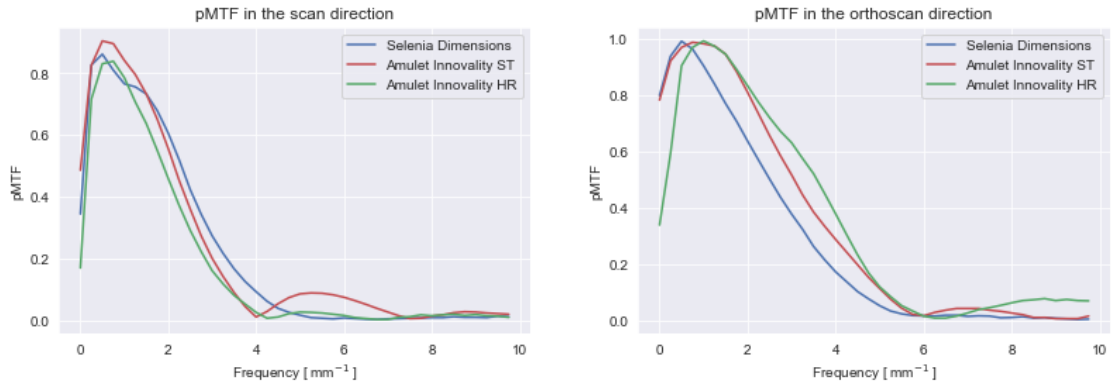

(a) (b)

Figure 4.14: Pre-sampling *MTF* curves measured in reconstructed images of a tungsten wire, for the two DBT systems (a) *pMTF* in the tube travel (scan) direction (b) *pMTF* in the chest wall-nipple (orthoscan) direction.

	MTF_{50} (mm^{-1})		MTF_{10} (mm^{-1})	
System	Scan	Orthoscan	Scan	Orthoscan
Selenia Dimensions	2.30	3.94	2.51	4.54
Amulet Innovality ST	2.13	3.45	3.06	5.10
Amulet Innovality HR	1.89	3.37	3.58	5.15

Table 4.14: MTF_{50} and MTF_{10} outputted by MAMMO QC, and measured from the tungsten wires in CIRS 021, held at roughly 45 mm above the breast support table.

Looking at the curves, a reduction in the *pMTF* at low frequencies (less than 1 mm^{-1}) was noticed for both systems. This is consistent with the literature and is due to the ramp (sharpening) filter applied in the reconstruction algorithm [45], which would result in a decreased contrast of large area objects. The effect of the ramp filter appears to be more prominent in figure 4.14a, indicating that stronger filtering is applied in the scan direction, which is also in agreement with previous studies [46].

Secondly, being both systems characterised by a continuous motion of the x-ray tube, the MTF_{50} measured in the orthoscan direction was found to be 6% to 62% greater than in the scan direction, which is affected by the focal spot motion. The influence of the angular range can also be observed in the lower *pMTF* curve for the HR imaging of the AMULET Innovality, as opposed to the ST mode and the Selenia Dimensions, with a reduction of the MTF_{50} by 12% and 20% respectively. This is also in agreement with the data reported in [46].

In the current version of the EUREF protocol, the assessment of the *MTF* in the *x*-*y*

plane of the reconstructed image is optional, given the ongoing research regarding the evaluation of image quality in DBT. Nevertheless, results such as the ones obtained with CIRS 021 can be used for reference purposes in stability testing, as it is also recommended in the protocol.

4.2.4 Z-resolution with spheroidal masses of varying diameter

Using reconstructed images of the target slab illustrated in figure 3.1b of CIRS 021, the dependence of the *ASF FWHM* on detail size and scan angle was further investigated. Figure 4.15 shows *ASF* profiles along the z-direction, for spheroidal masses of size 3.9 mm, 4.7 mm and 6.3 mm, imaged with the Selenia Dimensions and AMULET Innovality.

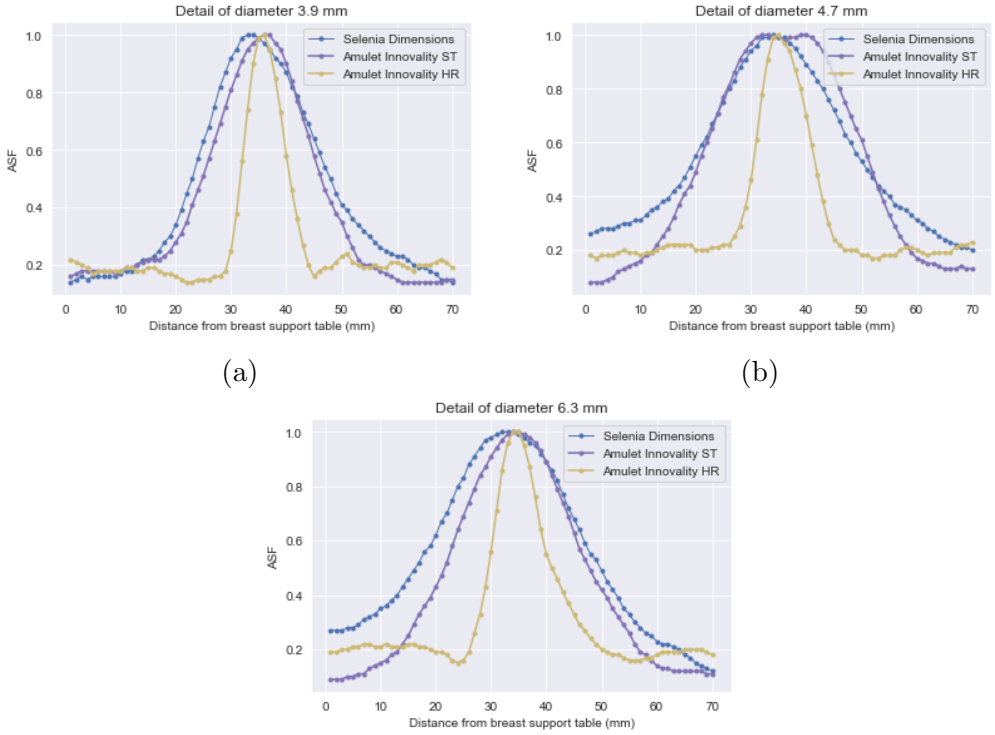

Figure 4.15: ASF profiles produced by spheroidal masses of different size included in CIRS 021, for the two DBT systems.

As expected, the detail of diameter 6.3 mm gives rise to a higher degree of artefact spread, as it is indicated by the wider *ASF* profiles in 4.15c. This is confirmed by the *FWHM* values reported in table 4.15, which are reduced by up to 40% for the Innovality ST. However, it was found that for the bigger sphere diameters, namely 4.7 mm and

	ASF FWHM (mm)		
System	3.9 mm	4.7 mm	6.3 mm
Selenia Dimensions	22.8 ± 0.4	28.0 ± 0.4	31.4 ± 0.5
Innovality ST	18.9 ± 0.2	29.3 ± 0.5	24.7 ± 0.2
Innovality HR	7.3 ± 0.2	9.6 ± 0.1	9.7 ± 0.3

Table 4.15: *ASF FWHM* computed from spheroidal masses of different diameter. Propagation of uncertainty was used to estimate the errors.

6.3 mm, there was no significant difference between the respective *FWHM* values. This is in agreement with the findings in [25], where comparable *ASF* profiles from spheres of diameter ranging from 4.76 mm to 9.52 mm were obtained. Additionally to this, a reduction of the *ASF FWHM* in the HR mode was once again observed, confirming the trend of improved z-resolution with scan angle.

Overall, differences in the shape of the *ASF* between the systems can be noticed, with the ST mode of the AMULET Innovality exhibiting a flat top for the 4.7 mm sphere in figure 4.15b. The reason for this could lie in differing reconstruction techniques.

4.3 Discussion

The results of this study have confirmed that both Mammo 3D Performance Kits and CIRS 021 meet the EUREF protocol requirements for the assessment of the AEC system performance and the z-resolution of the Hologic Selenia Dimensions and Fujifilm AMULET Innovality. Both phantoms made it possible to in effect reproduce the experimental set ups described in the DBT guidelines, and provide adequate high contrast imaging targets, which were necessary to perform the measurements, and obtain the expected results.

Starting with the AEC system performance, the *SDNR* values obtained using the two phantoms were consistent with each other, taking into account their uncertainty ranges. Nevertheless, with the Innovality system, discrepancies occurred for the lower phantom thickness values, and possibly rose from the difference in background material between the two phantoms. This analysis was in fact based on the assumption that PMMA and BR50/50 are of the same density, and therefore equally simulate the equivalent breast thickness values reported in table 3.5. Additionally to this, variations in the position of the aluminium insert could have impacted the results because of the heel effect, therefore reducing the repeatability of measurements. In actuality, CIRS 021 could guarantee better repeatability between exposures since the position of the aluminium plate is fixed within the target slab. On the other hand, Mammo 3D Performance Kits, although providing flexibility, could be more prone to human errors and movements of the Al

plate between exposures.

Moving on to the z-resolution, the results produced by both phantoms were overall consistent with the available literature, in terms of the dependence of the *ASF FWHM* on the object size, and its improvement with the distance from the breast support table. Being the spheres within the phantoms of different diameter and material, inconsistencies between the *ASF FWHM* were found, especially for the Innovality acquisitions in ST mode. However, in comparing the two phantoms, the position of the spheres in the x-y plane must also be taken into account. Specifically to the Innovality, the coordinate system used in the reconstructed volume is such that the *FWHM* of the *ASF* varies with the position of the object with respect to the on-axis point, where the x-ray beam is orthogonal to the detector. For this reason, considering also the different spacing between the spheres in the two phantoms, reproducibility of results is inevitably reduced.

The availability of imaging targets unique to each phantom made it possible to implement additional EUREF QC tests, for the physical characterisation of the two DBT systems. Using projection images of a 2 mm thick aluminium plate included with Mammo 3D Performance Kits, the different detector response functions of the Selenia Dimensions and AMULET Innovality were confirmed to be linear and logarithmic respectively. Furthermore, the outputted coefficients were found to be of the same order of magnitude as the values reported in the available literature [46], [9].

Using the same datasets, noise analysis based on pixel variance was also performed and the expected trends were observed. Namely, the quantum noise component k_{q} was dominant over all other noise sources and slowly decreased with dose, the electronic noise k_{e} decreased to a constant value for exposure levels greater than 6 mGy, and finally structured noise k_{s} increased linearly as a function of *DAK*. In addition to this, it was found that at the standard clinical entrance dose of approximately 4.5 mGy, the percentage fraction of the total noise, for each noise component, was in agreement with the literature [9].

The evaluation of the image receptor of the two systems also included the calculation of the system projection *MTF*, which was determined from the *ESF* generated by the edge test object of Mammo 3D Performance Kits. The results obtained are in agreement with what would be expected considering the acquisition geometry and the design parameters of the two DBT systems. Namely, a superior *MTF* in the direction perpendicular to the tube motion, and a deterioration of sharpness as a function of height above the breast support table, as quantified by the lower *pMTF*.

An exhaustive assessment of the systems' sharpness was completed by making use of reconstructed volumes representing the two 50 µm tungsten wires contained in CIRS 021. As well as confirming the anisotropy of the *MTF*, and the expected trends with the scan angle and distance from the detector, the *pMTF* curves encapsulated the effect of the reconstruction algorithm. As a matter of fact, the filtering of low frequencies resulted in a reduction of the *pMTF* below 1 mm^{-1}.

Finally, CIRS 021 also offered the possibility to further investigate the variation of the

z-resolution as quantified by the *ASF*, as a function of object size. Using the spheroidal masses in CIRS 021 which simulate breast carcinoma, it was found that the difference in mass size is less impacting on the *ASF FWHM*, for the spheres of diameter 4.7 mm and 6.3 mm, and for the wide angle HR acquisitions of the Innovality.

All things considered, Mammo 3D Performance Kits and CIRS 021 allow to effectively simulate the radiation matter interactions taking place in x-ray imaging of the breast. By providing appropriate imaging targets and background material, it was possible to reproduce the experimental conditions required to observe the expected patterns, and confirm these trends through the computation of quantitative image quality parameters, as suggested by the EUREF DBT QC protocol.

4.3.1 Future developments

This study has served as a starting point for the development of a software for the automation of QC procedures in Digital Breast Tomosynthesis, by Tecnologie Avanzate.

With work on its first version underway, the software would come in the form of a Python application, and allow the user to perform QC tests, according to the EUREF protocol. The application would integrate the ImageJ macros and Python scripts, which were used in this thesis, into new functionalities providing full automation of the QC procedures and output of results. To this end, the evaluation of the Hologic Selenia Dimensions and Fujifilm AMULET Innovality systems, using the two different phantoms, made it possible to identify variability factors which are system and phantom dependent, leading to specific software requirements.

These include the extraction of information from DICOM tags as opposed to the need for user inputs, and the automatic detection of areas of extra attenuation. Moreover, as it has been shown in this thesis, the implementation of the tests by the software would, to some extent, depend on the phantom. The reason for this is that, the type of imaging targets entails specific approaches in the calculation of image quality parameters, e.g. wire or edge method for the *MTF*. Additionally, the arrangement of the test objects within the phantom also affects the positioning of the ROIs. Taking target slab 1 of CIRS 021 as an example, a fully automated software would need to detect only those high contrast details required for the test being performed, leaving the rest out in the creation of the signal and background ROIs.

At the present time, completion of automated AEC system performance and z-resolution tests has been reached. In addition to the implementation of additional tests, the software design could be enhanced by integrating checks on the image parameters and DICOM tags, e.g. kVp, exposure, and pixel values, in order to detect potential human errors in the acquisition of the datasets, and warn the user. This functionality could be tested on image datasets acquired by purposely altering the EUREF protocol, e.g. using the wrong inserts, and taking as a reference the experimental results of this study.

Conclusions

The aim of this project was to verify the suitability of Sun Nuclear's Mammo 3D Performance Kits and CIRS DBT QC Phantom, model 021, in testing two DBT systems under the current version of EUREF DBT QC protocol. This implied the use of the image processing software ImageJ and Python programming language for the implementation of the image quality measurements prescribed by the protocol.

In the first part of the analysis, it was found that both phantoms provide imaging targets suitable for the assessment of the AEC system performance and z-resolution, and enabled measurements at different heights above the breast support table. Moreover, the results obtained from the computation of the relevant quantitative metrics, were consistent with the the differences in material and size of the test objects.

For the second part, further QC measurements for the physical characterisation of the two DBT systems were considered. These included the response function and noise analysis, the *MTF* from the signal produced by an edge and a wire, and finally the *ASF* of spheres of varying diameters. By comparing the results obtained with the available literature, the use of the phantoms on the two DBT systems considered was thus validated.

Throughout the implementation of the QC tests, differences between the two phantoms in terms of practicality were also highlighted. For instance, movements of CIRS 021 between exposures were limited by the magnetic holder, keeping all the slabs together. This was not the case with Mammo 3D Performance Kits, which required readjustments of the PMMA layers between acquisitions. Moreover, being the test objects integral with the target slab, measurements with CIRS 021 would be less prone to human errors, enabling greater reproducibility of results, as well as faster acquisitions. Lastly, the two phantoms are considerably different in size, shape and weight, with Mammo 3D Performance Kits being more bulky than CIRS 021. Nonetheless, Mammo 3D Performance Kits includes a greater variety of tools, guaranteeing a more comprehensive system evaluation under the EUREF DBT QC protocol.

That being said, in developing a fully automated software, it would be advisable to set requirements tailored to both phantoms.

Acknowledgements

I would like to express my immense gratitude to my supervisor Professor Nico Lanconelli, for his invaluable guidance and feedback throughout this project, and whose teaching was a great influence in choosing the topic of my thesis. Furthermore, I would like to give my deepest appreciation to my co-supervisors Dr Matilde Costa, Dr Barbara Mongero and Dr Silvia Pesente, for their outstanding expertise and mentorship.

In addition, I would like to sincerely thank Dr. Gabriele Massari for his expert knowledge and precious help whenever I had a question. I am also grateful to Dr. Antonella Talamo, and the rest of the team at Tecnologie Avanzate, for all the resources and support they provided during my internship.

Finally, I would like to thank the Mammography Department at Ospedale Molinette, in Turin, and Dr Daniela Origgi and her colleagues at the European Institute of Oncology in Milan, for providing access to the equipment, and supporting the data acquisition process.

I would like to finally thank my parents for their constant encouragement during my studies, and my brother Christopher who has been my role model throughout all the stages of my education, from helping me with my school homework to being a reference point during my studies at university.

Bibliography

[1] F.C. Geyer B. Weigelt and J.S. Reis-Filho. Histological types of breast cancer: How special are they? *Mol Oncol.*, 4(3), June 2010.

[2] European Commission. European commission initiative on breast cancer (ECIBC): European guidelines on breast cancer screening and diagnosis. Available at `https://healthcare-quality.jrc.ec.europa.eu/european-breast-cancer-guidelines/screening-tests/DBT-or-DM` (Accessed: 5 January 2023).

[3] European Commission. Screening ages and frequencies. Available at `https://healthcare-quality.jrc.ec.europa.eu/ecibc/european-breast-cancer-guidelines/screening-ages-and-frequencies` (Accessed: 5 January 2023).

[4] Sun Nuclear. A Mirion Medical Company. Digital breast tomosynthesis qc phantom. Available at `https://www.cirsinc.com/products/mammography/digital-breast-tomosynthesis-qc-phantom/` (Accessed: 28 June 2022).

[5] Sun Nuclear. A Mirion Medical Company. Mammography compliance phantoms. Available at `https://www.sunnuclear.com/products/mammography-compliance-phantoms` (Accessed: 28 June 2022).

[6] K. C. Young D. R. Dance and R. E. van Engen. Estimation of mean glandular dose for breast tomosynthesis: factors for use with the UK, European and IAEA breast dosimetry protocols. *Phys. Med. Biol.*, 56(2011), December 2010.

[7] D. R. Dance. Monte carlo calculation of conversion factors for the estimation of mean glandular breast dose. *Phys. Med. Biol.*, 35(9), May 1990.

[8] M.J. Flynn E. Samei and D.A. Reimann. A method for measuring the presampled MTF of digital radiographic systems using an edge test device. *Phys. Med. Biol.*, 25(1), Jan 1998.

[9] A. Rodriguez-Ruiz et al. Evaluation of the technical performance of three different commercial digital breast tomosynthesis systems in the clinical environment. *Phys. Med. Biol.*, 32(6), Jun 2016.

[10] C.J. Strudley et al. NHS Breast Screening Programme equipment report. Technical evaluation of Fujifilm AMULET Innovality digital breast tomosynthesis system. Available at `https://medphys.royalsurrey.nhs.uk/nccpm/?s=tomosynthesisqctools` (Accessed: 3 March 2023).

[11] C.J. Strudley et al. NHS Cancer Screening Programmes. Technical evaluation of Hologic Selenia Dimensions digital breast tomosynthesis system. Available at `https://medphys.royalsurrey.nhs.uk/nccpm/?s=tomosynthesisqctools` (Accessed: 16 November 2022).

[12] D. R. Dance et al. Additional factors for the estimation of mean glandular breast dose using the UK mammography dosimetry protocol. *Phys. Med. Biol.*, 45(2000), June 2000.

[13] E. Samei et al. Assessment of multi-directional MTF for breast tomosynthesis. *Phys. Med. Biol.*, 58(5), Mar 2013.

[14] G. Dietze et al. Basis for Dosimetric Quantities used in Radiological Protection. Available at `https://www.icrp.org/docs/Physics_ICRP_Found_Doc_for_web_consult.pdf` (Accessed: 17 February 2023).

[15] H. Fujita et al. A Simple Method for Determining the Modulation Transfer Function in Digital Radiography. *IEEE Transactions on Medical Imaging*, 11(1), Mar 1992.

[16] H. H. Barrett et al. Task-based measures of image quality and their relation to radiation dose and patient risk. *Phys. Med. Biol.*, 60(2):R1, Jan 2015.

[17] J.T. Bushberg et al. *The Essential Physics of Medical Imaging*. Lippincott Williams & Wilkins, Philadelphia, PA USA, 2012.

[18] L. Karsa et al. European guidelines for quality assurance in breast cancer screening and diagnosis: fourth edition, supplements. Available at `https://euref.org/european-guidelines/physico-technical-protocol/` (Accessed: 28 June 2022).

[19] LMFH Neeter et al. Contrast-enhanced mammography: what the radiologist needs to know. *BJR Open*, 3(1), November 2021.

[20] M. Arnold et al. Current and future burden of breast cancer: Global statistics for 2020 and 2040. *The Breast*, 66, September 2022.

[21] M. O. Jousi et al. A new breast tomosynthesis imaging method: Continuous Sync-and-Shoot – technical feasibility and initial experience. *Acta Radiol Open*, 8(3), March 2019.

[22] M.A. Orsi et al. Digital breast tomosynthesis: A state-of-the-art review. *Nuclear Medicine and Biomedical Imaging*, 3(4), December 2018.

[23] N. Perry et al. European guidelines for quality assurance in breast cancer screening and diagnosis. 4th edition. Available at `https://euref.org/european-guidelines/physico-technical-protocol/` (Accessed: 28 June 2022).

[24] O. Ginsburg et al. Breast cancer early detection: A phased approach to implementation. *Cancer*, 126(Suppl 10), May 2020.

[25] P. Colombo et al. Artifact analysis in digital breast tomosynthesis (dbt). Available at `https://www.researchgate.net/publication/266094050` (Accessed: 8 Jan 2023).

[26] P. Monnin et al. Comparison of the polynomial model against explicit measurements of noise components for different mammography systems. *Phys. Med. Biol.*, 59(19), Septembet 2014.

[27] P.Skaane et al. Digital Mammography versus Digital Mammography Plus Tomosynthesis in Breast Cancer Screening: The Oslo Tomosynthesis Screening Trial. *Riadology*, 291(1), April 2019.

[28] R. Bouwman et al. An alternative method for noise analysis using pixel variance as part of quality control procedures on digital mammography systems. *Phys. Med. Biol.*, 54(22), Oct 2009.

[29] S. Ciatto et al. Integration of 3D digital mammography with tomosynthesis for population breast-cancer screening (STORM): a prospective comparison study. *The Lancet Oncology*, 14(7), June 2013.

[30] S. Vedantham et al. Digital Breast Tomosynthesis: State of the Art. *Radiology*, 277(3), December 2015.

[31] EUREF. EUREF typetest protocol. Available at `https://euref.org/euref-typetest-protocol/` (Accessed: March 31 2023).

[32] Fujifilm. Value from Innovation. AMULET Innovality. Fujifilm Digital Mammography System. Available at `https://asset.fujifilm.com/www/uk/files/2021-05/617e8ced3d01d37e840ad94f5b0a99a7/AMULET_Innovality_Brochure_2020.pdf` (Accessed: March 22 2023).

[33] Fujifilm. Value from Innovation. Technical Specifications. Available at https://womenshealth-emea.fujifilm.com/discover-amulet-world/amulet-innovality-world/technical-specifications/#Tomosynthesis (Accessed: March 22 2023).

[34] EFOMP Mammo Working Group. EFOMP Mammo Protocol. Available at https://www.efomp.org/index.php?r=fc&id=protocols (Accessed: Dec 20 2023).

[35] ICRP. History. Available at https://www.icrp.org/page.asp?id=9 (Accessed: 17 February 2023).

[36] J. T. Dobbins III and D. J. Godfrey. Digital x-ray tomosynthesis: current state of the art and clinical potential. *Phys. Med. Biol.*, 48(2003), September 2003.

[37] R.A. Jesinger. Breast anatomy for the Interventionalist. *Tech Vasc Interv Radiol.*, 17(1), March 2014.

[38] N. Lanconelli. Tomographic reconstruction. *Physics of Medical Imaging*, Alma Mater Studiorum University of Bologna, delivered 18 May 2021.

[39] N. Lanconelli. X-ray planar imaging, lecture notes. *Physics of Medical Imaging*, Alma Mater Studiorum University of Bologna, delivered 2 March 2021.

[40] N. Lanconelli. Digital image processing. *Image Processing*, Alma Mater Studiorum University of Bologna, delivered 7 October 2020.

[41] A. Mackenzie. Validation of correction methods for the non-linear response of digital radiography systems. *The British Journal of Radiology*, 81(964), May 2008.

[42] A. Maldera. Digital breast tomosynthesis: Dose and image quality assessment. *Phys. Med.*, 33, Jan 2017.

[43] EFOMP Mammo Working Group. Quality Control in Digital Breast Tomosynthesis. EFOMP Protocol. Version 01.03.2023. Available at https://www.efomp.org/index.php?r=fc&id=protocols (Accessed: 3 March 2023).

[44] A.L. Manninen. Clinical applications of radiophotoluminiscence (RPL) dosimetry in evaluation of patien radiation exposure in radiology. Determination of absorbed and effective dose. Available at https://www.researchgate.net/figure/Schematic-representation-of-the-photoelectric-effect-and-forming-of-an-Auger-electron_fig1_298709741 (Accessed: 1 February 2023).

[45] N. W. Marshall and H. Bosmans. Measurements of system sharpness for two digital breast tomosynthesis systems. *Phys. Med. Biol.*, 57(22), Nov 2012.

[46] N. W. Marshall and H. Bosmans. Performance evaluation of digital breast tomosynthesis systems: physical methods and experimental data. *Phys. Med. Biol.*, 67(22), Nov 2022.

[47] M. P. Morigi. Scintillation detectors, lecture notes. *Health Physics*, Alma Mater Studiorum University of Bologna, delivered 10 November 2020.

[48] M. P. Morigi. Biological Effects of Ionizing Radiation. effects on humans, lecture notes. *Health Physics*, Alma Mater Studiorum University of Bologna, delivered 27 October 2020.

[49] NHS. Breast cancer in women. Available at `https://www.nhs.uk/conditions/breast-cancer/` (Accessed: 5 January 2023).

[50] NIST. X-ray Mass Attenuation Coefficients. Available at `https://www.nist.gov/pml/x-ray-mass-attenuation-coefficients` (Accessed: March 31 2023).

[51] World Health Organization. Breast cancer. Available at `https://www.who.int/news-room/fact-sheets/detail/breast-cancer` (Accessed: 5 January 2023).

[52] M. Porzio and A. Konstantinidis. Plugins for QC compliant with the European guidelines and EUREF/EFOMP protocols for digital mammography and digital breast tomosynthesis. Available at `https://data.mendeley.com/datasets/8jj7865wfn/9` (Accessed: 17 Aug 2022).

[53] I. Sechopoulos. A review of breast tomosynthesis. Part i. The image acquisition process. *Med. Phys.*, 40(1), January 2013.

[54] I. Sechopoulos. A review of breast tomosynthesis. Part ii. Image reconstruction, processing and analysis, and advanced applications. *Med. Phys.*, 40(1), January 2013.

[55] J.A. Seibert and J.M. Boone. X-ray Imaging Physics for Nuclear Medicine Technologists. Part 2: X-Ray Interactions and Image Formation. *Journal of Nuclear Medicine Technology*, 33(1), April 2005.

[56] A. Smith. Fundamentals of Breast Tomosynthesis. Improving the Performance of Mammography. Available at `http://hologic.ca/sites/default/files/Fundamentals%20of%20Breast%20Tomosynthesis_WP-00007.pdf` (Accessed: 28 June 2022).

[57] A. Smith. Design Considerations in Optimizing a Breast Tomosynthesis System. 2017.

[58] American Cancer Society. Types of Breast Cancer. Available at https://www.cancer.org/cancer/breast-cancer/about/types-of-breast-cancer.html (Accessed: 14 February 2023).

[59] R. van Engen et al. Protocol for the Quality Control of the Physical and Technical Aspects of Digital Breast Tomosynthesis Systems. Available at https://euref.org/download/euref-tomosynthesis-protocol-version-1-03/ (Accessed: 28 June 2022).

[60] M. J. Yaffe. Mammographic density. Measurement of mammographic density. *Breast Cancer Research*, 10(209), January 2008.